University of Cincinnati

Date: 3/24/2015

I, Abhay Srinivas . , hereby submit this original work as part of the requirements for the degree of Master of Science in Aerospace Engineering.

It is entitled:

Novel Compressor Blade Design Study

Student's name: **Abhay Srinivas .**

This work and its defense approved by:

Committee chair: Mark Turner, Sc.D.

Committee member: Shaaban Abdallah, Ph.D.

Committee member: Paul Orkwis, Ph.D.

18423

Novel Compressor Blade Design Study

Abhay Srinivas

B.E., NITTE Meenakshi Institute of Technology, India, 2013

A thesis submitted to the

Faculty of the Graduate School of the

University of Cincinnati in partial fulfillment

of the requirements of the degree

Master of Science

Departement of Aerospace Engineering and Engineering Mechanics

College of Engineering and Applied Sciences

Committee Chair: Mark G. Turner, ScD

March 24 2015

Abstract

Jet engine efficiency goals are driving compressors to higher pressure ratios and engines to higher bypass ratios, each one driving to smaller cores. This is leading to larger tip gaps relative to the blade height. These larger relative tip clearances would negate some of the cycle improvements, and ways to mitigate this effect must be found. A novel split tip blade geometry has been created which helps improve the efficiency at large clearances while also improving operating range. Two identical blades are leaned in opposite directions starting at 85% span. They are cut at mid chord and the 2 halves then merged together so a split tip is created. The result is similar to the alula feathers on a soaring bird. The concept is that the split tip will energize the tip flow and increase range. For higher relative tip clearance, this will also improve efficiency. The 6th rotor of a highly loaded 10 stage machine was chosen as the baseline for this study. Three dimensional CFD simulations were performed using CD Adapco\'s Star-CCM+ at 5 clearances for the baseline and split tip geometry. The choking flow and stall margin of the split tip blade was higher than that of the baseline blade for all tip clearances. The pressure ratio of the novel blade was higher than that of the baseline blade near choke, but closer to stall it decreased. The sensitivity of peak efficiency to clearance was improved. At tight clearances of 0.62% of blade height, the maximum efficiency of the new design was less than the baseline blade, but as the tip clearance was increased above 2.5%, the maximum efficiency increased. Structural analysis was also performed to ascertain the feasibility of the design.

Acknowledgments

The author would like to thank the College of Engineering and Applied Sciences at University of Cincinnati for supporting this research.

Thanks are given to Dr. Paul Orkwis and Dr. Shabaan Abdallah for their guidance and agreeing to be part of the defense committee.

The author also wants to thank Rob Ogden for his knowledge and support setting up and maintaining the computers and cluster in the lab. Most accomplishments in the lab would not be possible if it were not for Rob.

Special thanks also goes to Kiran Siddappaji , Ahmed Nemnem and Robert Knapke, and for helping with a various number of issues and problems that were encountered during this project.

Last and far from least the author wants to thank Dr. Mark Turner, knowledge and curiosity, and for their support to finish this thesis.

Contents

List of Figures

List of Tables

Nomenclature

Greek Symbols

π Pressure Ratio

ψ Function

ρ Density

θ Tangential Direction

Abbreviations

$\dot{m}$ Mass Flow Rate

PR Pressure Ratio

PT Total Pressure

R Gas Constant

TR Temperature Ratio

TT Total Temperature

Subscripts

i Values at inlet

o Values at outlet

r Radial Direction

T Stagnation Values

t Tangential Direction

z Axial Direction

Chapter 1

Introduction

Advancements in gas turbine technology are pushing engine designs toward weight reduction, higher thrust, improved stall margin, and reduced fuel consumption. To improve propulsive efficiency, higher bypass ratios must be obtained. This is accomplished by a reduction in core engine size, rather than increased fan diameter, to fit current aircraft. These design requirements necessitate improved aerodynamics of axial compressors. The compressor, the heaviest component of the engine, defines the stability margin for the engine and can provide significant improvements to specific fuel consumption (SFC) and overall efficiency. Since the compressor absorbs a majority of the power generated from the turbine, any improvement to the compressor greatly impacts the overall engine efficiency.

The tip clearance is one of the most important source of losses in axial compressors. Tip leakage flows are a major source of unsteadiness and three-dimensionality of the flow in turbomachines, while contributing significantly to loss of efficiency and useful work in turbomachines. They have therefore been the subject of many studies. As much as 30 percent of the total loss in compressors is sometimes attributed to the flow through the tip clearance. It is well known that tip clearance flows can reduce the pressure rise, flow range, and efficiency of turbomachinery. One of the most significant effects of the tip leakage flow is the loss in peak total pressure rise, which can be attributed to entropy generation from the tip leakage jet being injected into the main flow. Figure 1.1 shows the tip clearance of a rotor blade. The tip leakage flow is generated by the pressure difference between the pressure side and suction side of the rotor tip. This pressure differential introduces a high velocity flow through the tip clearance gap which is ejected into the passage. In addition to this effect, the relative motion of the end wall with respect to the tip leakage flow is in the same direction of the leakage flows and serves to enhance them, refer Figure 1.2. The tip gap vortex is formed as the pressure-driven leakage flow interacts with the main passage flow, refer Figure 1.2a, which can interact with the end wall boundary layer drawing the low momentum fluid further into the main passage flow,Figure 1.2b.

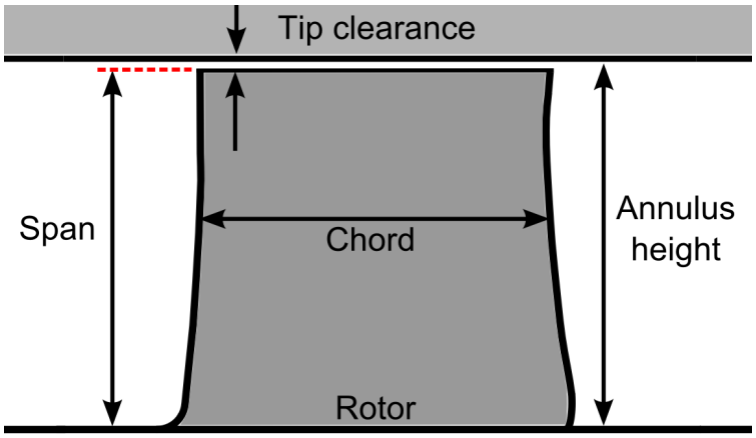

Figure 1.1: Tip Clearance of a blade. [1]

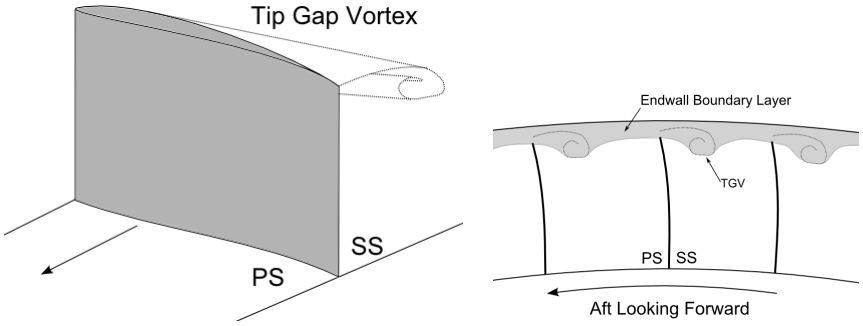

(a) Tip Vortex Formation[1]

(b) End wall boundary layer interaction[1]

Figure 1.2: Simplified Flow field

The rear stages of axial compressors decrease in annulus height and blade aspect ratio to achieve constant axial velocity with the increased density, but the clearance between the rotors and casing remains nearly constant resulting in high relative clearance ratios (clearance/span and clearance/chord). This results in a significant increase in the relative tip clearance ratio and a flow field dominated by end wall flows. New turbofan engines with increased bypass ratios accomplished with reduced core size lead to physically smaller flow paths where the relative size of the tip gap is large leading to large tip leakage flows.

A general design rule is a 1% decrease in compressor efficiency occurs with a 1% increase in tip clearance. A 1% change in efficiency of the high pressure compressor yields up to a 0.66% SFC change on a given engine [4]. Large tip leakage flows not only decrease operability but also efficiency.

Increased tip clearance also leads to early stall inception, resulting in decreased operating range and compressor stability. A large amount of studies were performed concerning the effect of this tip gap on the characteristics of axial compressors and turbines. Smith and Cumpsty[5] have shown a 23 percent drop in maximum pressure rise and a 15 percent increase in flow coefficient at stall in a large, low speed compressor as the tip clearance

was increased from 1 to 6 percent of chord. Wisler[4] has shown a 1.5 point drop in efficiency of a low speed compressor when the tip clearance was doubled. Yet the details of tip clearance flows are not well understood. Storer and Cumpsty[3], for example, suggest that most of the loss often attributed to tip clearance effects are probably due to other causes.

To overcome the effects of large tip gaps a novel split tip blade has been designed which can improve the overall efficiency and stall margin of the blade. Two identical blades are leaned in opposite directions starting at 85% span. They are cut at mid chord and the 2 halves then merged together so a split tip is created. The result is similar to the alula feathers on a soaring bird, Figure 1.3. 3D CFD analysis has been done using CD-Adapco's Star-CCM+ [14]. The 6th rotor of a highly loaded 10 stage machine was chosen as the baseline for this study. Structural analysis was also performed to ascertain the feasibility of the design using ANSYS [15].

Figure 1.3: Alula feathers on a soaring bird.[2]

Chapter 2

Literature Review

The complications related to the operation of compressors with increased tip clearance have been known since the inception of the gas turbine. An extensive base of research has been built from isolated rotors, single-stage, and multistage machines. However, a unified understanding of the flow physics is still lacking.

Storer and Cumpsty [3] studied the effect of tip leakage flow in a linear cascade using both experimental methods and three dimensional numerical solutions. The linear cascade consisted of 5 blades. Figure shows the contours of endwall static pressure distributions. It was observed that with a tip clearance typical of that in a machine the clearance flow separates from the blade tip and does not reattach along the majority of the chord. Also the magnitude and chordwise distribution of the tip leakage flow depends on the static pressure field near the end wall of the blade. Although the suction surface pressure changes with tip clearance, the pressure distribution outside the endwall boundary layer remains the same. Also it was observed that the tip clearance vortex increases in size and strength as the clearance is increased.

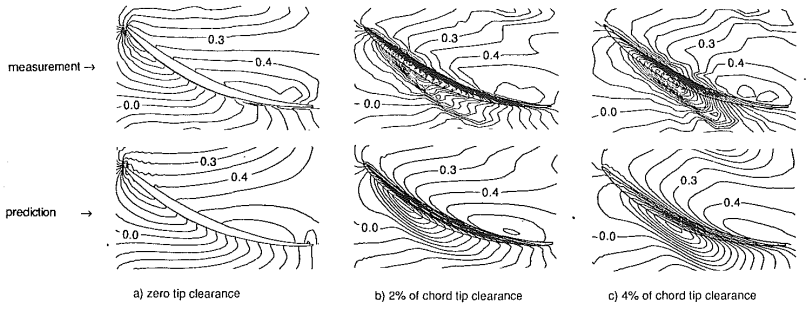

Figure 2.1: Measured and predicted endwall static pressure distributions. [3]

Wisler [4] studied the effects of tip clearance on performance of a compressor. He used a low speed model of a high speed compressor to evaluate the performance. The performance of the low speed baseline compressor was evaluated to locate the regions of high loss and potential improvement. Overall performance was obtained at two levels of tip clearance to height ratio, 1.36 and 2.8 percent. The results are shown in Figure 2.2. This increase in tip clearance costs 1.5 points in peak efficiency, 11.0 percent in stalling

flow coefficient (flow range), and 9.7 percent in peak pressure rise relative to the nominal clearance. The increase in loss near the casing at increased clearance extended to 30 percent immersion in the measured profiles of relative total pressure.

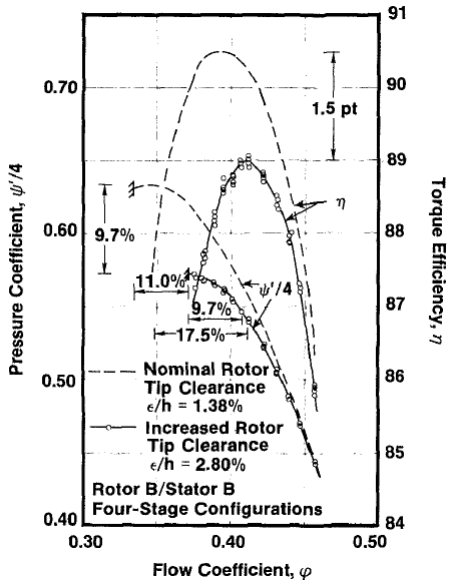

Figure 2.2: Flow Characteristics.[4]

Smith and Cumpsty [5] experimentally studied the flow through a axially skewed casing treatment. The slots were inclined such that the flow emerging from them would posses swirl in the opposite sense to that of the rotor motion. A low speed compressor of 1.52-m tip diameter and 0.4 hub/tip ratio was used for the experiment. The rotor was fitted with 22 blades with a constant chord length of 152.4 mm, giving hub and tip solidities of 1.43 and 0.47 respectively. Flow characteristics were measured at different locations, upstream of the slot, in between the slot and downstream of the slot to understand to flow the the slot. It was shown from the results that there was about 23 percent drop in maximum pressure rise and a 15 percent increase in flow coefficient at stall as the tip clearance was increased from 1 to 6 percent of chord.

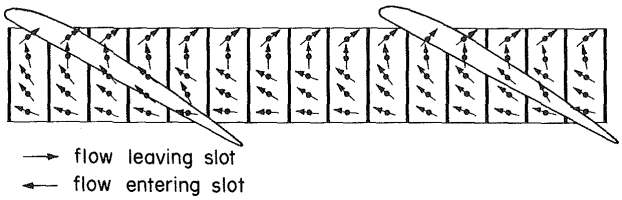

Figure 2.3: Flow direction at mid depth in the treatment slots. [5]

Several other types of casing treatments have also been studied and their effects on performance. Shabbir and Adamczyk [16] conducted studies to understand the physical mechanism responsible for improvement in stall margin of an axial flow rotor due to

circumferential casing grooves. A budget of a axial momentum equation was carried out at the rotor casing in the tip gap in order to understand the physical process behind this stall margin improvement. Numerical analysis was performed on a low speed axial compressor. From the results it was seen that adding circumferential grooves reduced the stall flow coefficient from 0.34 to 0.3.

Wennerstrom [6] performed experimental studies at three different tip clearances on a transonic axial compressor. He later evaluated the performance of the compressor at the three different clearances and an optimum clearance was found. The clearance between the rotor tip and the casing at design speed was predicted to be 0.016 in. (0.41 mm). This is equivalent to 0.415 percent of tip chord, or 0.324 percent of mean span. This was made deliberately tight initially in order to evaluate the sensitivity of the design to tip clearance. Clearance was progressively increased in two steps by grinding 0.010 in. (0.25 mm) from the tips of the rotor blades each time. The casing remained untouched. The resulting test matrix was:

	% Chord	% Span
Original clearance (config 1)	0.415	0.324
First Modification (config 2)	0.675	0.524
Second Modification (config 3)	0.935	0.724

Table 2.1: Wennerstrom test details

Wennerstrom found that the efficiency of a high speed transonic compressor with a tip rotor tip gap of 0.524% span is higher than that with a tip gap of 0.324% span and 0.724% span. Thus there exists a optimum tip clearance and for his case it existed between 0.324% and 0.724%

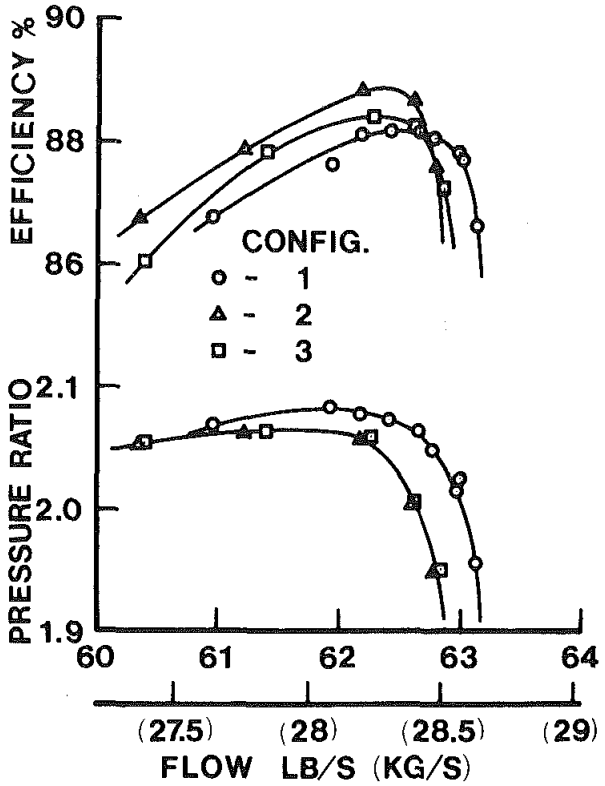

Figure 2.4: Effect of rotor tip clearance changes at design speed. [6]

Dario Bruna conducted computational studies on Rotor 37 with a isothermal and adiabatic boundary conditions [7]. Detailed analysis based on conservation of Rothalpy has been made and applied to the rotor. The case was run at design and double tip clearance. The Pressure ratio and Efficiency speedline are figure 2.5 and 2.6.

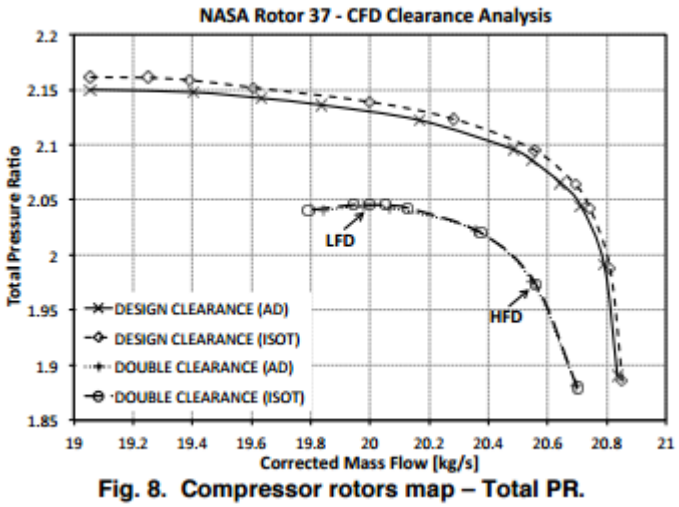

Figure 2.5: Total Pressure Ratio Speedline. [7]

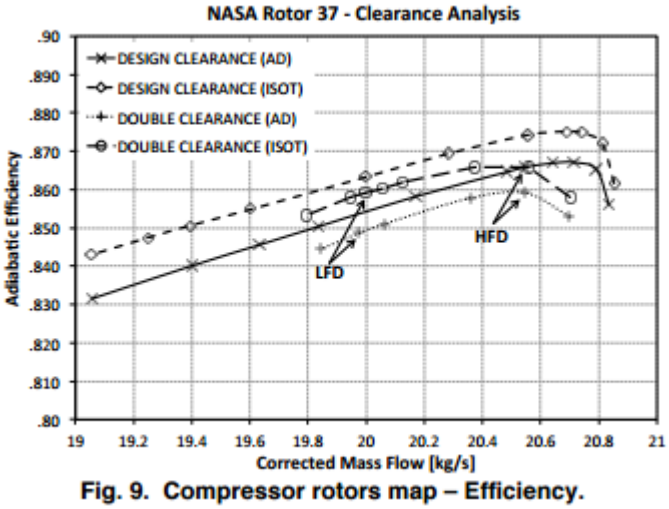

Figure 2.6: Efficiency Speedline. [7]

It was seen that with the increased tip gap the rotor working range (based on the steady CFD calculations) is about half that of the design clearance case. The maximum total PR ratio achieved by the double tip clearance rotor is 5% reduced, and also the efficiency, at any point of the rotor characteristic, is decreased when compared to the design clearance case. The application of the isothermal boundary condition at casing (with double tip clearance gap) had a similar impact on rotor performance, as that at the design clearance.

Anthony Gannon performed experimental studies of the effect of increasing the tip-gap size on the performance of a splittered transonic rotor [8]. The tip gap was varied by changing the diameter of the outer casing while keeping the diameter of the rotor constant. Studies were conducted at 3 different clearances of 0.99 mm, 0.76 mm and 0.53mm and 6 different speeds. The stagination pressure and efficiency performance map is shown in figures 2.7 and 2.8. The variation of Efficiency with tip clearance was also studied and is shown in figure 2.9. It can be seen that as the tip clearance increased the efficiency decreased.

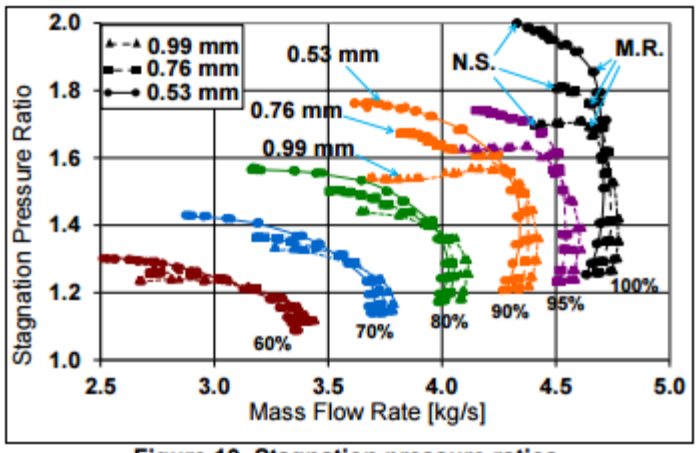

Figure 10. Stagnation pressure ratios.

Figure 2.7: Stagnation pressure Speedline. [8]

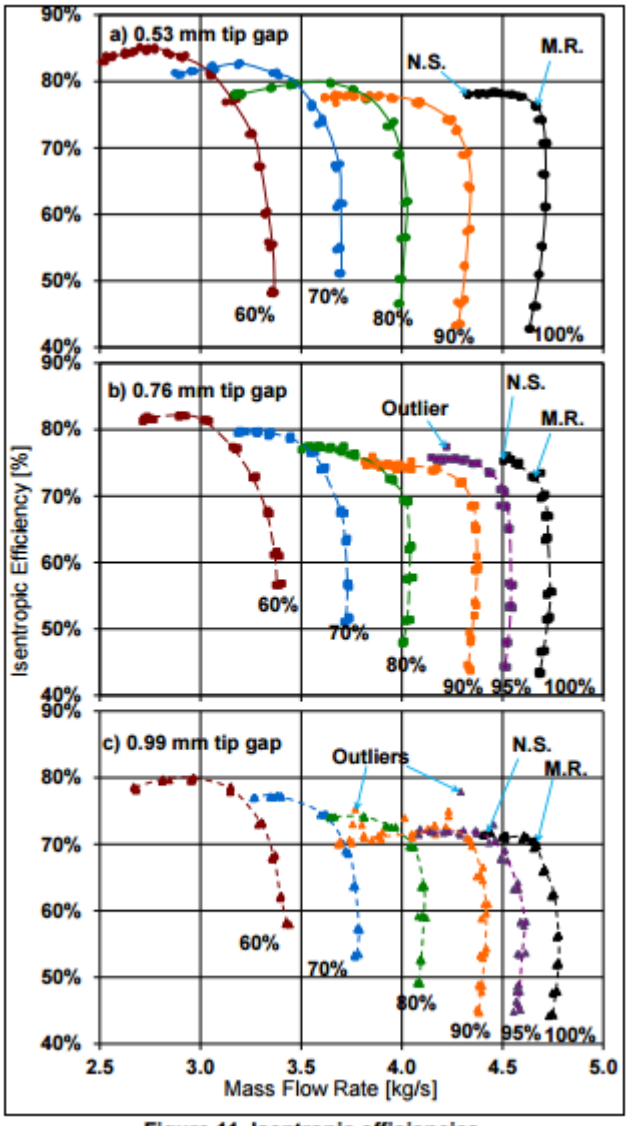

Figure 11. Isentropic efficiencies.

Figure 2.8: Efficiency Speedline. [8]

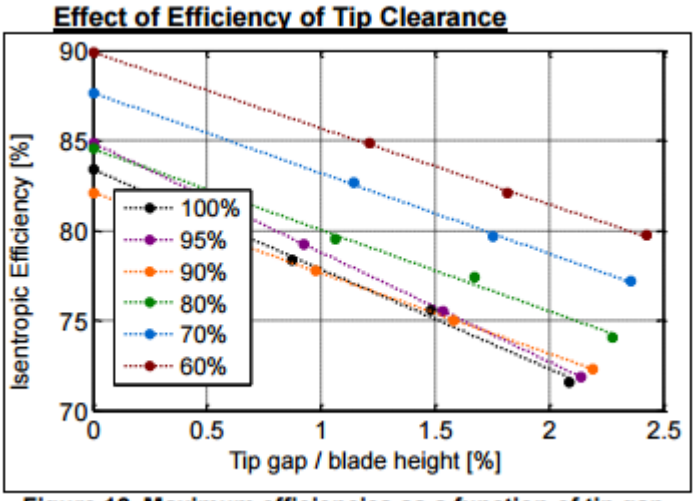

Figure 2.9: Efficiency vs Tip Clearance. [8]

Chapter 3

Methodology

Geometry generation is the most important part in the blade design process. The blade geometry was constructed using 3DBGB[9, 10, 11, 12]. 3DBGB is a blade geometry generation tool that uses a parametric approach to design blades for turbomachinery applications. Due to its parametric nature, a wide range of blades can be designed with relative ease. 2D airfoil sections are created using geometric and aerodynamic input quantities. The sections are stacked in a 3D cylindrical space and are transformed to Cartesian space. This can be imported into any CAD package to create 3D solid models. The geometry builder is also capable of creating complex geometries such as bent tips and split tips with minimum change to the inputs.

3.1 Process Overview

The entire process involves 4 steps

1. Generation of 3D section files in 3DBGB [9, 10, 11, 12].
2. Solid Geometry generation in Star-CCM+.
3. CFD analysis in Star-CCM+.
4. Structural analysis in ANSYS.

Figure 3.1 describes the overall process overview

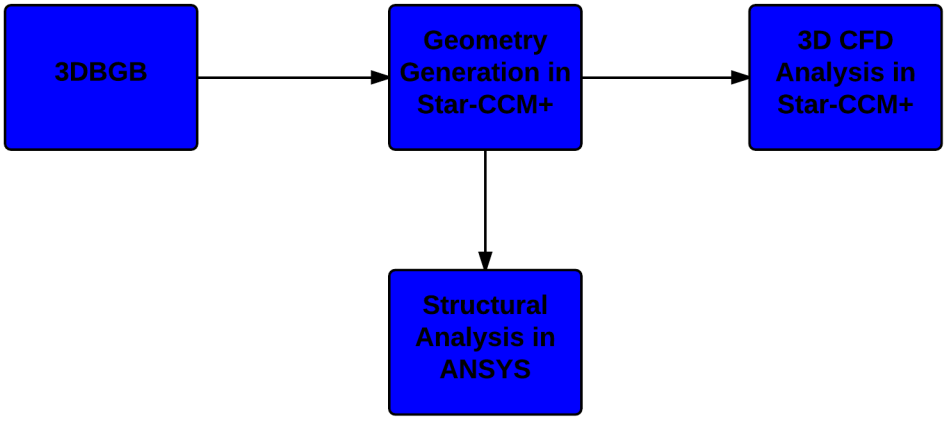

Figure 3.1: Process Overview.

3.2 Blade Design Process

3DBGB[9, 10, 11, 12] uses the input file '3dbgbinput.dat' to extract the input parameters and create 3D sections. The number of blades, scaling factor and number of streamlines are specified in the first few lines of the input file. A switch to use non-dimensional actual chord values is available to enable reverse engineering of known blades. At each streamline (actually a construction curve shown in figure 3.3) the blade inlet and outlet angles, relative mach number at inlet, non-dimensional actual chord, thickness to chord ratio, incidence, deviation and secondary flow angle are specified. The blade stagger angle can be input through the inlet and outlet leading edge and trailing edge angles.

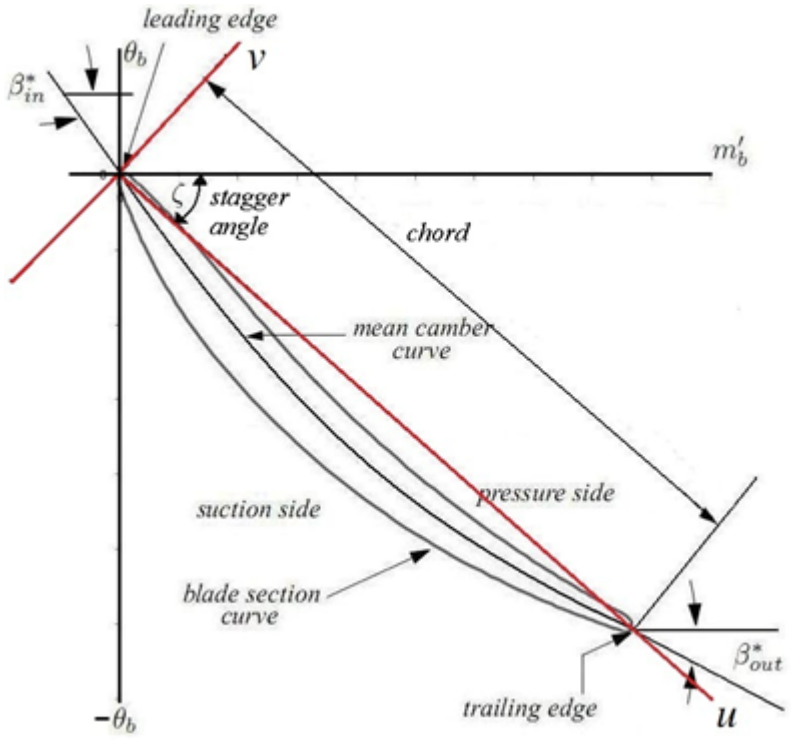

Figure 3.2: Blade Nomenclature.[9, 10, 11, 12]

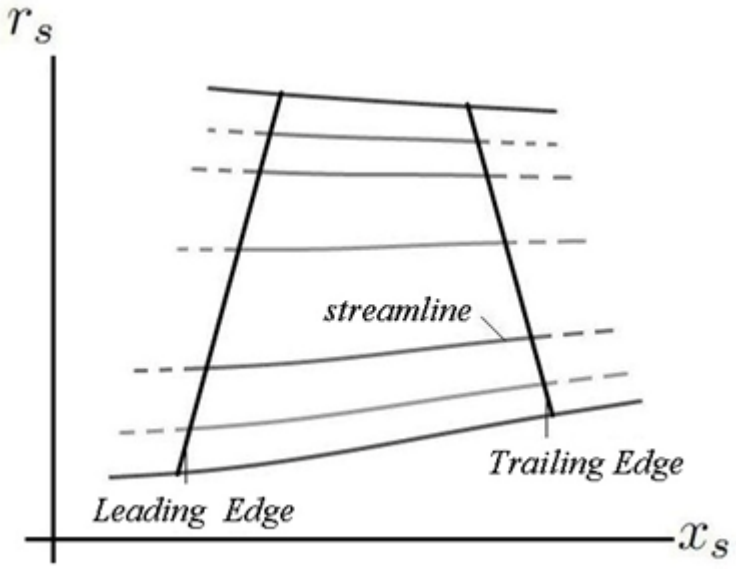

Figure 3.3: Meridional View.[9, 10, 11, 12]

The streamlines or construction lines are defined in the xs, rs plane. 3DBGB[9, 10, 11, 12] has the capability to generate a variety of airfoils. Due to its parametric nature it is easy to define different airfoils at different sections which makes the design process highly flexible. Presently, the code has the capability to create circular sections, NACA

4-digit airfoils, NREL S809 airfoils and the default mixed camber airfoil. New airfoils can also be included in the code.

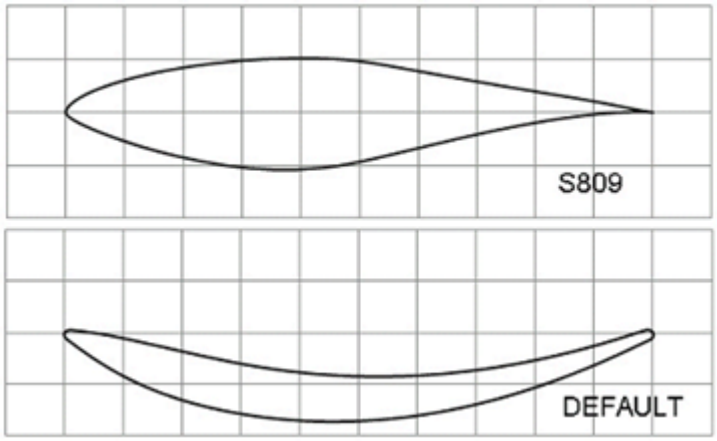

Figure 3.4: 3DBGB generated airfoils. [9, 10, 11, 12]

Using the stacking information and control points, the blade definition can be further altered to produce design features such lean, sweep, bent tips,split tips, etc.

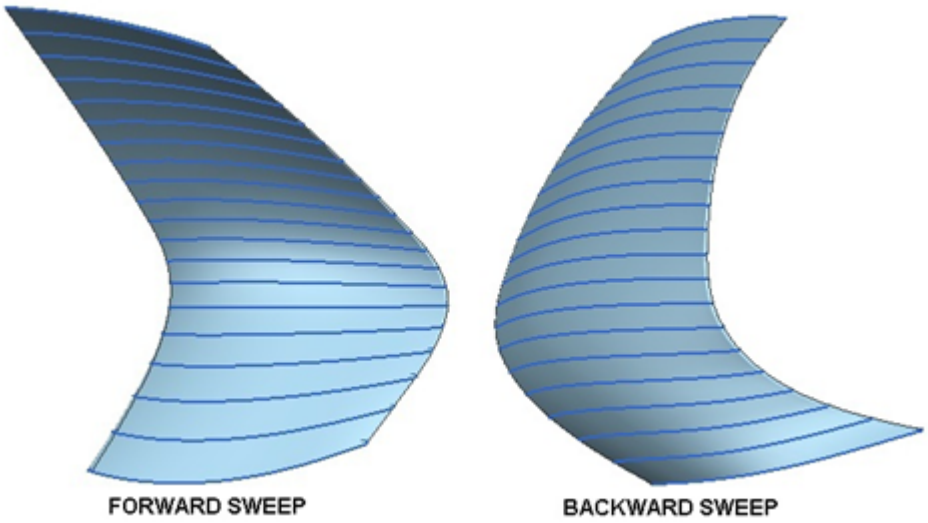

Figure 3.5: Swept Blades.[9, 10, 11, 12]

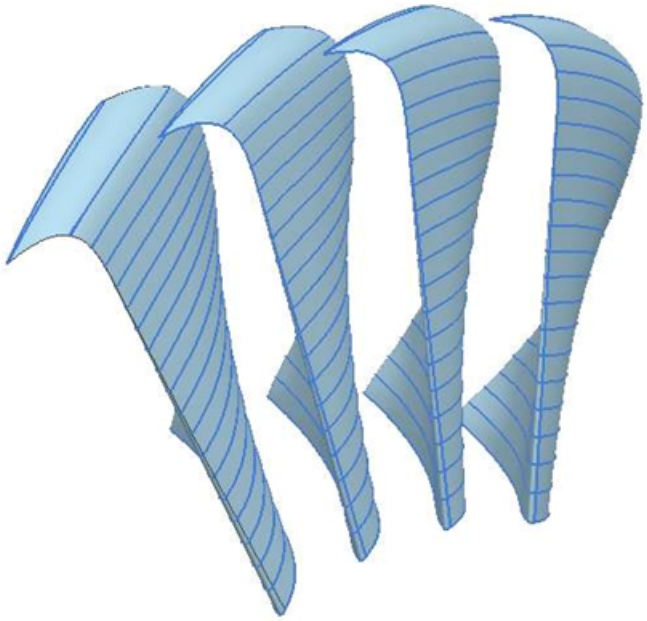

Figure 3.6: Leaned Blades. [9, 10, 11, 12]

3.3 Geometry Generation

The steps involved in blade generation for a specific case is shown here but the process remains the same for any blade where the lean has to be adjusted based on the solidity of the blade. The geometry is created using Star-CCM+'s built in CAD tools using 3D parametric curves output from 3DBGB. 3DBGB[9, 10, 11, 12] gives out 3D blade curves, hub, shroud and the periodic boundary curves. There is a built in ability in 3DBGB[9, 10, 11, 12] to apply lean at the blade. This enables us to apply a defined amount of lean on specific span locations on the blade. The blade consists of 2 parts, the positive lean and the negative lean. The blade is leaned tangentially as described by Denton[17]. Figure 3.7 shows the blade leaned both tangentially and in normal direction to the chord.

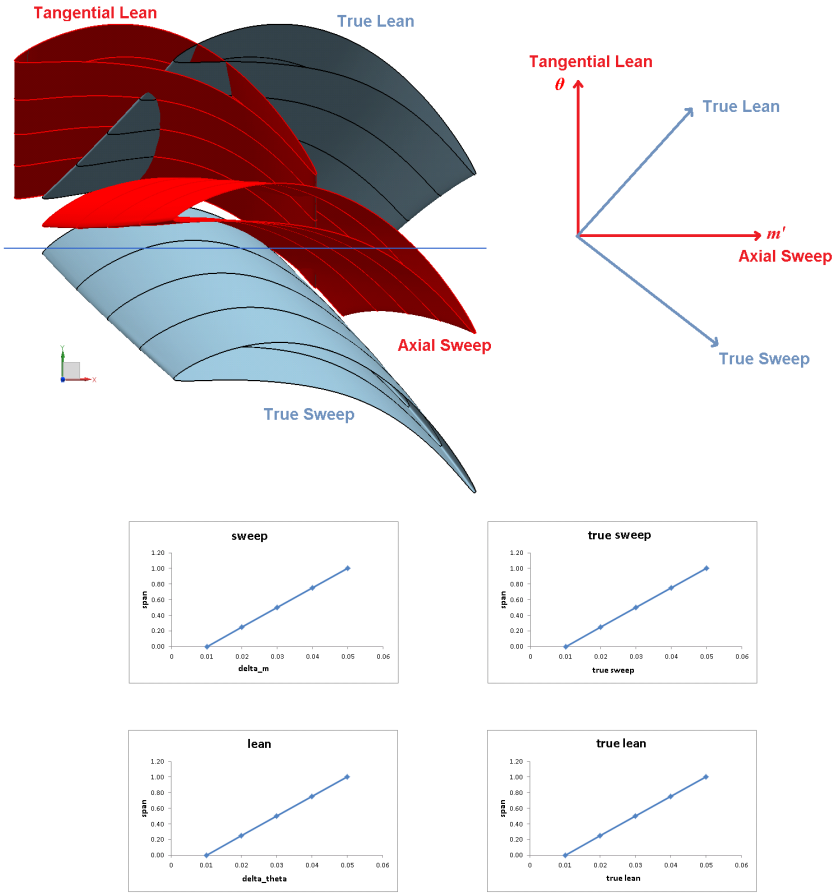

Figure 3.7: True lean and tangential lean.[13]

Figure 3.8 describes the steps involved in the geometry generation process.

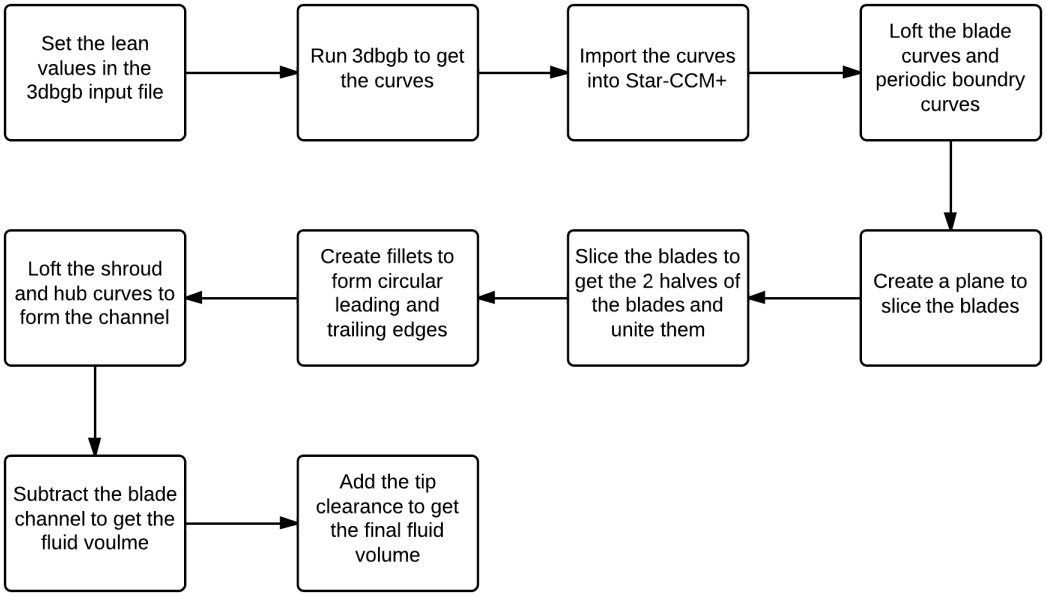

Figure 3.8: Flow chart describing the geometry generation process.

Two identical blades are leaned starting at 80% span. Table 3.1 shows the lean defined for the blade and Figure 3.9 shows the variation of lean along the span of the blade. Figure 3.10 shows two blade leaned in opposite directions.

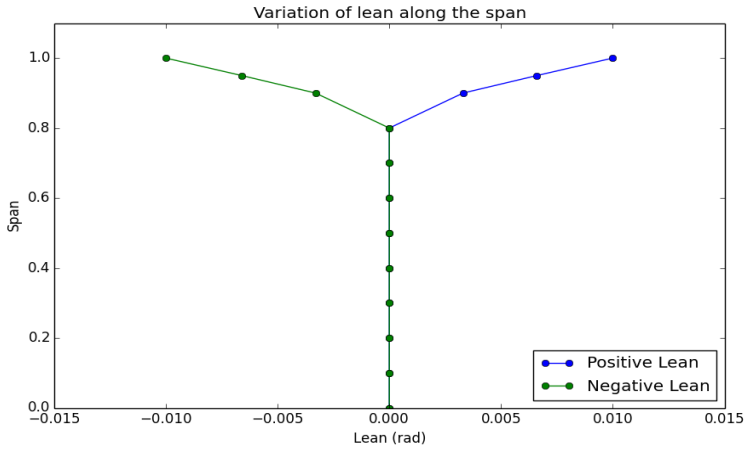

Figure 3.9: Variation of lean.

Span	Lean(radians)
0.0	0.0
0.1	0.0
0.2	0.0
0.3	0.0
0.4	0.0
0.5	0.0
0.6	0.0
0.7	0.0
0.8	0.0
0.9	0.0033
0.95	0.0066
1.0	0.01

Table 3.1: Variation of Lean.

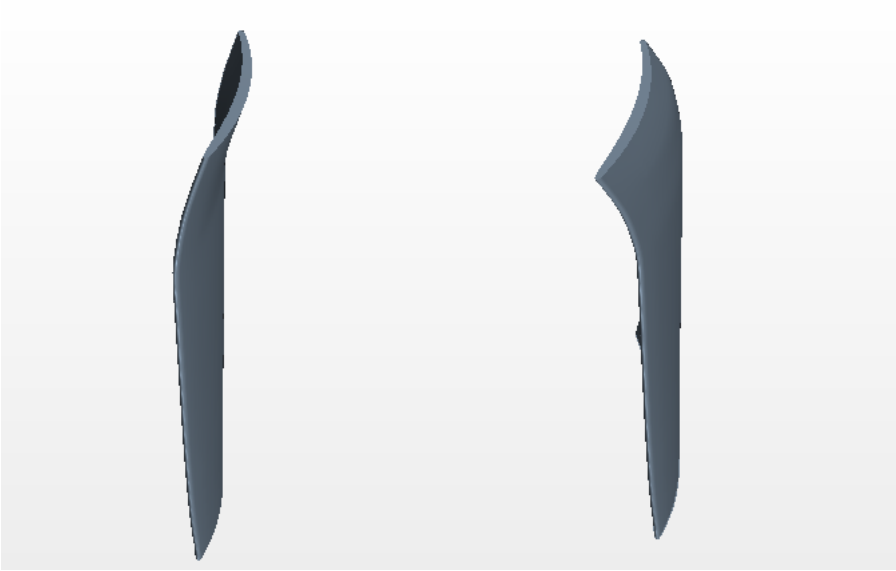

Figure 3.10: Blades with Positive and Negative lean.

The 3D blade curves along with the hub, shroud and the periodic boundary is imported into Star-CCM+©[14] using java macros. Circles with radii equal to that of the hub and shroud radius are created as splines and imported along with the other curves which is later used to form the fluid volume. Figure 3.11 shows the curves imported into Star-CCM+©.

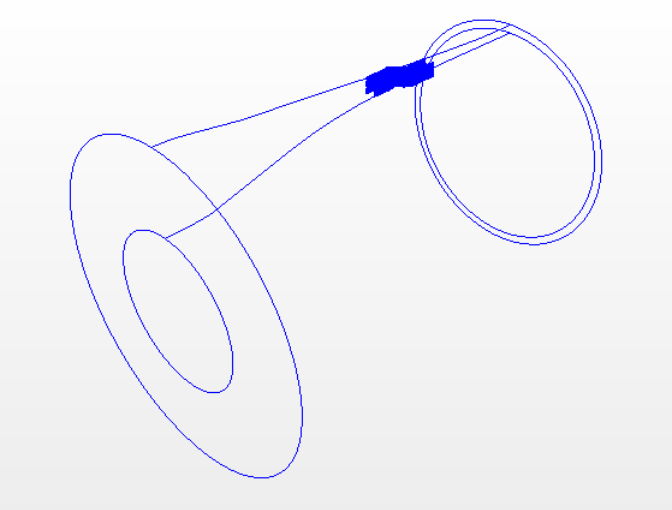

Figure 3.11: Curves imported in Star-CCM+.

The 2 blade curves are then lofted to form the solid blade. The periodic curves are also lofted to form a sheet element which is then later used to slice the fluid volume.

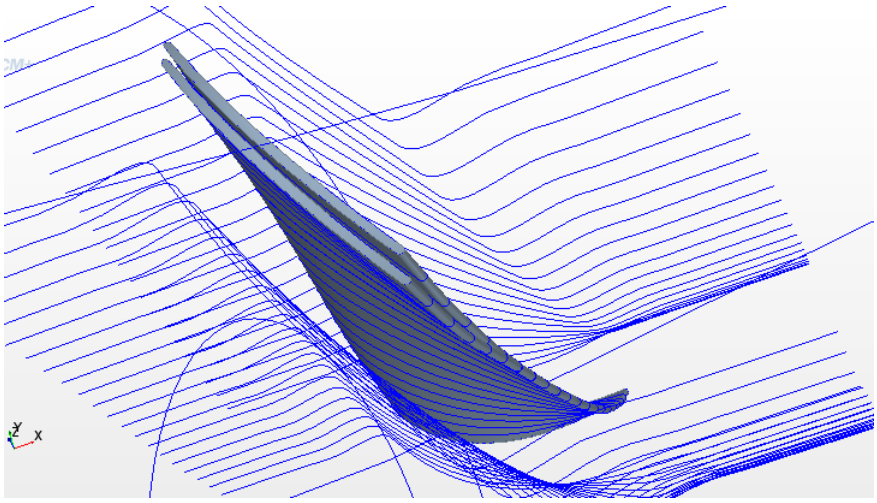

Figure 3.12: Lofted blade.

The lofted blades need to be sliced into 2 halves to form the split tip. To do this a sheet surface is created at mid chord of the blade. The first blade is sliced leaving only the positive lean part and the 2nd blade is sliced to get the negative lean part of the blade. The 2 halves of the blade are then united to form a single part which forms the blade.

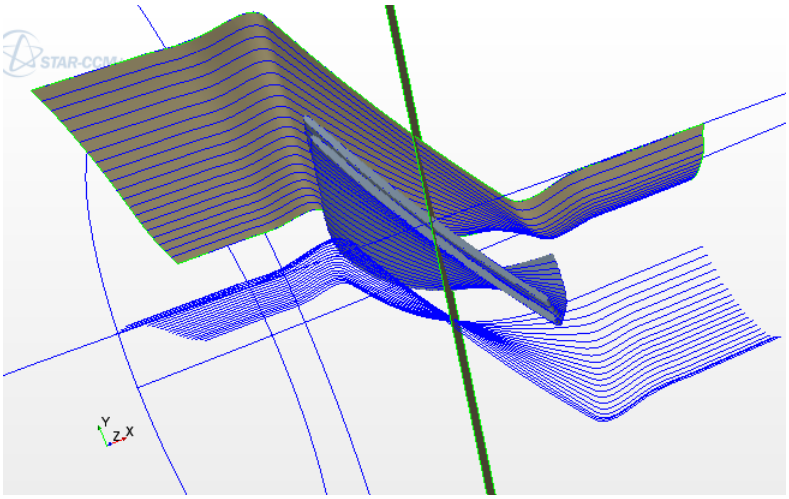

Figure 3.13: Sheet used to slice the blade.

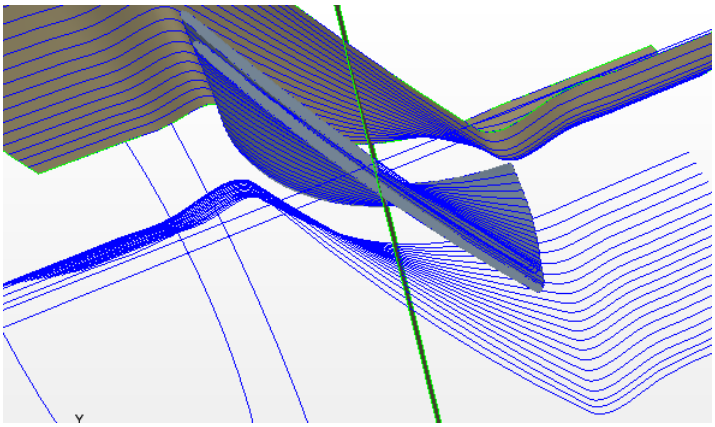

Figure 3.14: One and a half leaned blades.

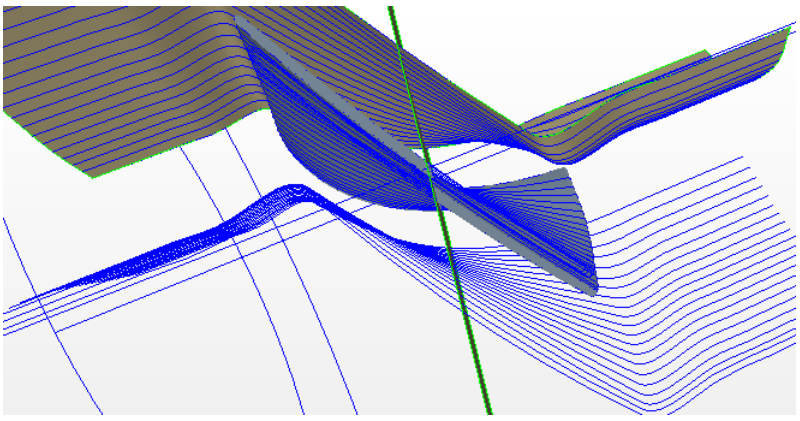

Figure 3.15: Two half blades.

The sliced blades have blunt trailing edge for the first half and a blunt leading edge for the second half. The blunt edges can cause separation and have to be rounded. Fillets

are created at the edges to create circular leading edge and circular trailing edge. The fillets are of radius of 0.5mm each.

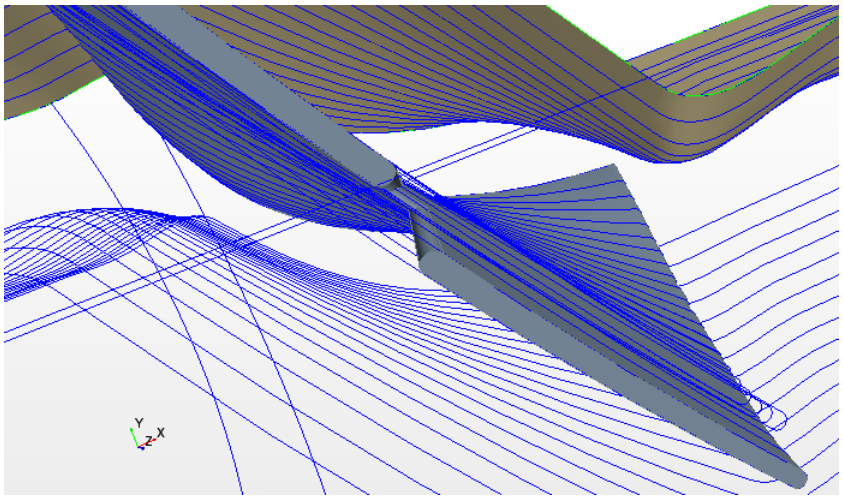

Figure 3.16: Filleted blade.

Once the geometry of the blade is completed, the fluid volume needs to be generated. First, the two shroud circles are lofted using the shroud curve as a guide. The blade volume is then subtracted from the larger volume using boolean subtraction.

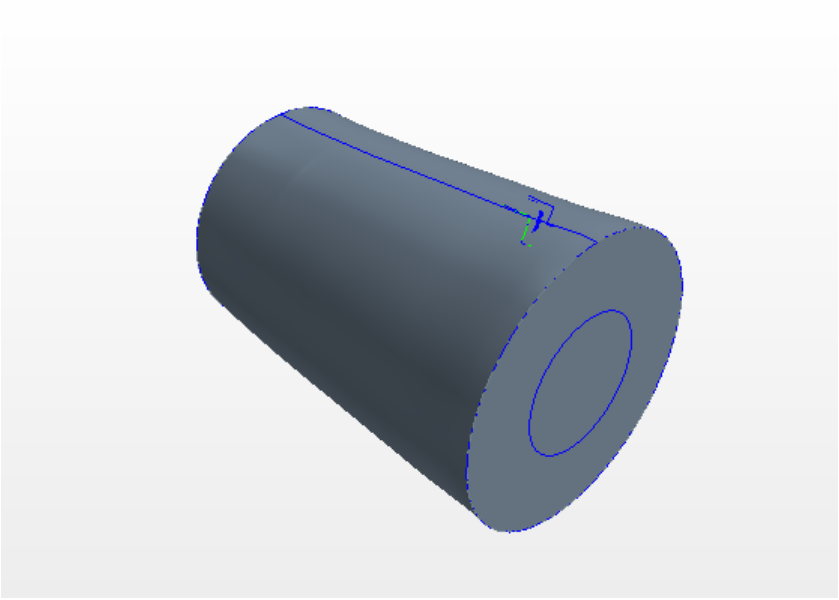

Figure 3.17: Lofted Fluid Volume.

Then the smaller hub circles are lofted using the hub curve as a guide. Lofted cut operation is used to delete this volume from the larger volume to get the full annulus fluid channel.

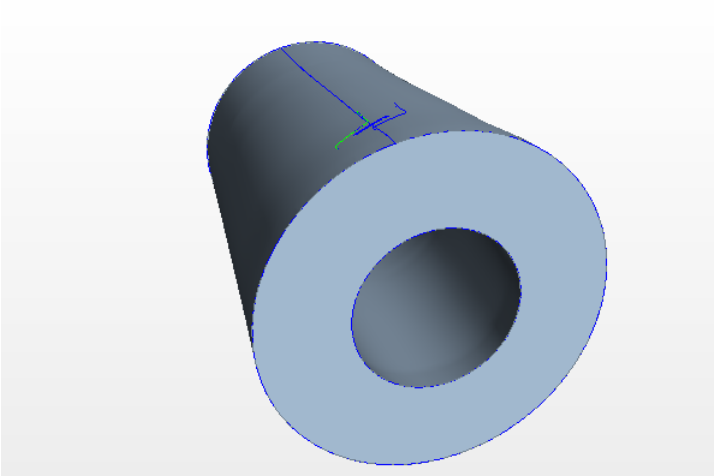

Figure 3.18: Full Channel Length.

To generate the tip clearance the shroud curve is projected onto a sketch and a duplicate of it offset by 0.5 mm which is the tip clearance for the EEE stage 6 rotor blade[18]. This sketch is then used to perform a revolve cut about the engine axis to remove the blade part and the sketch is revolved again to get the solid volume to generate the tip clearance. The fluid volume is then sliced using the periodic boundary sheets to create a single channel for the simulation. The length of the channel is then reduced by performing extrude cut operation both at the inlet and outlet as we are using only a single blade for this simulation. Figure 3.20 and 3.21 shows the final geometry of the channel which is later meshed to solve for the results.

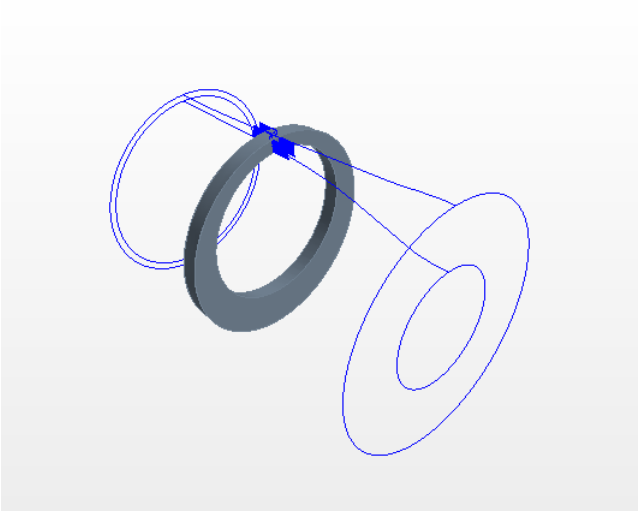

Figure 3.19: Reduced Channel Length.

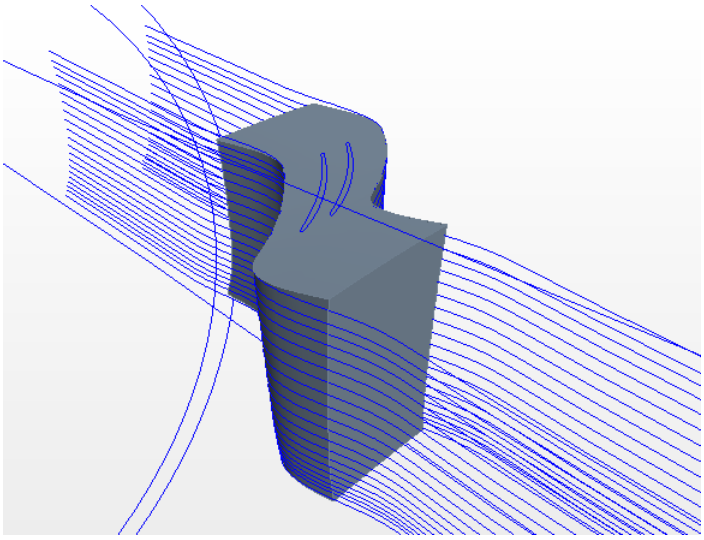

Figure 3.20: Final Fluid Volume.

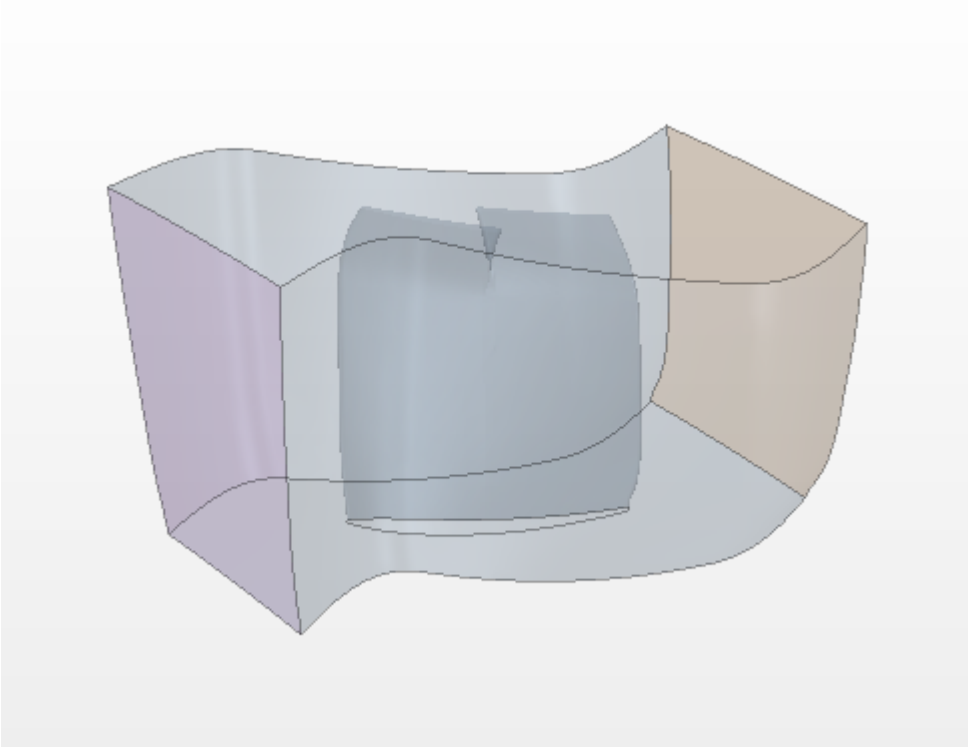

Figure 3.21: Final Fluid Volume.

3.4 Mesh Generation

A mesh is the discretized representation of the computational domain, which the physics solvers use to provide a numerical solution. A good mesh is required to obtain good cfd results. Since the geometry is very complex, generating a structured mesh is very tedious and very time consuming. Unstructured meshes enable us to generate meshes easily for such complex bodies even though they are more resource intensive. Unstructured meshes use either polyhedrals or tetrahedrals as the cells to generate the volume mesh. Prism layers are used near to capture the boundary layer flows. Star-CCM+©'s automatic unstructured mesh generator helps us to easily generate the mesh for our complex geometry.

The polyhedral mesher, Surface remesher, Surface Wrapper and Prism layer meshing models were used to generate the mesh. The surface remesher remeshes the initial surface to provide a quality discretized mesh that is suitable for CFD[19]. The surface wrapper can be used to provide a closed, manifold, non-intersecting surface when starting from poor quality CAD data. Since our geometry has multiple intersecting parts, the surface wrappers ensures proper intersection of the parts for the Volume mesher to process.

The polyhedral mesher generates volume mesh composed of polyhedral shaped cells. A major advantage of polyhedral cells is that they have many neighbors (typically of the order of 10), so gradients can be much better approximated (using linear shape functions and the information from nearest neighbors only). Even along wall edges and at corners, a polyhedral cell is likely to have a number of neighboring cells, thus allowing for a reasonable prediction of both gradients and local flow distribution. The fact that more neighboring cells means more storage and computing operations per cell is more than compensated for by a higher accuracy in the final solution. A base size of 0.5 mm was used for meshing. The areas having curvature was defined using a unit circle with 501 points on the circumference. This gives good mesh definition around the leading and trailing edges.

The prism layer mesher adds prismatic cell layers next to wall boundaries. The mesher projects the core mesh back to the wall boundaries to create prismatic cells. 7 prism layers were used to accurately capture the boundary layer flows. The extent to which the prism layers stretch can be controlled by the prism layer stretching factor. After couple of tests it was found that a stretching factor of 1.5 was optimal. Figure 3.22 shows the mesh near the boundary layer and Figure 3.23 shows the full mesh of the fluid volume.

Grid dependency study was done and the chosen grid was is a balance between speed and accuracy. The grid had a mean Y+ value of 14 as shown in figure 3.24.

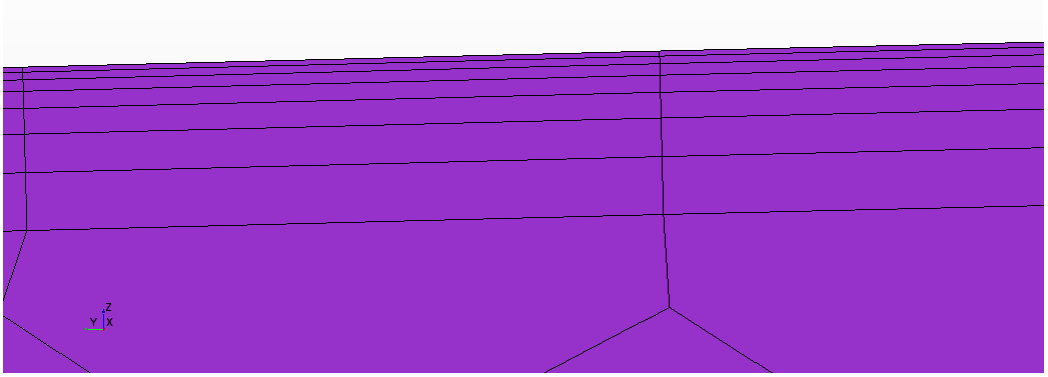

Figure 3.22: Prism layers near the boundary.

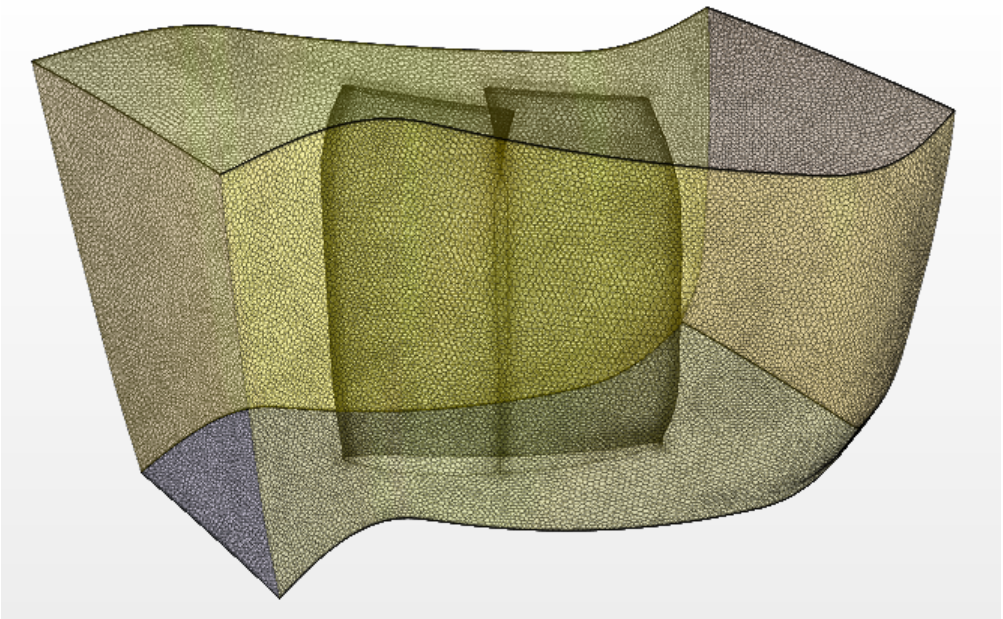

Figure 3.23: Fluid volume mesh.

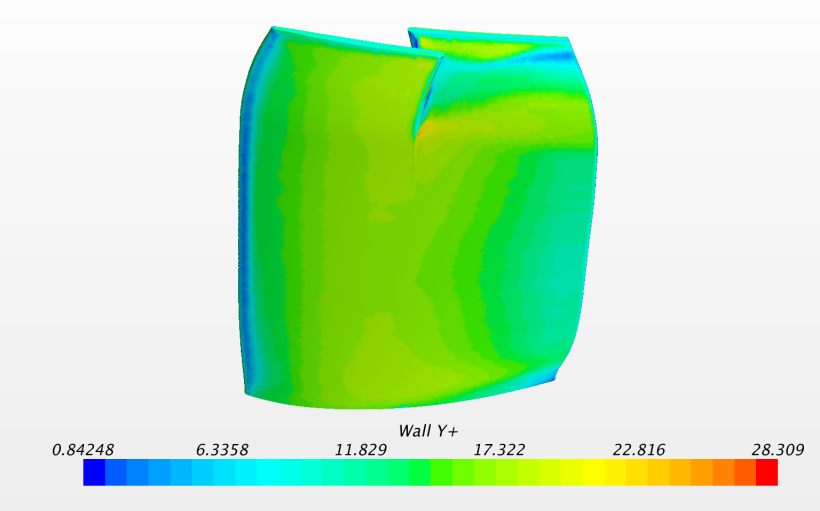

Figure 3.24: Y+ values.

3.5 Physics Modeling

A physics model in Star-CCM+©defines how a physical phenomenon in a continuum is represented. Essentially, physics models define the primary variables of the simulation (such as pressure, temperature, and velocity) and what mathematical formulation is used to generate the solution. An appropriate combination of models is necessary for the complete definition of a physics continuum. The following physics models were used in the simulation.

- 3D Steady
- Reynolds-Averaged Navier-Stokes
- Coupled Flow
- Coupled Energy
- Spalart-Allmaras Turbulence
- Gamma(γ) of 1.37836 was used.

3.6 Boundary Conditions

- A stagnation inlet boundary condition was set at the inlet with Total Pressure, Figure 3.25a, and Total Temperature, Figure 3.25b, profiles imposed.
- A pressure outlet boundary condition was set at the outlet with radial equilibrium pressure distribution with static pressure imposed at the hub.

- Periodic boundaries had a periodicity of 4.5^0.
- A rotating motion of 12300 rpm was imposed on the blade and hub boundary.
- Inlet swirl was imposed in terms of velocity components at the inlet, Figure 3.26a, Figure 3.26b, Figure 3.26c.
- Turbulence Viscosity ratio of 500 was imposed throughout the domain.

All these boundary conditions were held constant for each of the cases.

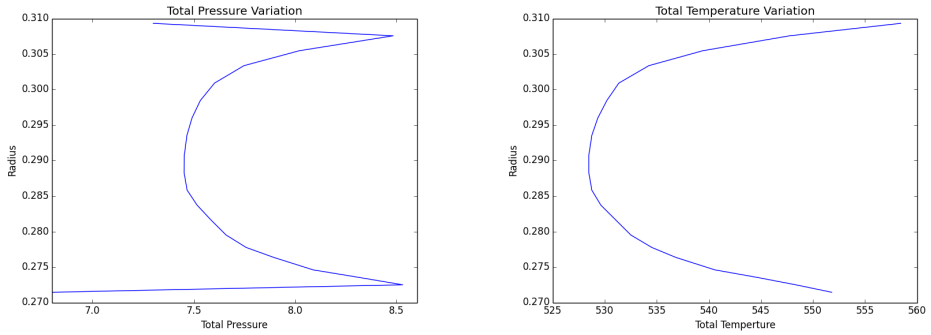

(a) Inlet Total Pressure (b) Inlet Total Temperature

Figure 3.25: Inlet Boundary Conditions

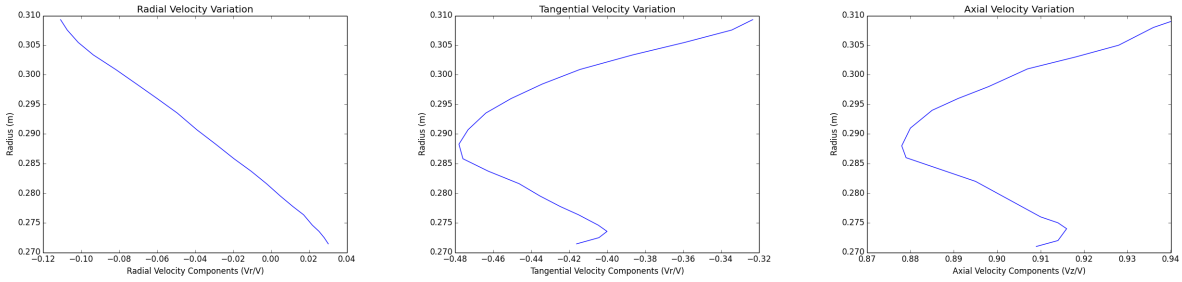

(a) Radial Velocity Components (b) Tangential Velocity Components (c) Axial Velocity Components

Figure 3.26: Inlet Velocity Components

Chapter 4

Results

4.1 CFD Analysis

4.1.1 Grid Dependency Study

A Grid dependency study was done. Initially when the grid was created due to the way the geometry was created there was a clustering at mid span and all the results shown here are with this clustering. This was later eliminated by using an extra meshing module called surface wrapper as explained in the mesh generation in Chapter 3. A case with the clustered and unclustured grid has been studied to show that the clustering doesn't affect the results. Also a case with twice the number of prism layers was run to check the effect of prism layers. Five different mesh cases were run

- Very Coarse mesh with base cell size of 1mm.
- Coarse mesh with base cell size of 0.5 mm.
- Coarse mesh with base cell size of 0.5 mm. (With clustering)
- Fine mesh with base cell size of 0.25mm.
- Fine mesh with base cell size of 0.25mm with twice the number of prism layers.

The results are tabulated in table 4.1 .

Case	No of cells	PR	TR	Mass flow rate (kg/s)	Efficiency
Very Coarse	570923	1.301429	1.086778	0.680302	90.0928
Coarse	2314144	1.303002	1.086002	0.6874376	91.3384
Coarse with grid clustering	1719696	1.300728	1.085501	0.6855353	91.2442
Fine	10049545	1.304402	1.085657	0.6913875	92.0927
Fine(2x prism layers)	10226494	1.306464	1.086245	0.6926658	92.0295

Table 4.1: Grid Dependency Study.

Case	Relative Mass Flow Rate	Relative Efficiency
Very Coarse	-1.8245%	-1.9367
Coarse	-0.7547%	-0.6911
Coarse with grid clustering	-1.0294%	-0.7853
Fine	-0.1845%	0.0632
Fine(2x prism layers)	0	0

Table 4.2: Relative Values of Grid Dependency Study.

From the grid dependency study results since the difference between the coarse grid and fine grid is small and the time required for the fine grid case is much larger than the time required for the coarse grid, the coarse mesh with the grid clustering was used.

4.1.2 Speedlines

Simulations were run for 5 different tip clearances 0.625% span, 1.25% (Baseline), 2.5%, 3.75%, 5% (0.5x, 1x, 2x, 3x, 4x). The back pressure was increased until there was reverse flow at the inlet on 200+ faces. At this point it was determined that the compressor had stalled. Figure 4.1 show the speedline for pressure ratio and figures 4.2 to 4.6 shows the speedlines for the individual cases.

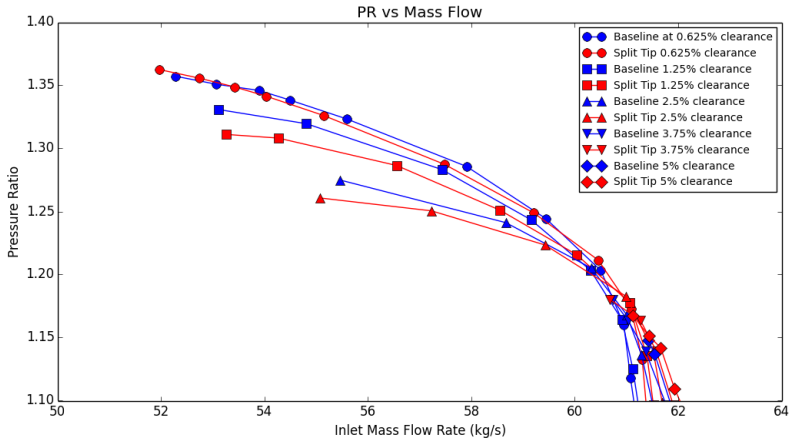

Figure 4.1: Pressure ratio speedline.

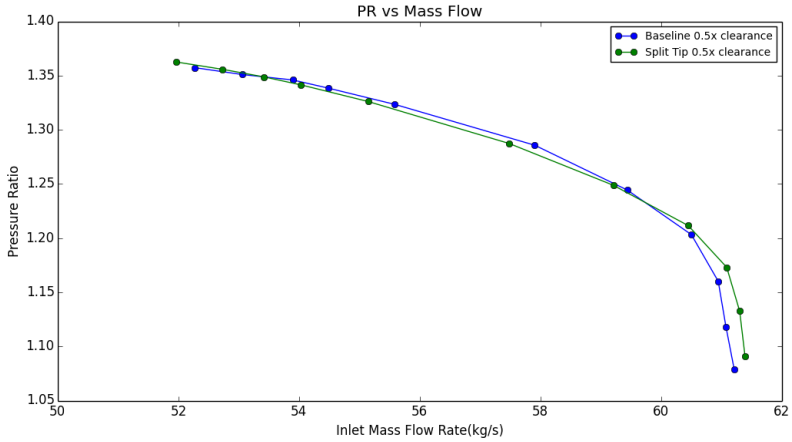

Figure 4.2: Pressure ratio speedline for 0.625% clearance.

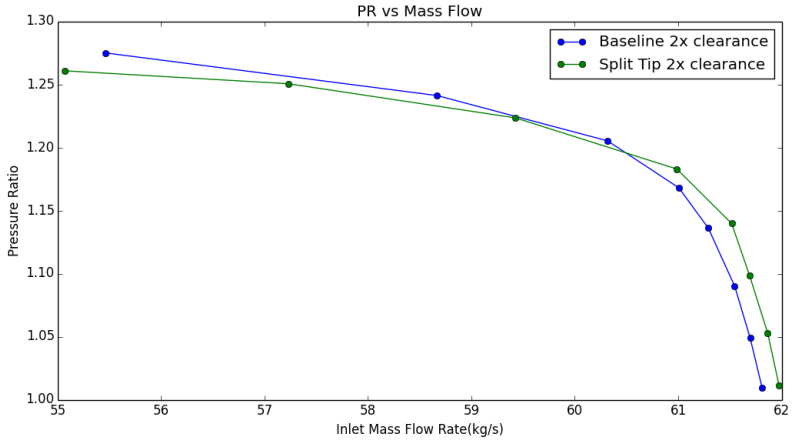

Figure 4.3: Pressure ratio speedline for 1.25% clearance.

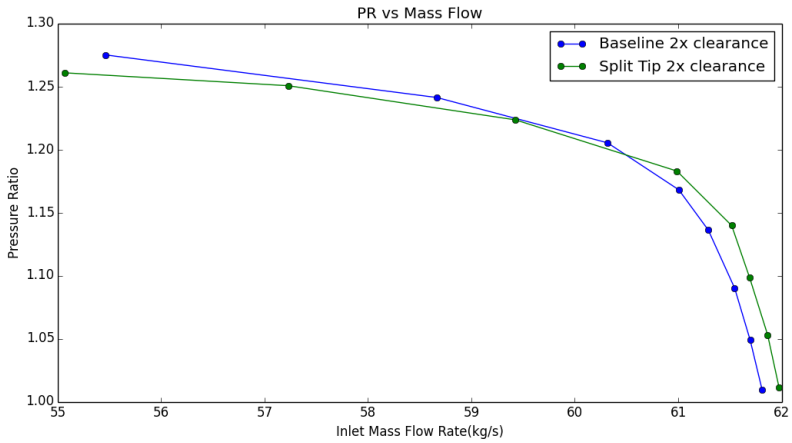

Figure 4.4: Pressure ratio speedline for 2.5% clearance.

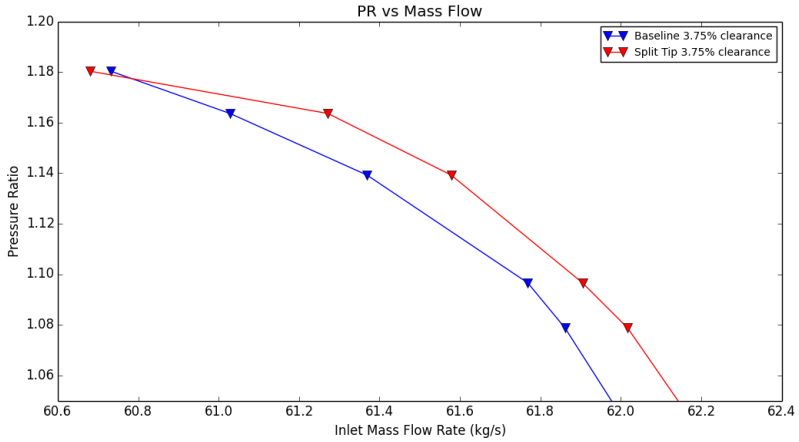

Figure 4.5: Speedline for 3.75% clearance case.

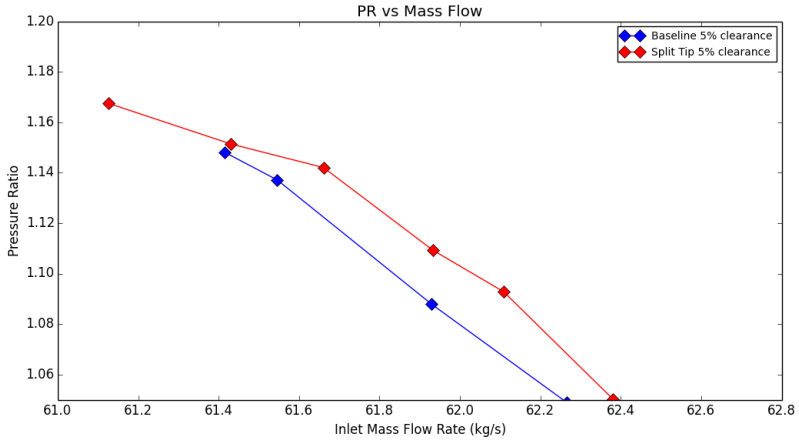

Figure 4.6: Speedline for 5% clearance case.

Figure 4.7 shows the efficiency speedlines for all five clearance cases and figures 4.8 to 4.12 show the individual speedline for each case.

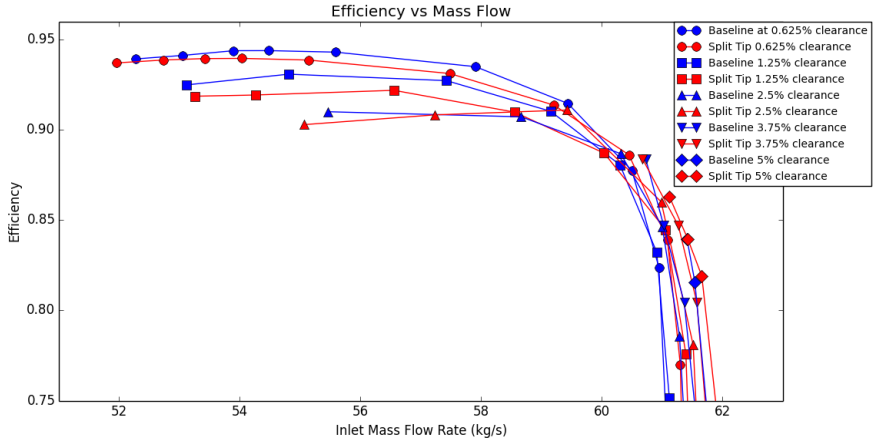

Figure 4.7: Efficiency Speedline.

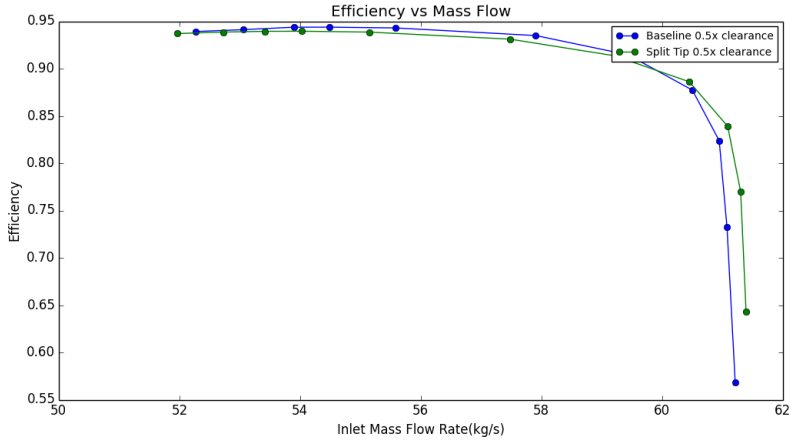

Figure 4.8: Efficiency Speedline for 0.625% clearance case.

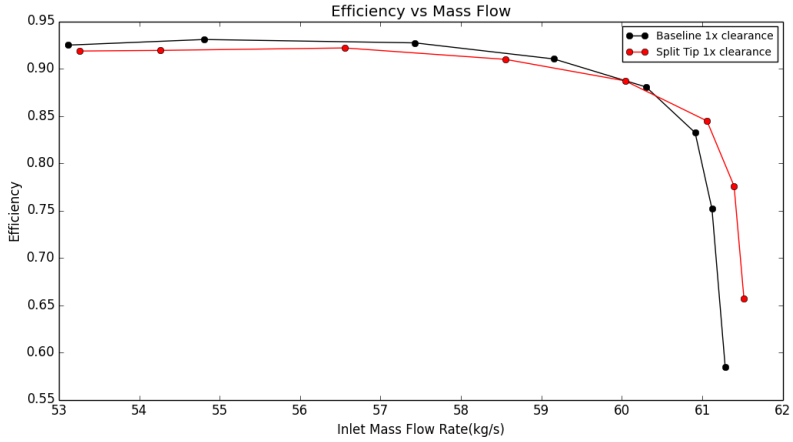

Figure 4.9: Efficiency Speedline for 1.25% clearance case.

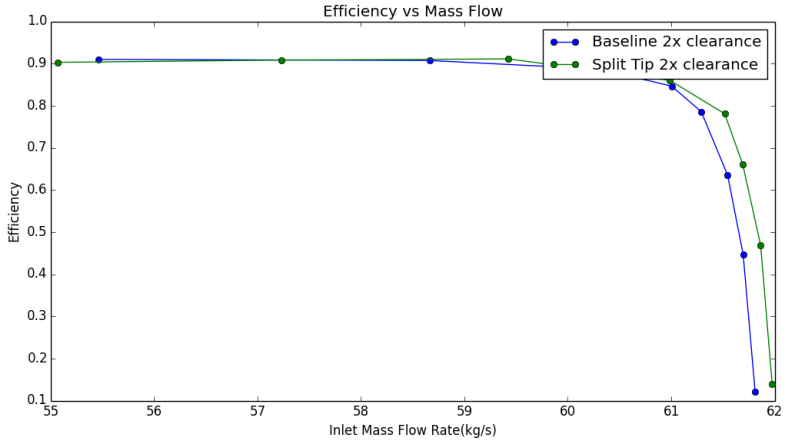

Figure 4.10: Efficiency Speedline for 2.5% clearance case.

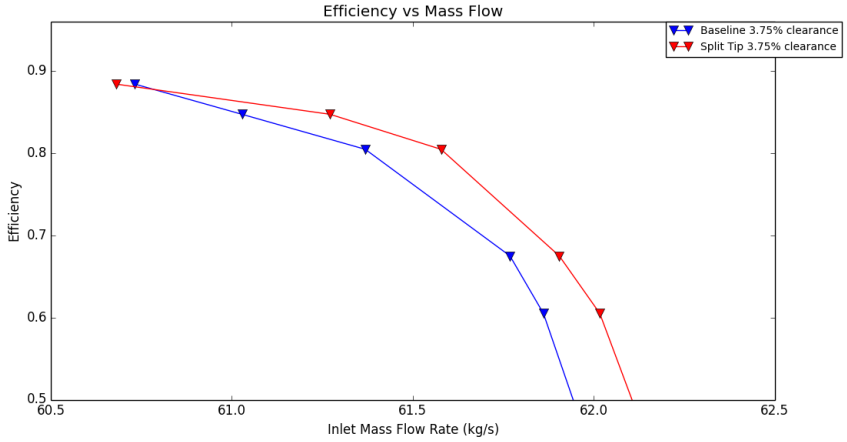

Figure 4.11: Efficiency Speedline for 3.75% clearance case.

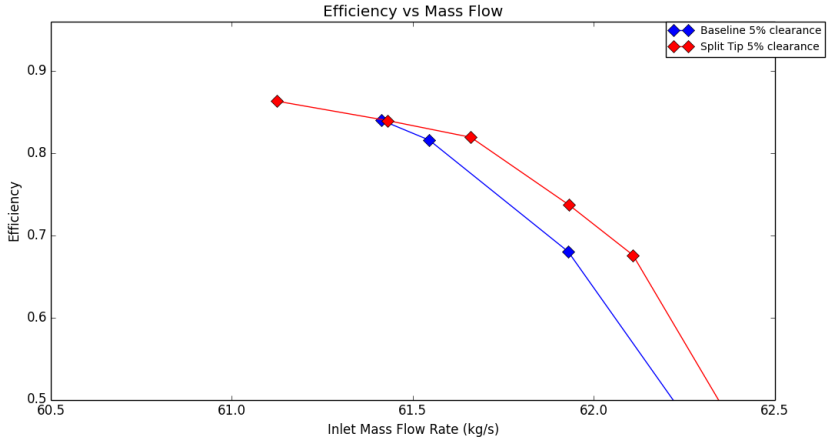

Figure 4.12: Efficiency Speedline for 5% clearance case.

From the above plots it can been seen that the split tip case has higher operating range than the baseline case. Also it can be seen that close to choke the split tip case has higher pressure ratio and mass flow rate compared to the baseline case but closer to stall the baseline case performs better. Also the efficiency of the split tip case is higher near the choke and close to stall it drops down compared to the baseline.

4.1.3 Tip Clearance Trends

A tip clearance study was conducted to study the effect of tip clearance on peak efficiency of the rotor. Figure 4.13 shows the variation of peak efficiency versus tip gap/blade height ratio.

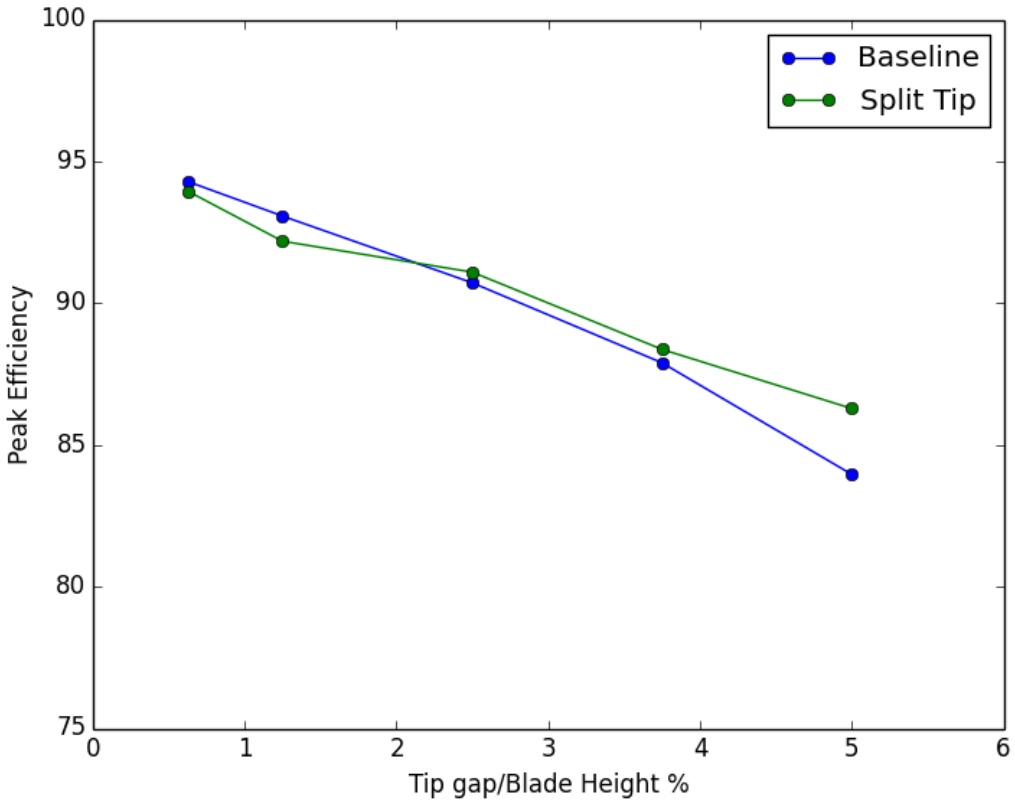

Figure 4.13: Variation of Peak efficiency.

From the above figure it is seen that at tight clearances the baseline case has higher peak efficiency than the split tip case and performs better. But as the tip clearance is increased, the split tip has a higher peak efficiency and performs better than the baseline case. From this it can be said that the split tip case is much better suited for higher clearances.

4.1.4 Combined Quantity Speedlines

Mattingly[20] defines the mass flow parameter(MFP) as

$$MFP = \frac{\dot{m}\sqrt{T_T}}{P_T A} \tag{4.1}$$

and is only a function of mach number and other texts might refer to this as flow function. The corrected mass flow rate at a station i is defined as

$$\dot{m}_{ci} = \frac{\dot{m}_i\sqrt{\theta_i}}{\delta_i} \tag{4.2}$$

where $\theta = \frac{T_T}{T_{ref}}$, $\delta = \frac{P_T}{P_{ref}}$, $T_{ref} = 288.15K$ and $P_{ref} = 1atm$.

A combined quantity used at Rolls Royce[21] is obtained by dividing the pressure ratio by the corrected inlet mass flow rate as shown in Equation 4.3

$$CQ = \frac{\pi}{\frac{\dot{m}\sqrt{\theta_i}}{\delta_i}} \tag{4.3}$$

Some such as Cumpsty[22] consider exit corrected flow as an important parameter, although the results here have not been presented that way. If we consider a multistage compressor with N stages. The outlet flow from stage n is the inlet flow to stage n+1. In selecting the annulus height and the blade angles for stage n+1, the pressure and temperature rises in stages 1, though N will have been considered to arrive at the intended corrected mass flow into stage n+1. If, for example, the flow from stage n has a blockage greater than the value assumed in the design, then the pressure rise it produces will be lower than the design and the corrected mass flow into stage n+1 will be higher than the design. As a result stage n+1 will produce a lower pressure rise than intended in the design, and, in extreme cases, may choke. Likewise, if the pressure rise in the stages up to stage n exit is higher than the design, then the corrected mass flow into stage n+1 will be lower than the design and the stage may stall.

The Combined Quantity is then plotted against efficiency. Figures 4.14 to 4.19 shows the Combined Quantity plots.

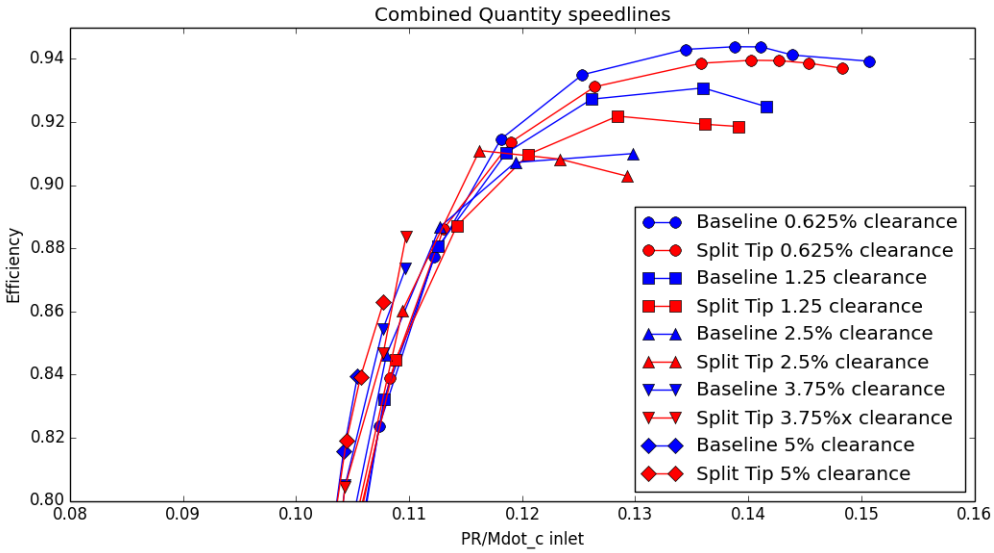

Figure 4.14: Combined Quantity Speedline.

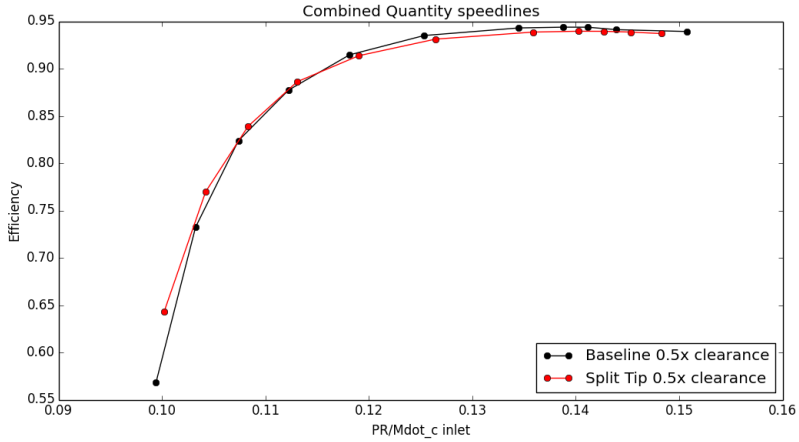

Figure 4.15: Combined Quantity speedline for 0.625% clearance.

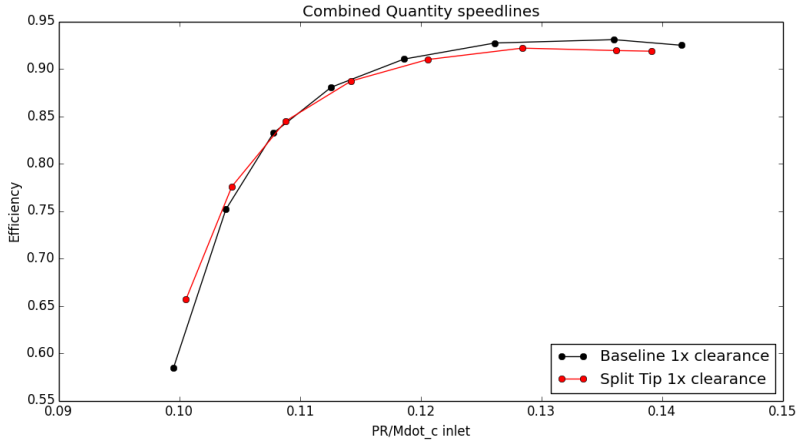

Figure 4.16: Combined Quantity speedline for 1.25% clearance.

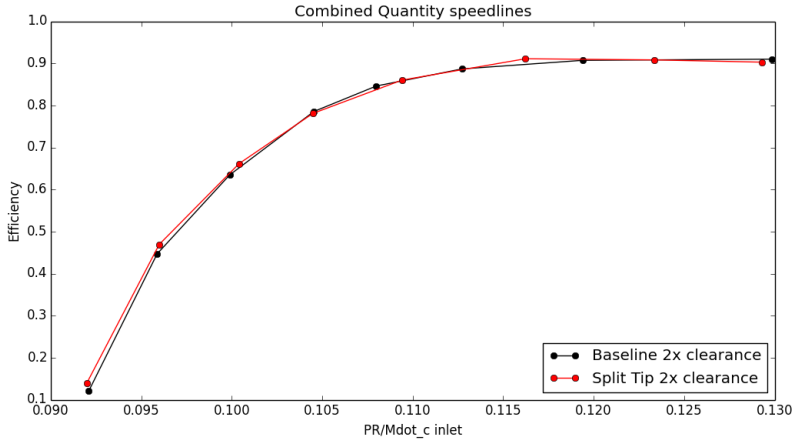

Figure 4.17: Combined Quantity speedline for 2.5% clearance.

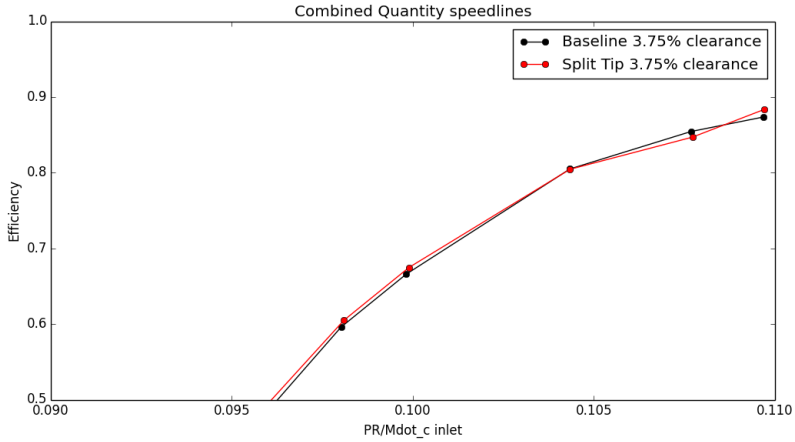

Figure 4.18: Combined Quantity speedline for 3.75% clearance.

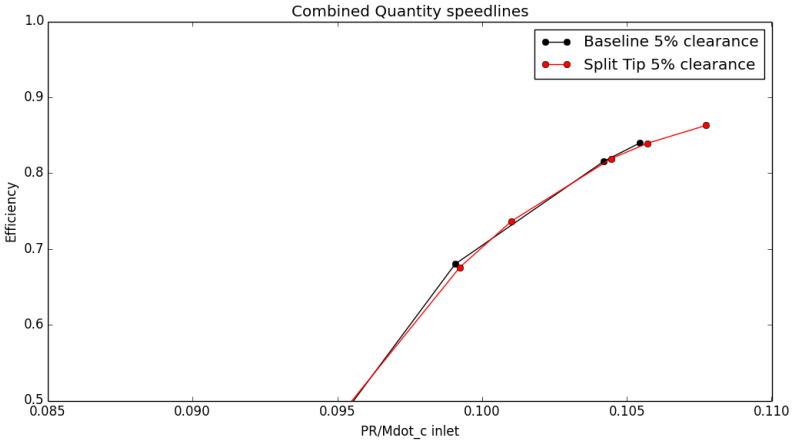

Figure 4.19: Combined Quantity speedline for 5% clearance.

4.1.5 Dihedral Case

Based on the feedback from Brownyn Power a case with just the leaned blade was run to ensure the results shown before is not completely due to the effect of the dihedral. A blade with the same amount of negative lean was created was run at different back pressures for the nominal tip clearance of 1.25%. Figures 4.20 and 4.21 show the pressure ratio and efficiency speedlines for the dihedral case. As expected the dihedral blade had a smaller operating range than the baseline blade similar to Denton [17]. But the efficiency was much higher than the other 2 case and was not matching the results of Denton.

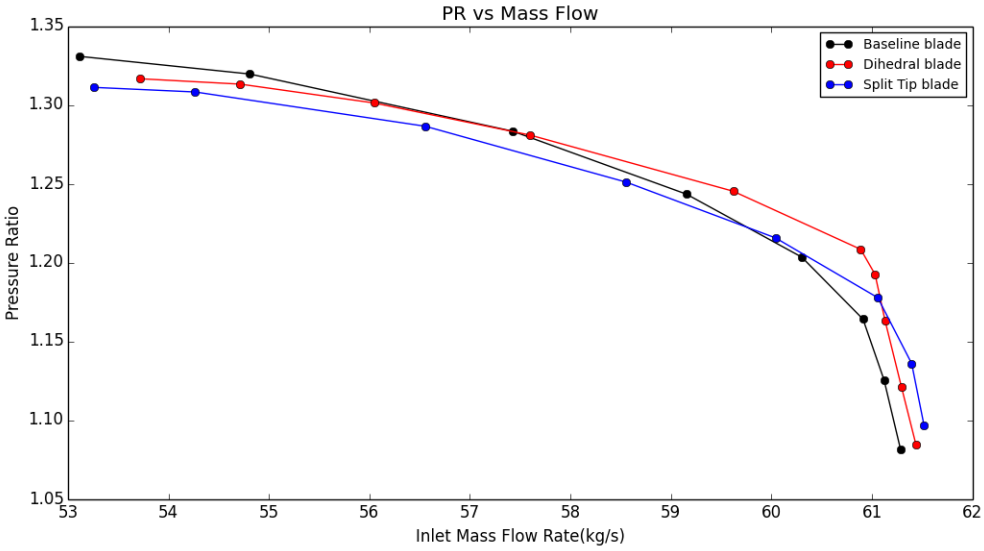

Figure 4.20: Dihedral case Pressure ratio Speedline.

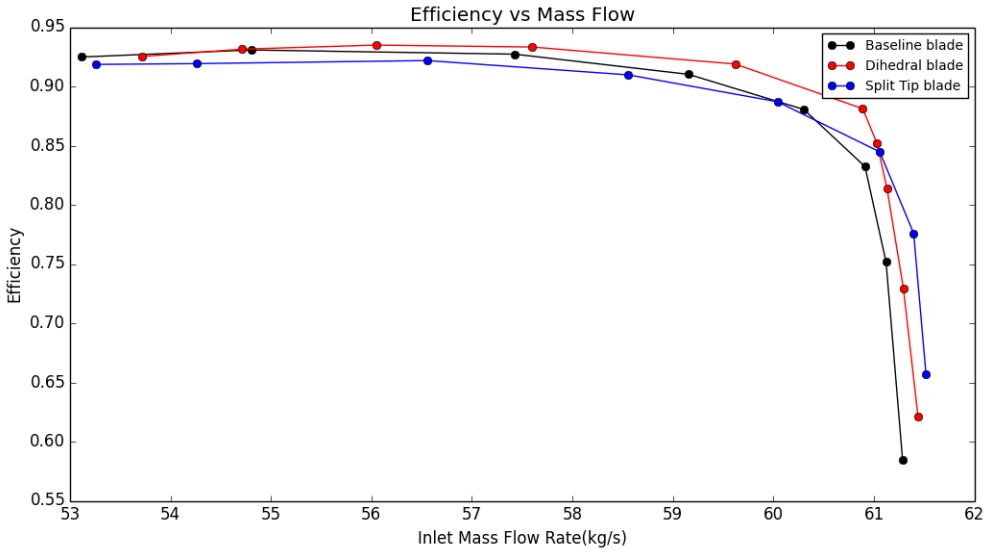

Figure 4.21: Dihedral case Efficiency Speedline.

The Combined Quantity for the dihedral case has been calculated and compared to the baseline and split tip case. Figure 4.22 shows the Combined Quantity speedline .

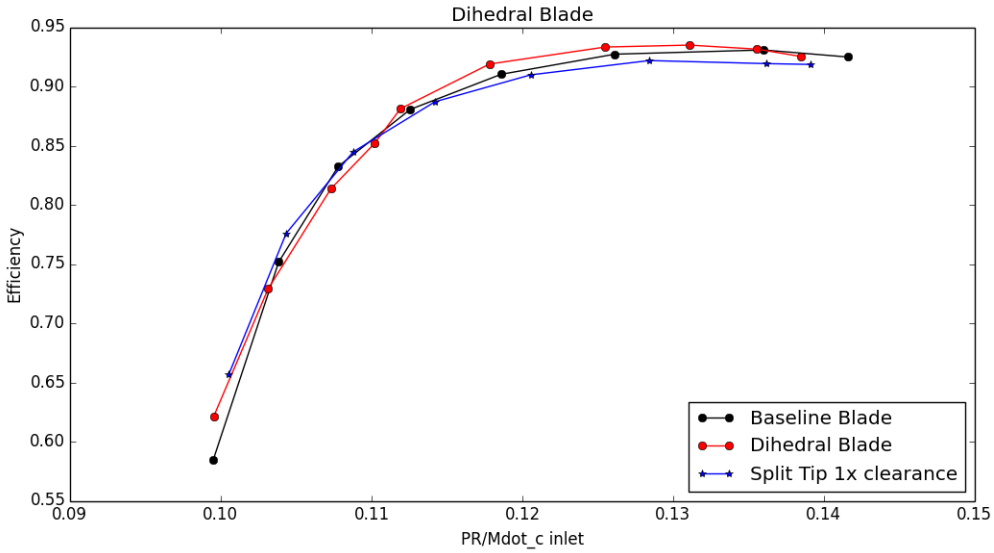

Figure 4.22: Dihedral case Combined Quantity speedline.

4.1.6 Flow Field Description

A brief description of the flow is given here.

Figure 4.23 shows the Relative mach number contours at choke, operating point and stall at 90% span for the 1.25% clearance case.

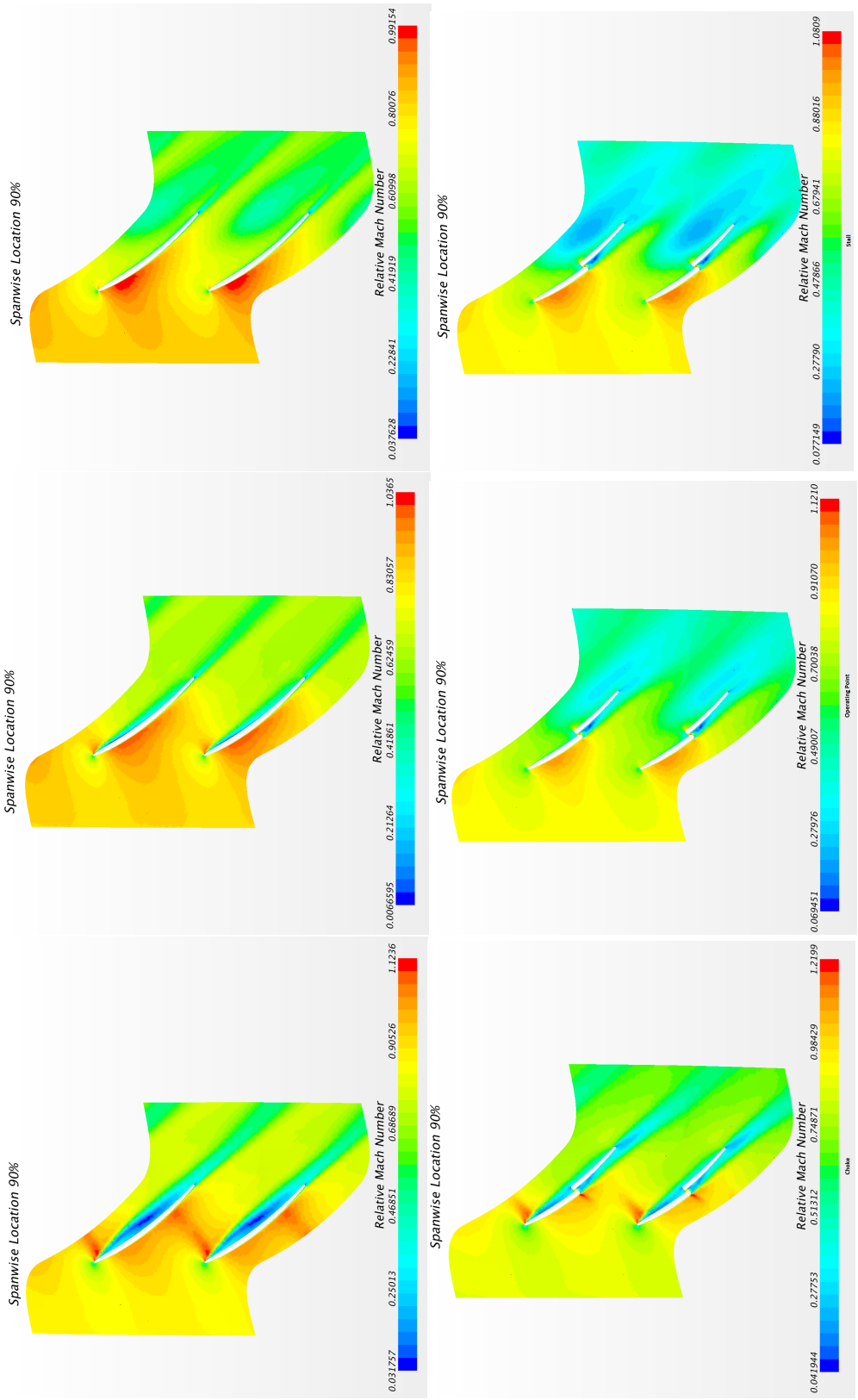

Figure 4.23: Relative mach number contours for 1.25% clearance.

From the figure it can be seen that in the baseline case close to stall the flow has a slightly positive incidence, at choke a negative incidence and close to zero incidence at operating point. The positive incidence at stall is causing high loading on the suction side of the blade. Where as in the split tip case this high loading is slightly reduced due to the dihedral effect. Similarly at choke in the baseline case the negative incidence is causing a positive loading on the pressure side. Where as in the split tip case the loading is smeared out due to the dihedral effect. Similar effect can be seen for the other tip clearance cases.

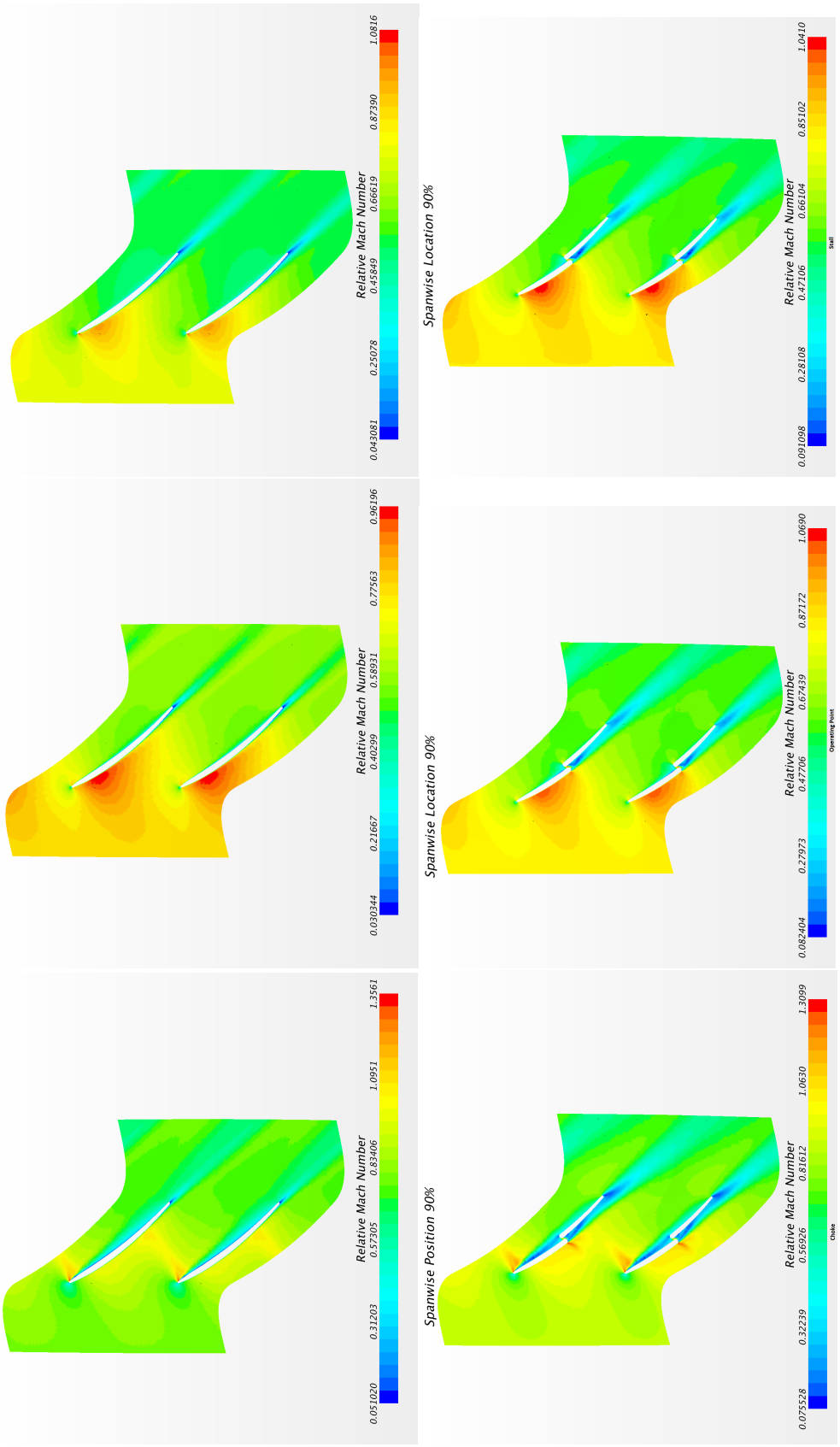

Figure 4.24: Relative mach number contours for 0.625% clearance.

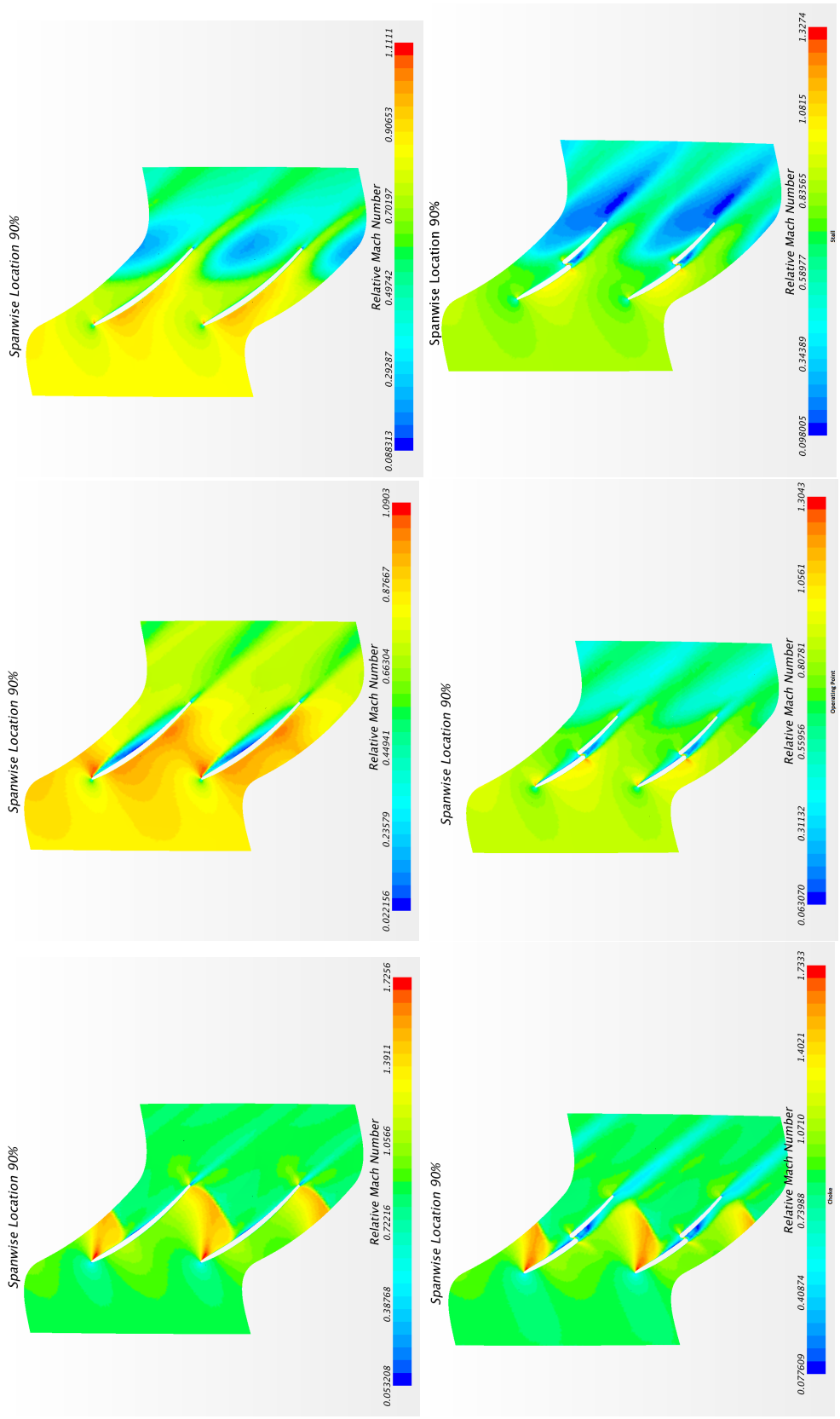

Figure 4.25: Relative mach number contours for 2.5% clearance.

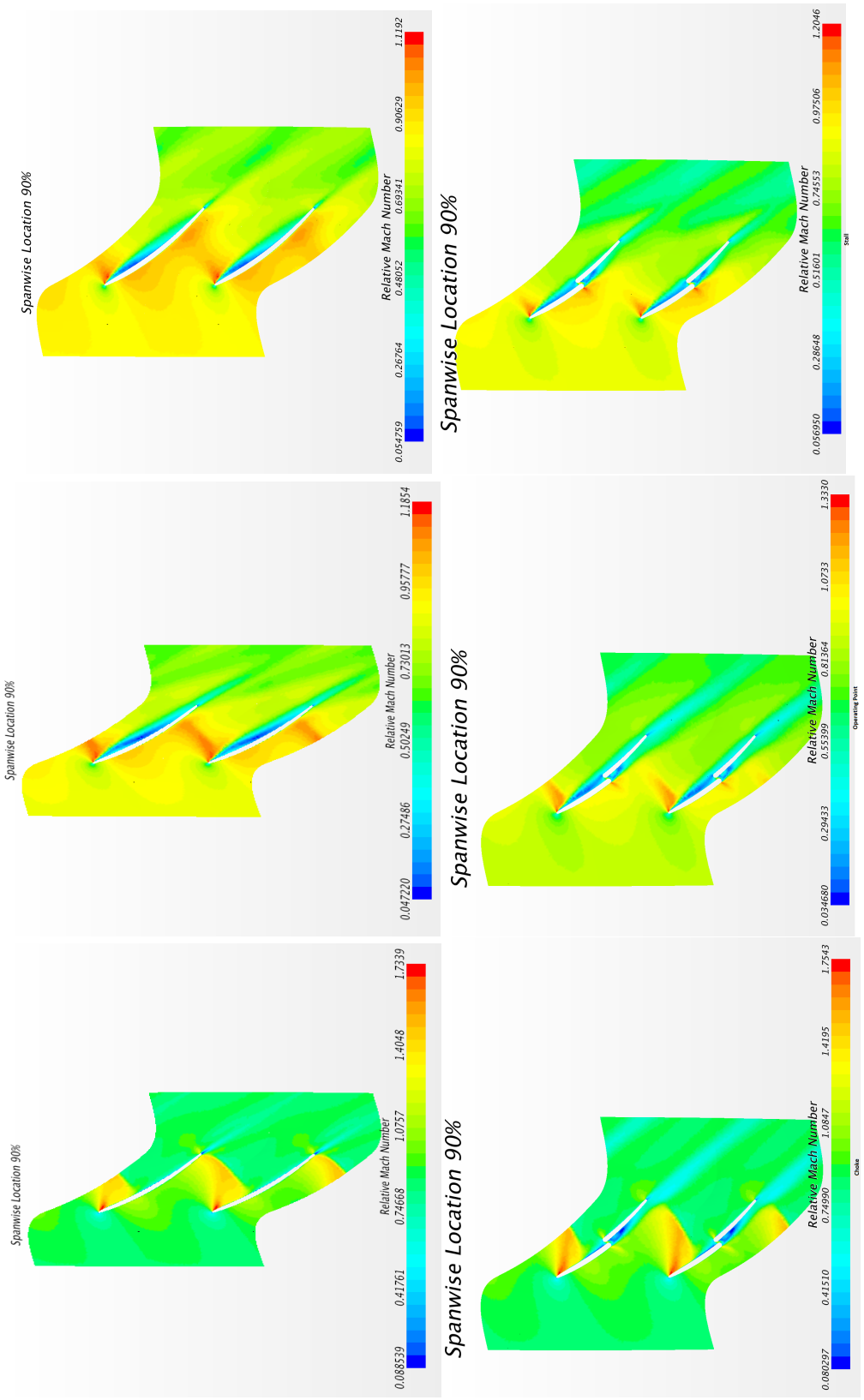

Figure 4.26: Relative mach number contours for 3.75% clearance.

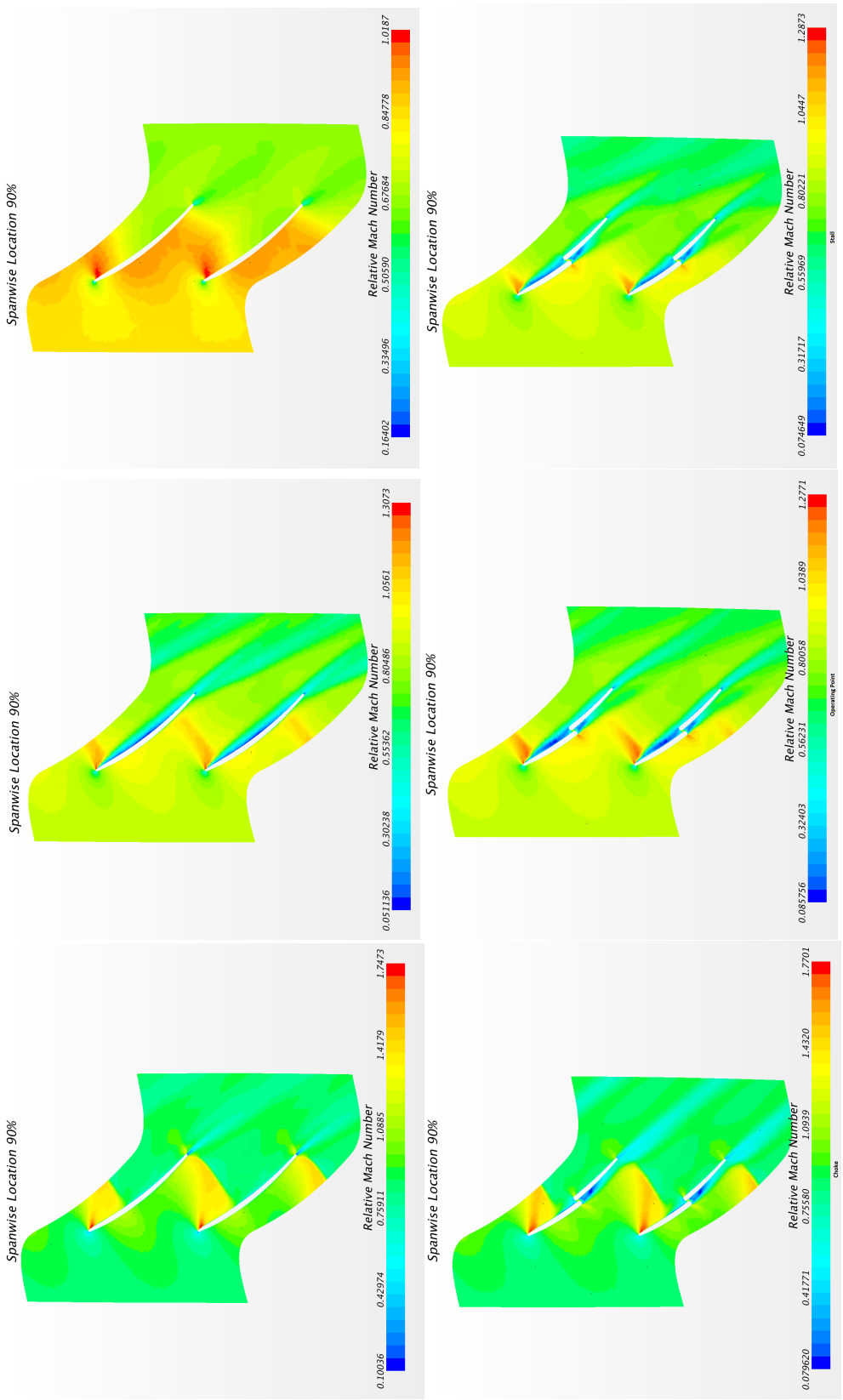

Figure 4.27: Relative mach number contours for 5% clearance.

Figure 4.28 shows the streamtubes of entropy for the baseline case and Figure 4.29 for the split tip case at 3x clearance. It can be seen that in the baseline case the streamtubes follow the curvature of the blade whereas in the split tip case there is a lot more mixing at the beginning and just downstream of the split. It can also be seen the flow has much higher entropy near the split. Hence the split tip can promote mixing to improve stall margin, but can also adversely affect efficiency.

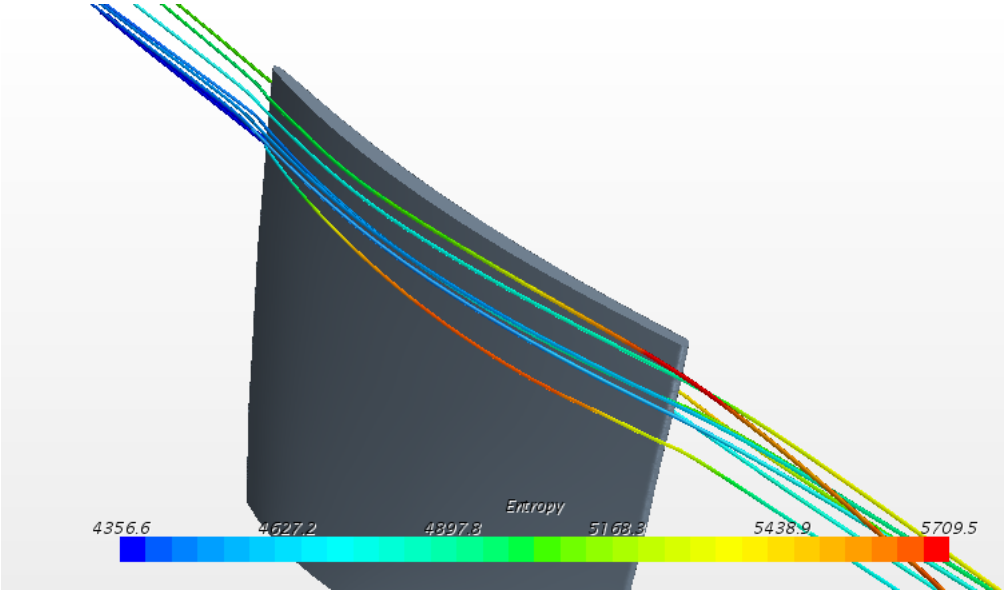

Figure 4.28: Streamtubes of entropy for baseline case at 3x clearance for pb 6.75 atm.

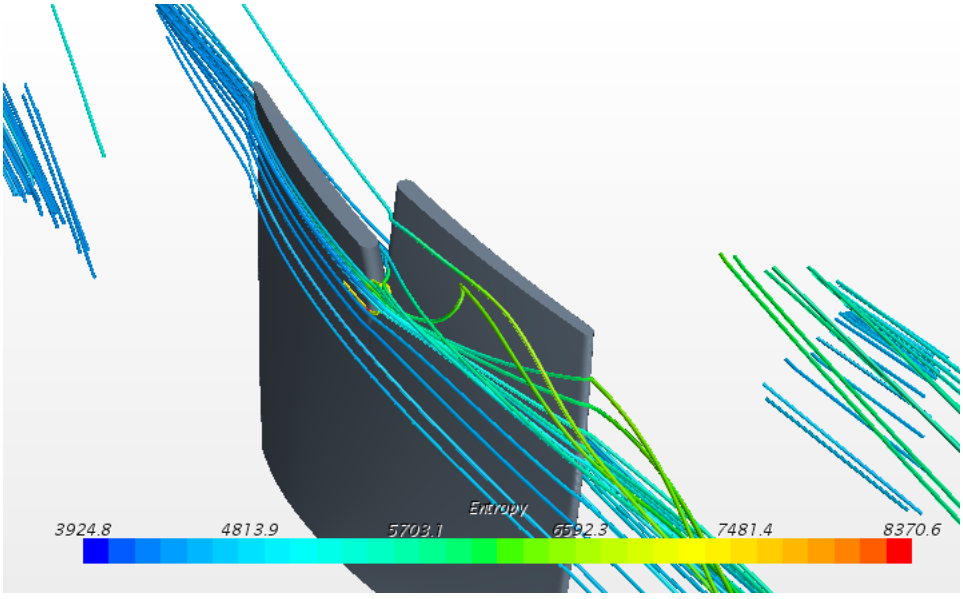

Figure 4.29: Streamtubes of entropy for split tip case at 3x clearance for pb 6.75.

Figure 4.30 shown the flow path of the compressor in the r-z plane and the positions of the inlet, exit, hub, casing, upstream and downstream plotting planes.

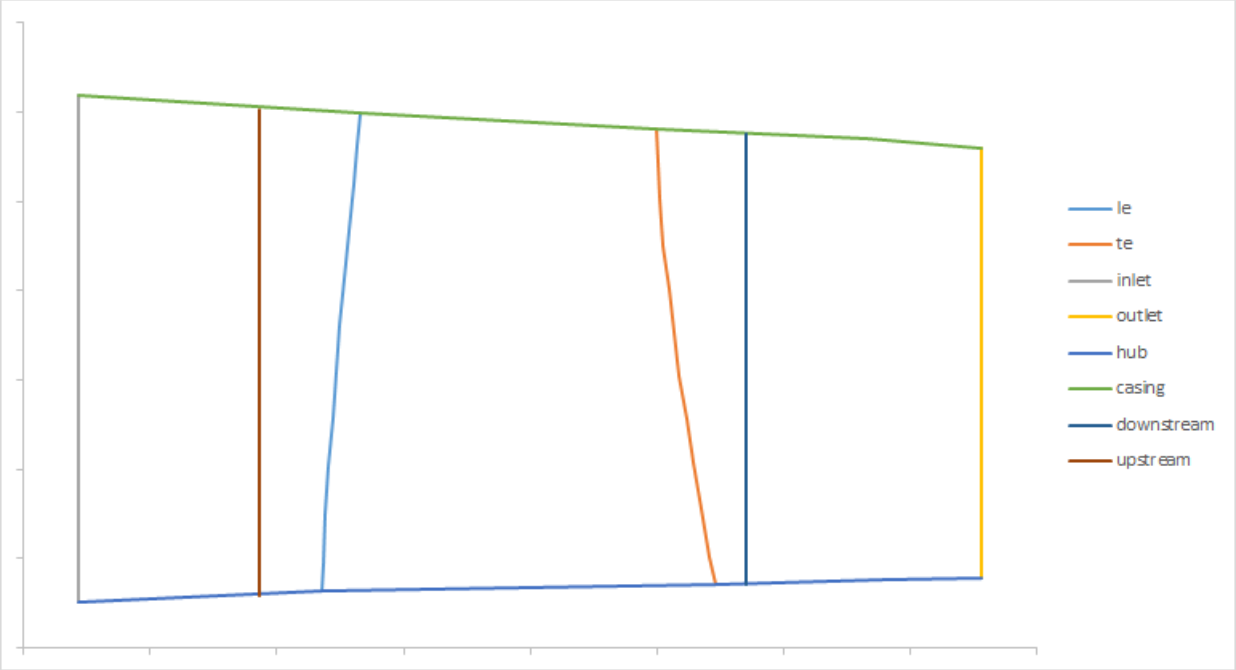

Figure 4.30: Flow Domain.The upstream and downstream planes are at 25% and 75% of the length of the passage respectively. They are used for plotting the Mass Weighted Theta Averaged plots

Mass weighted theta averaged plots for Alpha, Beta, and Relative Mach Number for the 1x clearance case plotted at the downstream plane location, refer Figure 4.30 (75% the length of the passage), are shown in Figures 4.31 to 4.33. Also the plot of beta for the 1x clearance case plotted at the upstream plane location, refer Figure 4.30 (25% of the length of the passage), is shown in Figure 4.34.The Mass weighted theta averaged value is calculated by integrating across the passage, refer Equation 4.4

$$\bar{\psi} = \frac{\int \rho V_z \psi d\theta}{\int \rho V_z d\theta} \tag{4.4}$$

The process of calculating the Mass Weighted Theta Averaged values in Star-CCM+ is explained in Appendix C.

The mass weighted theta averaged total pressure and mass weighted theta averaged total temperature plots at the downstream plane location for all the clearance cases is shown in Figures 4.35 to 4.44. Proflies shown are at similar operating lines, the same back pressure for the same clearance.

Comparing the Total Pressure and Total Temperature for the 1x clearance (Figure 4.37) and 3x clearance (Figure 4.41) case at the downstream plane location, it can be seen that for the 1x clearance case , due to the split tip the depth of the clearance effect is larger than the baseline case. Whereas for the 3x clearance case, the baseline and split tip curves are similar and the effect of the split tip can be seen here. As the performance of the baseline decreases drastically with the increased clearance, the split tip performance is better than the baseline. This is also trure for the 4x case

It can be seen that for the 1x clearance case in Figure 4.38, the split tip case has a slightly higher Total Temperature than the baseline whereas in the 3x clearance case in Figure 4.42, the total temperature curves are similar to each other. Also in the 3x clearance case, looking the the profile for alpha in Figure 4.45 there is a sharp change in alpha near the hub in the split tip curve. This is due the effect of the split tip near the hub. Though the reason for this effect is not known, it shows that the split tip has an effect the the hub

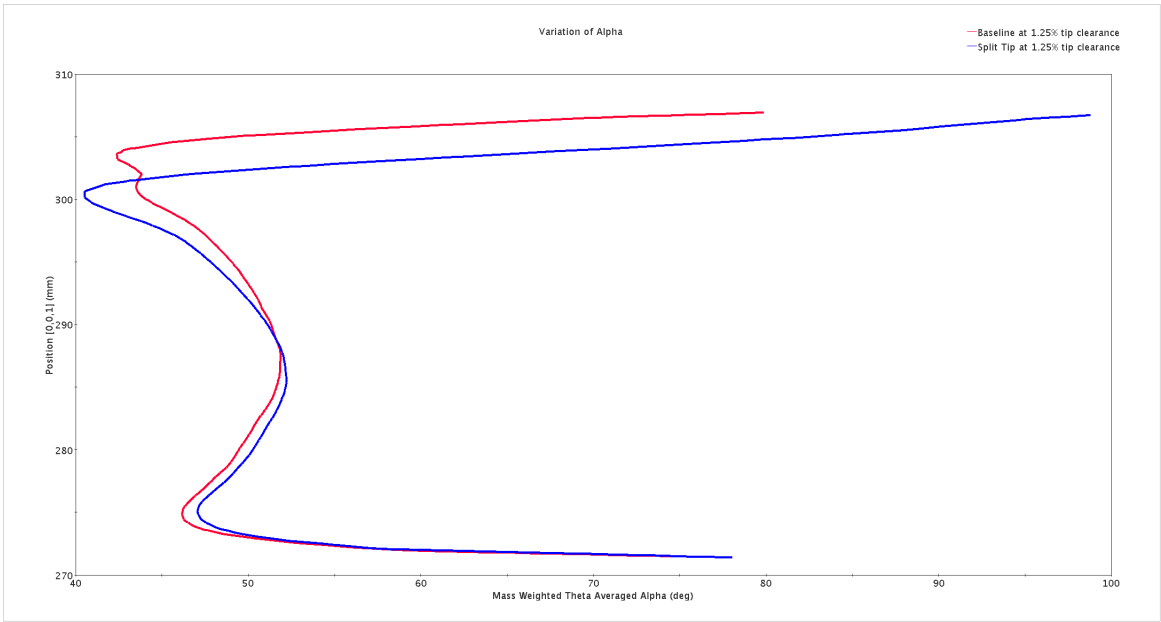

Figure 4.31: Mass Weighted Theta Averaged Alpha at 1x clearance for pb 7.9 atm.

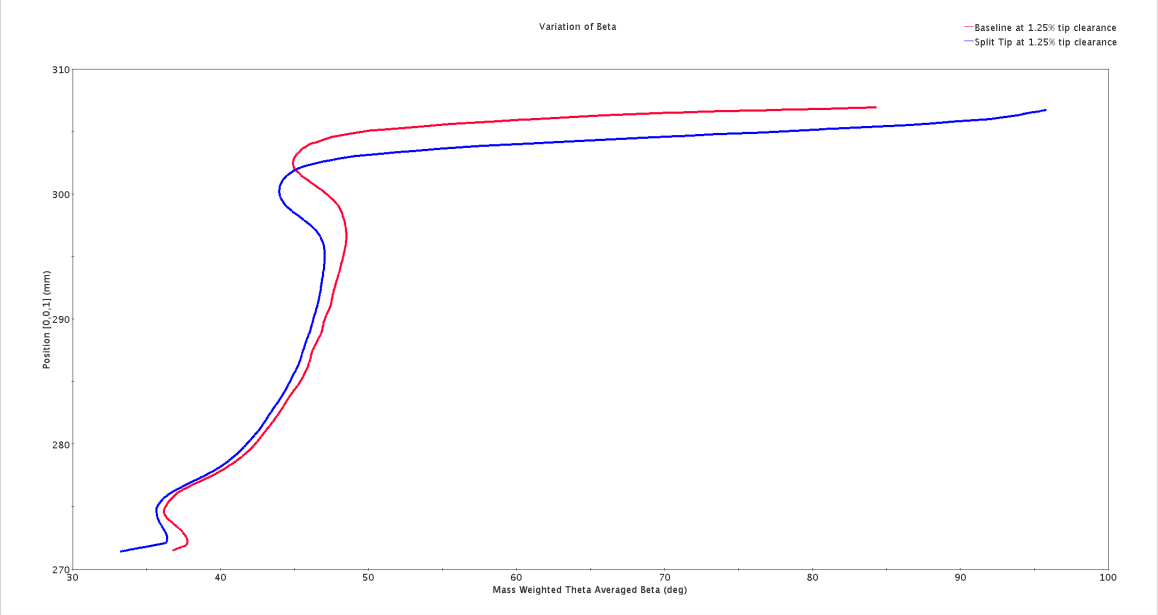

Figure 4.32: Mass Weighted Theta Averaged Beta at 1x clearance for pb 7.9 atm.

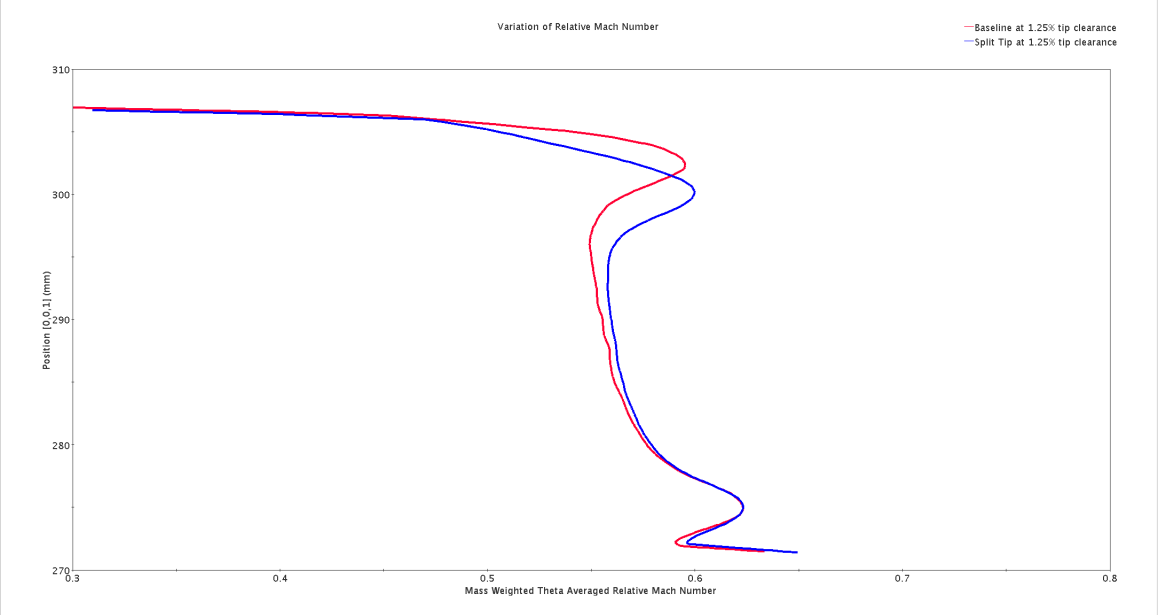

Figure 4.33: Mass Weighted Theta Averaged Relative Mach Number at 1x clearance for pb 7.9 atm.

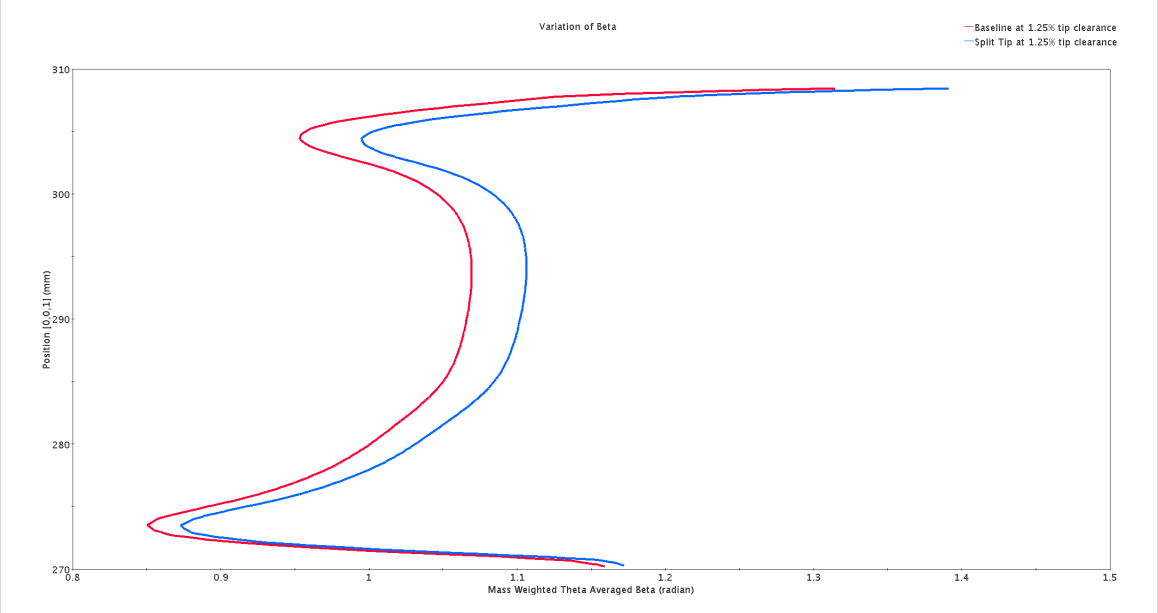

Figure 4.34: Mass Weighted Theta Averaged Beta at Inlet at 1x clearance for pb 7.5 atm.

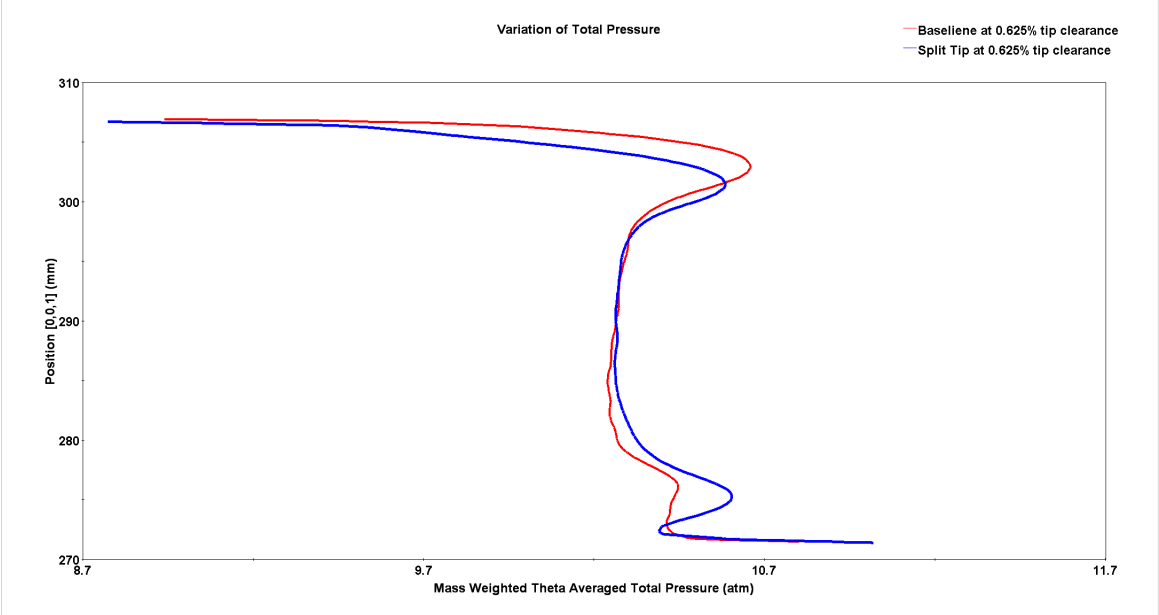

Figure 4.35: Mass Weighted Theta Averaged Total Pressure at 0.5x clearance for pb 8.1 atm.

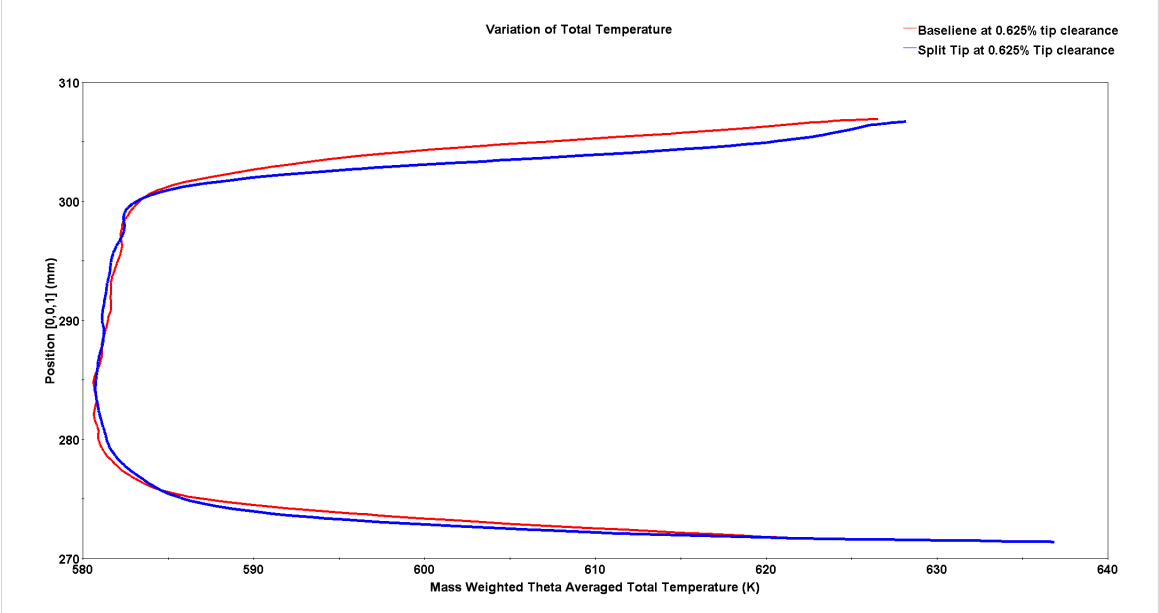

Figure 4.36: Mass Weighted Theta Averaged Total Temperature at 0.5x clearance for pb 8.1 atm

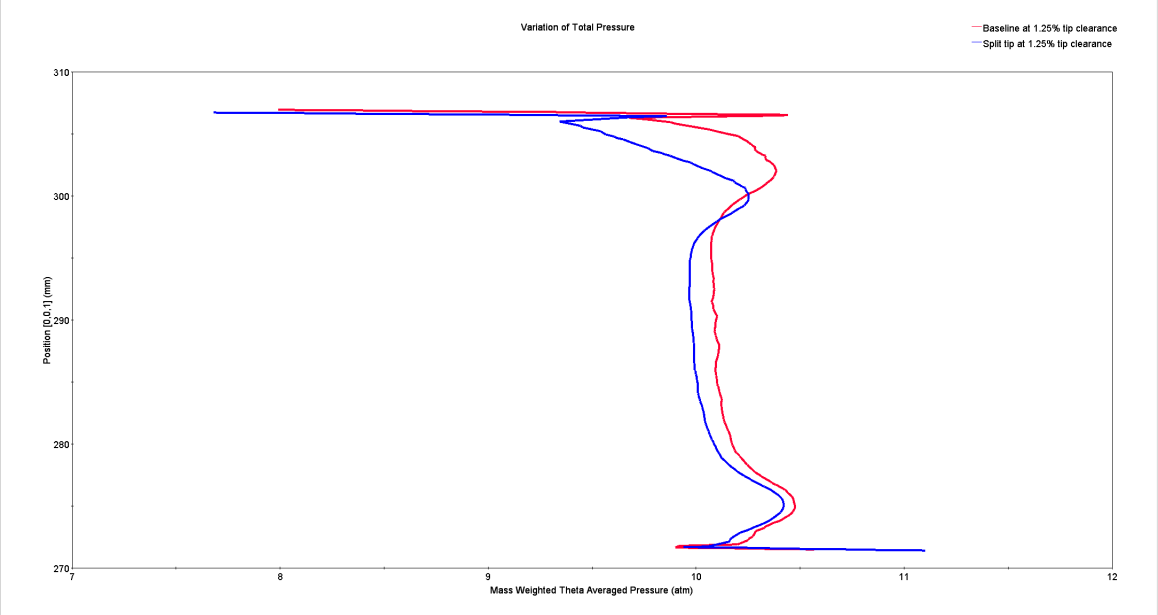

Figure 4.37: Mass Weighted Theta Averaged Total Pressure at 1x clearance for pb 7.9 atm.

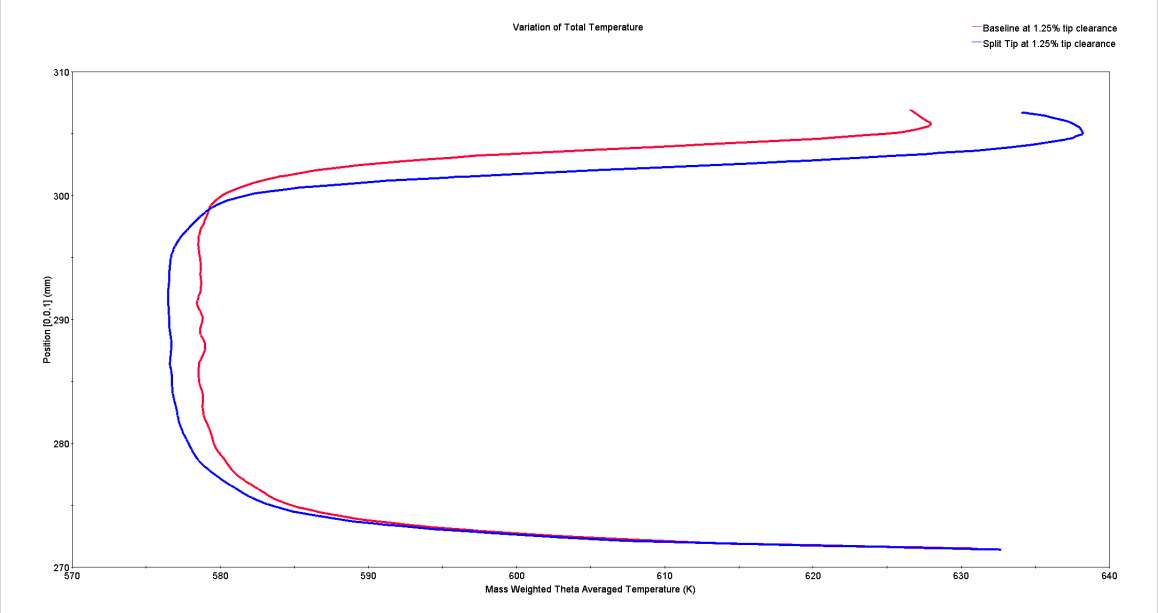

Figure 4.38: Mass Weighted Theta Averaged Total Temperature at 1x clearance for pb 7.9 atm.

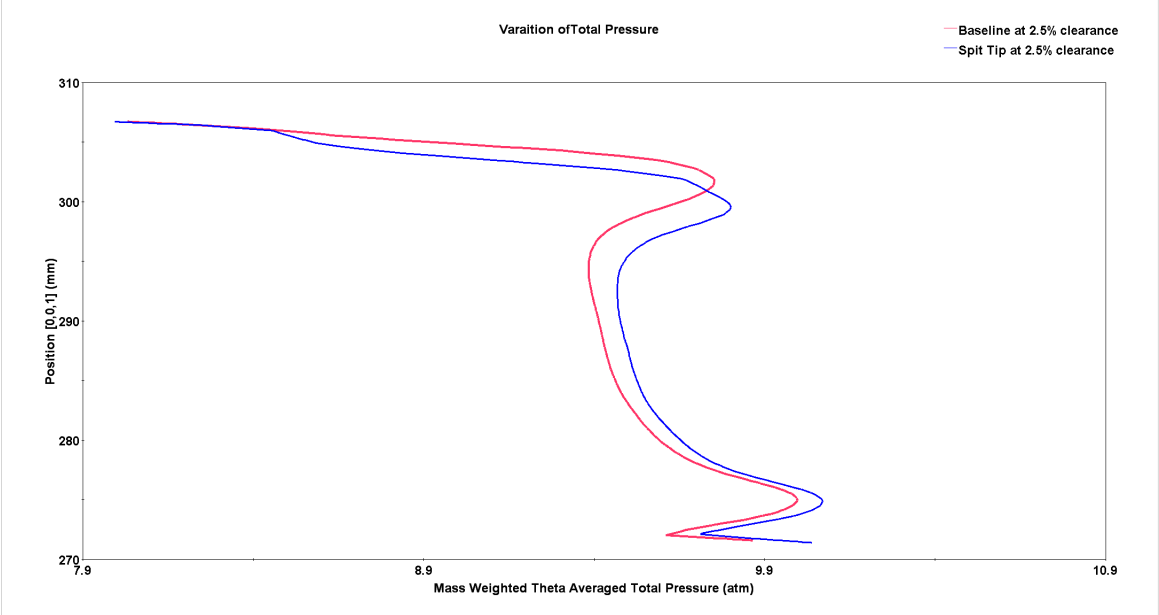

Figure 4.39: Mass Weighted Theta Averaged Total Pressure at 2x clearance for pb 7.5 atm

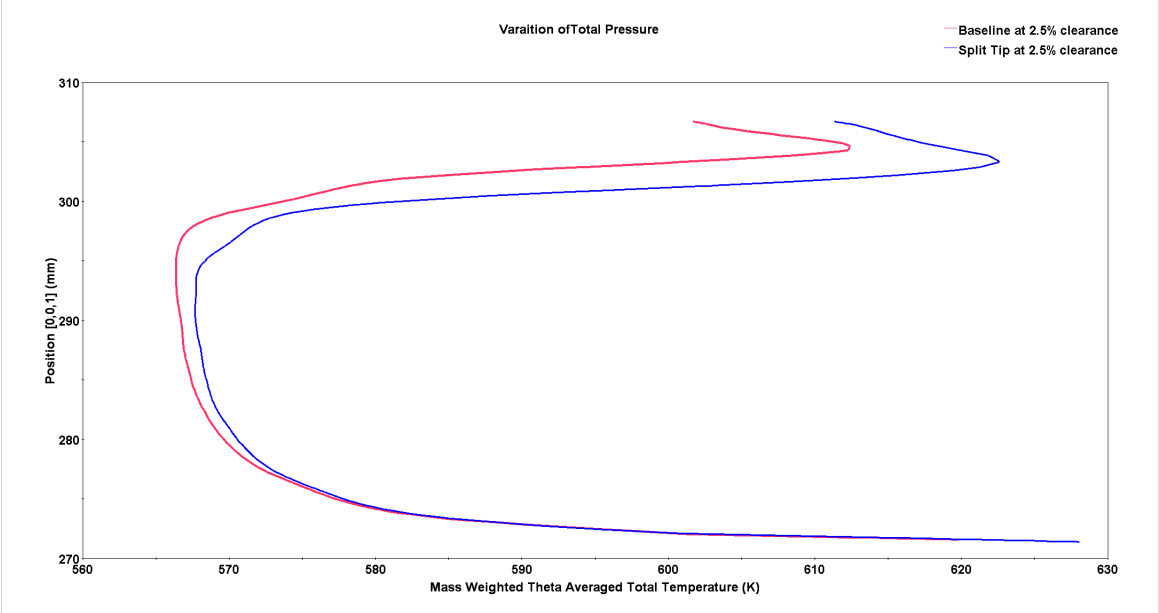

Figure 4.40: Mass Weighted Theta Averaged Total Temperature at 2x clearance for pb 7.5 atm

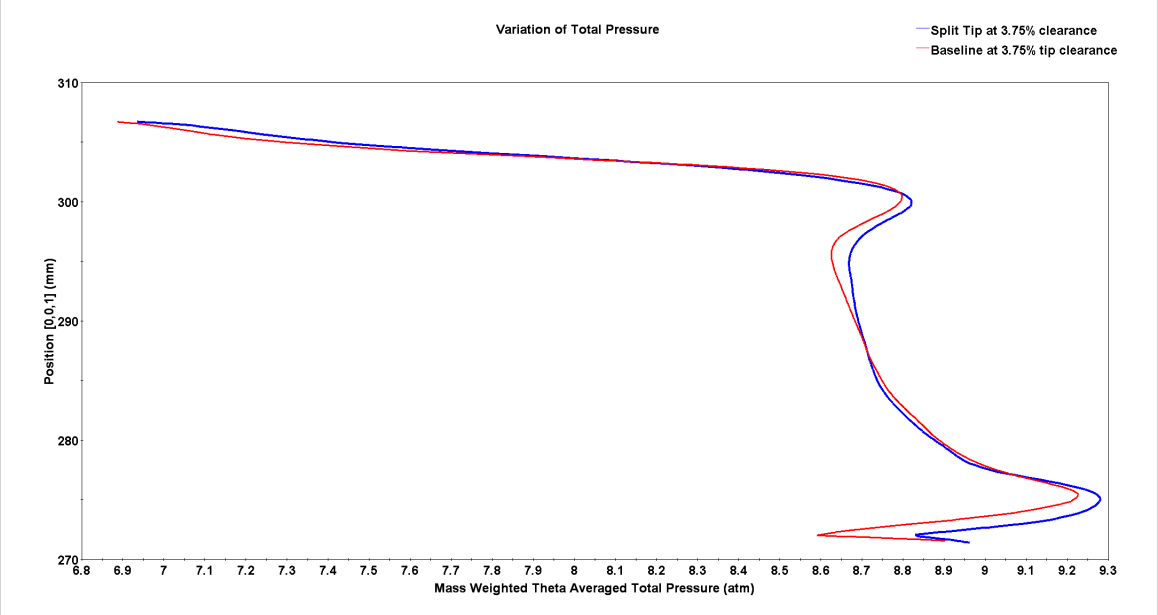

Figure 4.41: Mass Weighted Theta Averaged Total Pressure at 3x clearance for pb 6.75 atm.

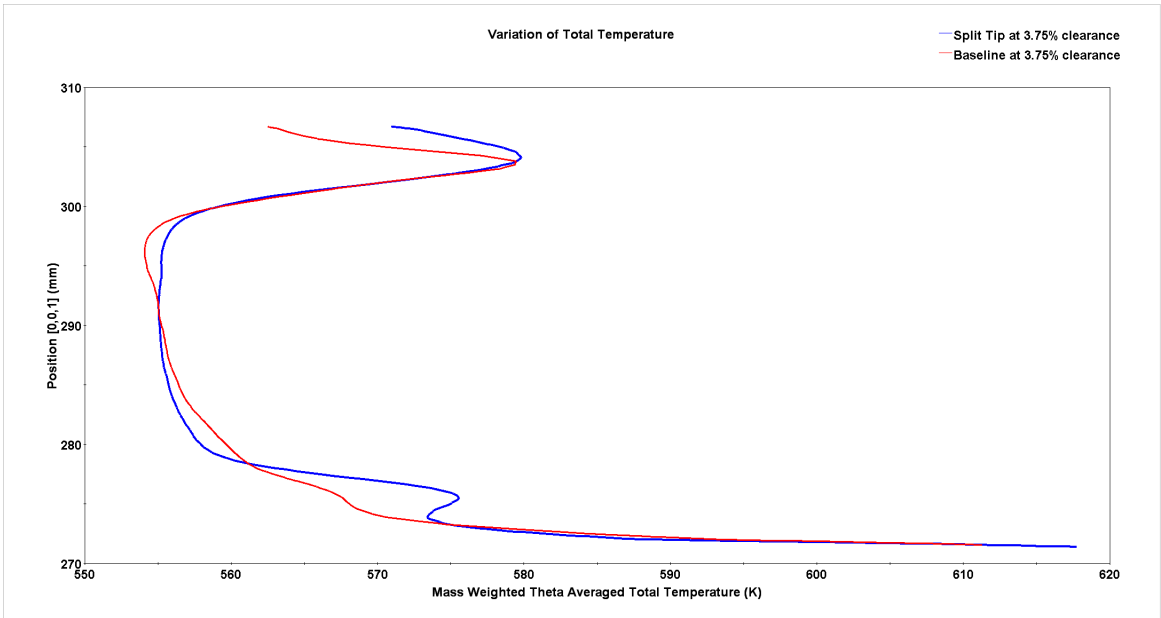

Figure 4.42: Mass Weighted Theta Averaged Total Temperature at 3x clearance for pb 6.75 atm.

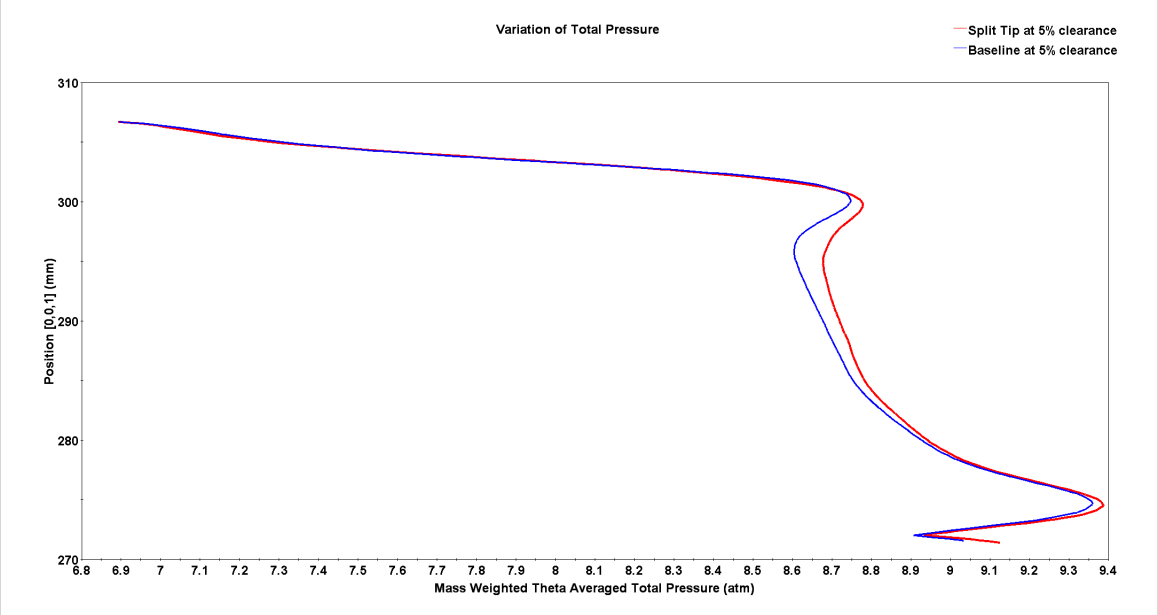

Figure 4.43: Mass Weighted Theta Averaged Total Pressure at 4x clearance for pb 6.5 atm

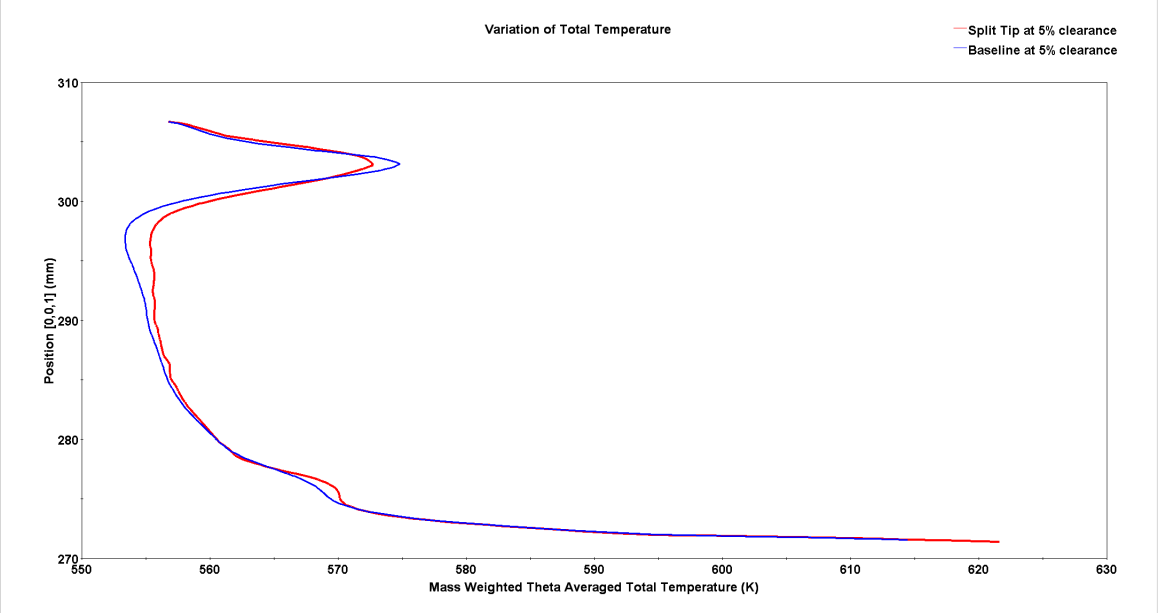

Figure 4.44: Mass Weighted Theta Averaged Total Temperature at 4x clearance for pb 6.5 atm.

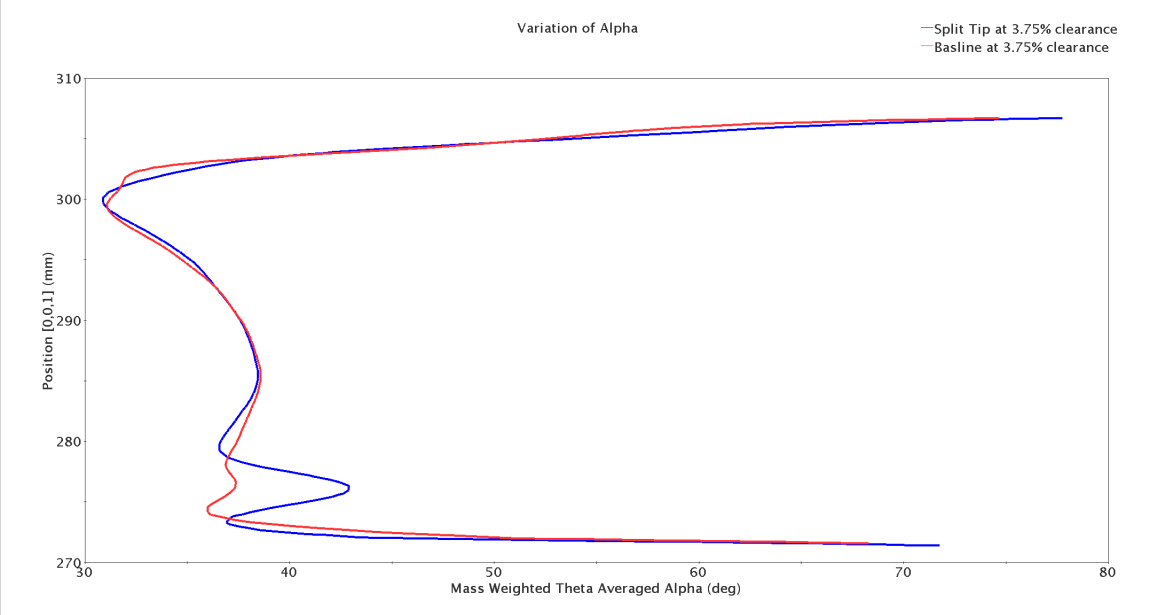

Figure 4.45: Mass Weighted Theta Averaged Alpha at 3x clearance for pb 6.75 atm.

4.2 Structural Analysis

A structural analysis has been done to to check the structural integrity of the design. A geometry with a periodic disc is created, Figure 4.46.

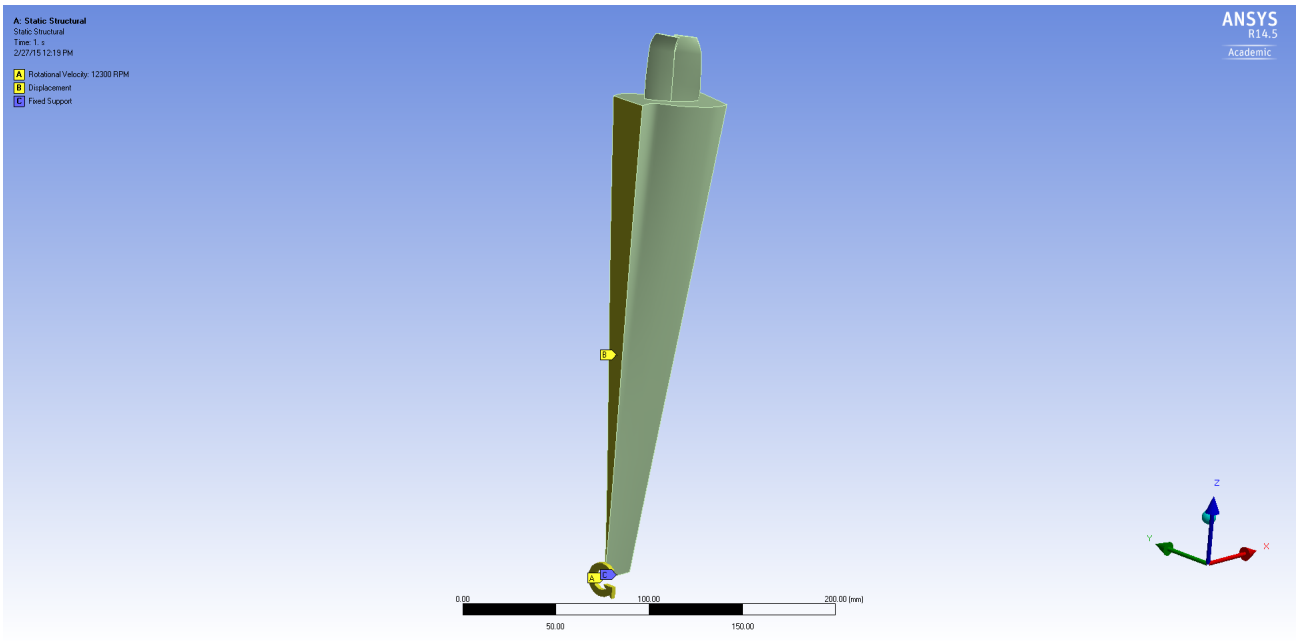

Figure 4.46: Ansys Geometry.

A unstructured mesh is created using the automatic mesh generators in Ansys, Figure

4.47. Inconel 718 is used as the material for the blade. The Young's Modulus and Poisson's ratio for Inconel 718 was input into ANSYS at different temperatures [?]. Table 4.3 lists the Young's Modulus and Poisson's ratio at different temperatures.

Temperature (K)	Young's Modulus (GPa)	Poisson's Ratio
294	199.95	0.294
311	198.56	0.291
366	195.81	0.288
422	193.05	0.280
478	190.29	0.280
533	186.85	0.275
589	184.09	0.272
644	180.64	0.273

Table 4.3: Inconel 718 data.

Three boundary conditions were used in the analysis.

- A rotational velocity along the z axis at 12300 rpm
- A fixed support at the hub
- Fixed displacement in the axial direction

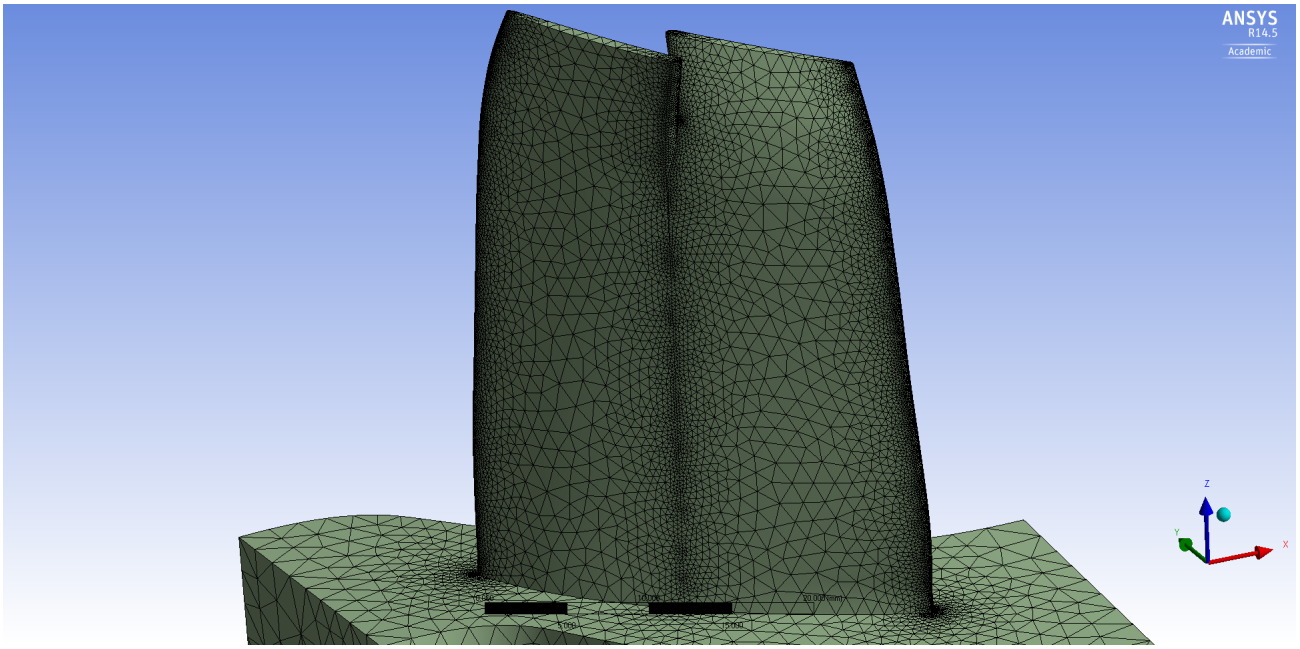

Figure 4.47: ANSYS Mesh.

The analysis is performed at 550K. The results of the analysis is given below. Figures 4.48, 4.49 and 4.50 show the Equivalent (Von Mises) stress. As expected the max stress

was near the split. The max stress had a value of 1353 MPa which exceeded the tensile strength of the material which is 1100 MPa.

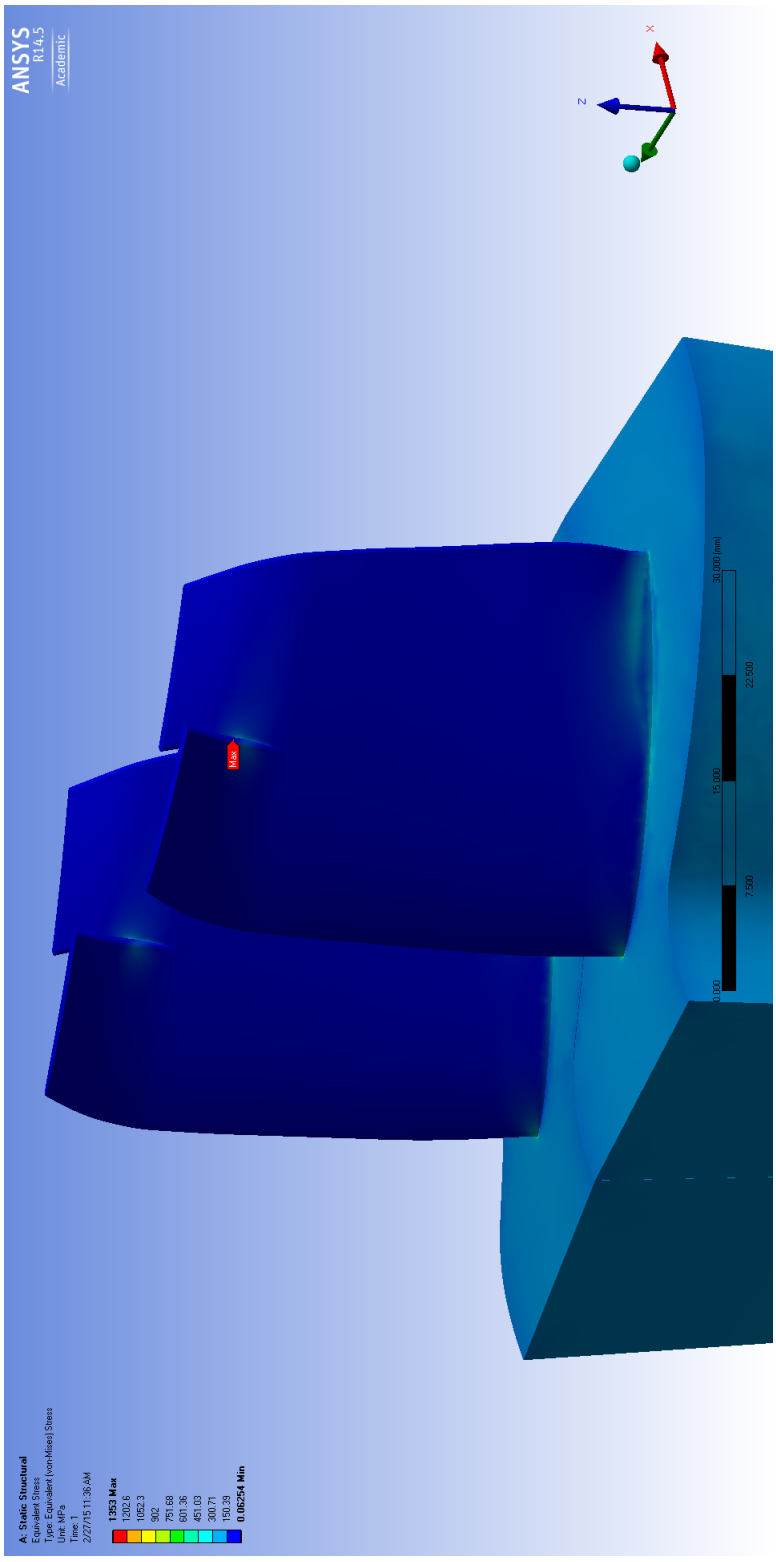

Figure 4.48: Equivalent Stress on Suction Side of the Blade.

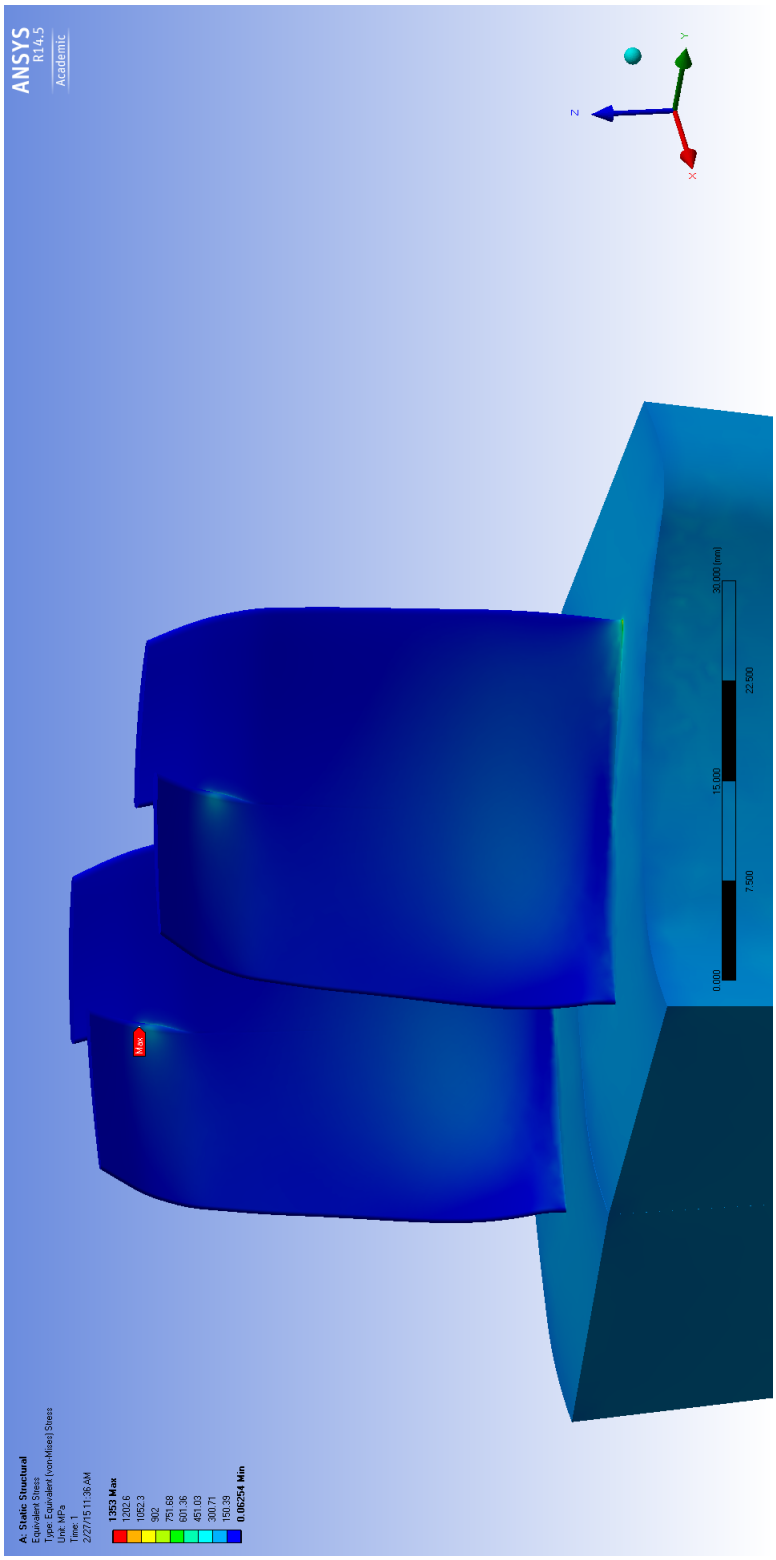

Figure 4.49: Equivalent Stress on Pressure Side of the Blade.

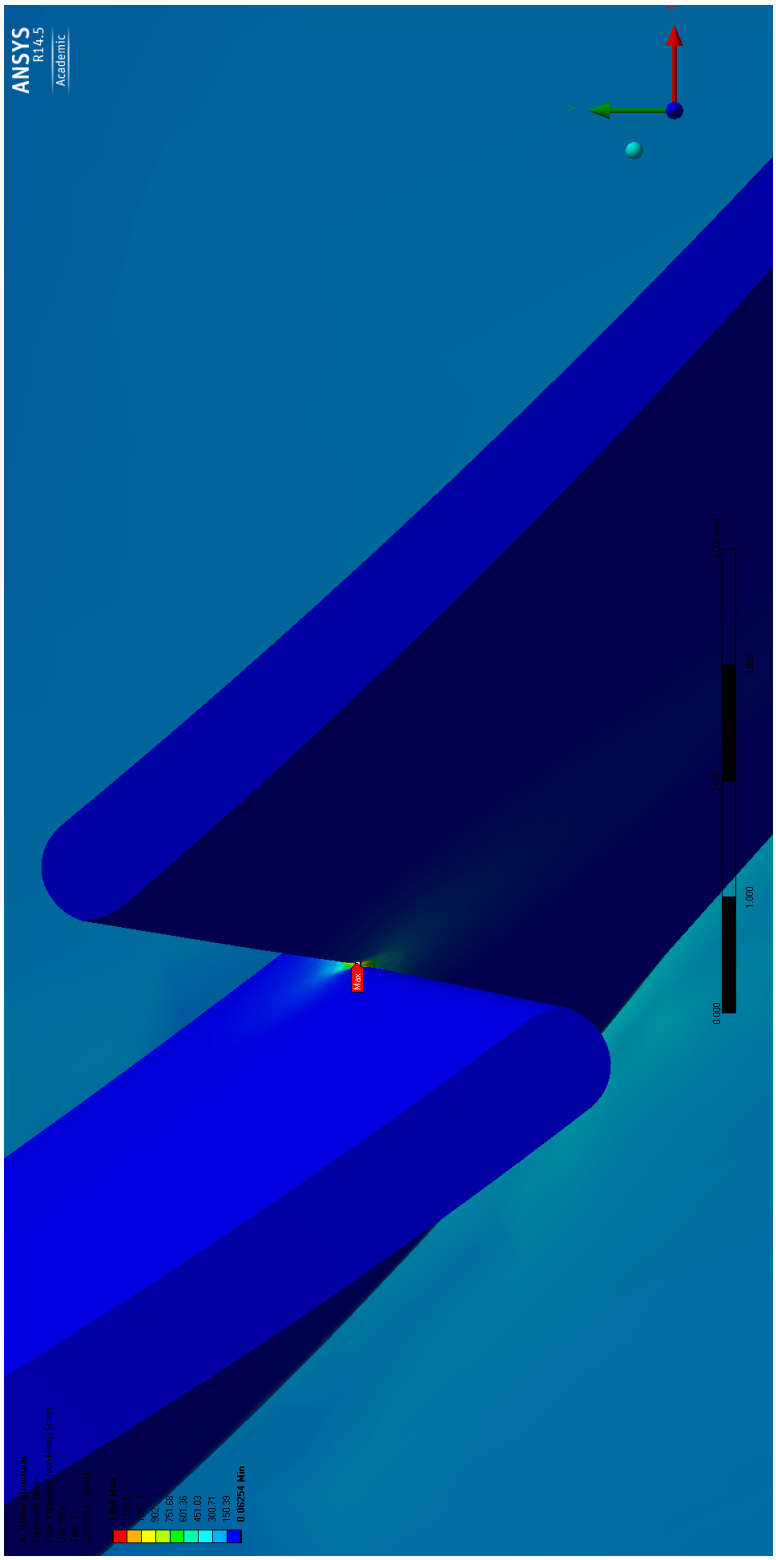

Figure 4.50: Equivalent Stress.

Chapter 5

Conclusion and Future Work

5.0.1 Conclusions

A novel split tip blade geometry has been generated and CFD analysis has been performed. The design was implemented on the sixth rotor of a high pressure compressor based on the EEE HPC design by GE. Five different tip clearance cases were run at different back pressures. Structural analysis was performed to check the structural integrity of the design.

The itemized conclusions are as follows

- A novel blade design has been generated.
- The new geometry has a higher overall operating range than the baseline blade.
- The split tip blade had a higher pressure ratio and efficiency than the baseline blade near choke but falls off near stall.
- The split tip blade performs better at higher tip gap/blade height ratio than the baseline blade.
- The structural analysis showed that the design would fail in the current configration, but approaches to mitigate the high stresses are possible.
- The split tip impacts a larger portion of the span near the casing than the baseline at tight clearances, but not at large clearances

5.0.2 Future Work

Future improvements for continued research on this topic are listed as follows:

- Further understanding of the flow physics.
- Generalizing the geometry by performing optimization on the lean and depth of cut and axial location.
- Improving the leading edges at the split tip to represent a more elliptical leading and trailing edges than the circular one used here.

- Studying the effect of multiple splits on the geometry.
- Improving the geometry near the split by adding fillets and more material to reduce the stress concentration

Bibliography

[1] Brossman, J. R., 2012. "An investigation of rotor tip leakage flows in the rear-block of a multistage compressor". PhD thesis, Purdue University.

[2] Softeis, 2006. Haliaeetus leucocephalus.

[3] Storer, J. A., and Cumpsty, N. A., 1994. "An approximate analysis and prediction method for tip clearance loss in axial compressors". *Journal of Turbomachinery,* **116**(4), Oct., pp. 648–656.

[4] Wisler, D. C., 1985. "Loss reduction in axial-flow compressors through low-speed model testing". *Journal of Engineering for Gas Turbines and Power,* **107**(2), Apr., pp. 354–363.

[5] Smith, G. D. J., and Cumpsty, N. A., 1984. "Flow phenomena in compressor casing treatment". *Journal of Engineering for Gas Turbines and Power,* **106**(3), July, pp. 532–541.

[6] Wennerstrom, A. J., 1984. "Experimental study of a high-throughflow transonic axial compressor stage". *Journal of Engineering for Gas Turbines and Power,* **106**(3), July, pp. 552–560.

[7] Bruna., D., and Turner., M., 2013. "A rothalpy analysis for the isothermal boundary condition at casing applied to the rotor 37 transonic axial flow compressor". No. GT2013-94595, ASME Turbo Expo 2013.

[8] Gannon, A. J., Hobson, G. V., Turner, M. G., and Sanz, W. "Performance of a splittered transonic rotor with several tip clearances". No. GT2015-453799, ASME Turbo Expo 2015.

[9] Siddappaji, K., and Turner, M., 2012. "General capability of parametric 3d blade design tool for turbomachinery". No. GT2012-69756, ASME Turbo Expo 2012.

[10] Nemnem, A. F., Turner, M. G., Siddappaji, K., and Galbraith, M., 2014. "A smooth curvature-defined meanline section option for a general turbomachinery geometry generator". No. GT2014-26363, ASME Turbo Expo 2014.

[11] Ahmed, M., F. N., 2014. "A general multidisciplinary turbomachinery design optimization system applied to a transonic fan". PhD thesis, University of Cincinnati.

[12] Siddappaji, K., 2011. "Parametric 3d blade geometry modeling tool for turbomachinery systems". Master's thesis, University of Cincinnati.

[13] www.gtsl.ase.uc.edu/3DBGB, 2014.

[14] CD-Adapco. Star-ccm+. http://www.cd-adapco.com/products/star-ccm

[15] ANSYS, I., 2015. Ansys.

[16] Shabbir, A., and Adamczyk, J. J., 2004. "Flow mechanism for stall margin improvement due to circumferential casing grooves on axial compressors". *Journal of Turbomachinery,* **127**(4), Mar., pp. 708–717.

[17] Denton, J., D., 2001. "The effects of lean and sweep on transonic fan performance:a computational study". Vol. 5, ASME Turbo Expo 2002:Power of Land Sea and Air, pp. 23–32.

[18] Cline, S., J., Fesler, W., Liu, H., S., Lovell, R., C., and Shaffer, S., J., 1985. High pressure compressor component performance report. Tech. Rep. NASA CR-168245, GE-NASA.

[19] CD-Adapco. Starccm+ user guide.

[20] Mattingly, J. D., 2006. *Elements of Gas Turbine Propulsion.* American Institute of Aeronautics and Astornautics.

[21] Power, B. Personal correspondance.

[22] Cumpsty, N. A., 2010. "Some lessons learned". *Journal of Turbomachinery,* **132**(4), May, pp. 041018–041018.

Appendix A

3DBGB Input Files

Input parameters (version 1.1)
e3c
Blade row #:
12
Number of blades in this row:
80
Blade Scaling factor (mm):
350.700000000000
Number of streamlines:
21
Angles in the input file (0=Beta_z (default),1=Beta_r):
0
Airfoil camber defined by curvature control (0=no,1=yes):
0
Airfoil Thickness distribution (0=Wennerstrom,1=Spline):
0
Airfoil Thickness multiplier (0=no,1=yes):
0
Airfoil LE defined by spline (0=no,1=yes):
0
Non-dimensional Actual chord (0=no,1=yes,2=spline):
0
Sectionwise properties:
J in_Beta out_Beta mrel_in chord t/c_max Incidence Deviation Sec. Flow Angle
1 -54.47338791 -28.21655510 0.79255895 0.08038719 0.07972391 0.00000000 0.00000000 0.00000000
2 -54.84393396 -29.69306633 0.78856519 0.07908441 0.07827014 0.00000000 0.00000000 0.00000000
3 -55.21867168 -31.05324153 0.77968914 0.07802034 0.07672903 0.00000000 0.00000000 0.00000000
4 -55.59502058 -32.47266350 0.76729720 0.07692415 0.07500573 0.00000000 0.00000000 0.00000000

5 -55.96917514 -33.83941274 0.75323011 0.07578337 0.07318849 0.00000000 0.00000000 0.00000000
6 -56.33643057 -35.14521105 0.74745883 0.07452650 0.07127287 0.00000000 0.00000000 0.00000000
7 -56.69789927 -36.36870637 0.74387642 0.07313288 0.06928824 0.00000000 0.00000000 0.00000000
8 -57.05490052 -37.47717218 0.74192983 0.07163062 0.06727496 0.00000000 0.00000000 0.00000000
9 -57.41209777 -38.46223841 0.73993707 0.07006679 0.06524981 0.00000000 0.00000000 0.00000000
10 -57.76551466 -39.35237929 0.73981042 0.06848035 0.06314126 0.00000000 0.00000000 0.00000000
11 -58.12551670 -40.17993030 0.74352924 0.06690615 0.06092231 0.00000000 0.00000000 0.00000000
12 -58.51153293 -40.91788731 0.75016005 0.06537982 0.05869019 0.00000000 0.00000000 0.00000000
13 -58.93295034 -41.55635444 0.75799364 0.06392014 0.05645899 0.00000000 0.00000000 0.00000000
14 -59.38094646 -42.11300590 0.76666738 0.06248417 0.05405318 0.00000000 0.00000000 0.00000000
15 -59.85630630 -42.51275278 0.77742465 0.06106640 0.05157168 0.00000000 0.00000000 0.00000000
16 -60.36070398 -42.79563292 0.79147211 0.05954710 0.04894448 0.00000000 0.00000000 0.00000000
17 -60.90306993 -42.90001766 0.80670743 0.05804244 0.04629060 0.00000000 0.00000000 0.00000000
18 -61.48271496 -42.73762469 0.83079259 0.05671187 0.04372461 0.00000000 0.00000000 0.00000000
19 -62.07332021 -42.29224217 0.86539487 0.05557593 0.04119909 0.00000000 0.00000000 0.00000000
20 -62.67468021 -41.54918167 0.92876102 0.05455518 0.03863126 0.00000000 0.00000000 0.00000000
21 -63.30208348 -40.60131662 1.01571935 0.05333042 0.03583723 0.00000000 0.00000000 0.00000000
LE / TE curve (x,r) definition :
Number of Curve points :
12
xLE rLE xTE rTE
1.40711200 0.77265200 1.46925500 0.77402800
1.40733000 0.77866300 1.46838600 0.78025600
1.40769200 0.78996200 1.46708200 0.79119300
1.40812600 0.80075300 1.46577800 0.80126000
1.40877800 0.81140000 1.46461900 0.81103800
1.40935800 0.82190200 1.46353300 0.82081600
1.40993700 0.83240400 1.46266400 0.83052100

1.41052200 0.84283300 1.46186700 0.84029800
1.41131300 0.85340800 1.46107000 0.85007600
1.41211000 0.86412700 1.46049100 0.86028800
1.41268900 0.87245600 1.46020100 0.86854500
1.41326900 0.87962600 1.45998400 0.87629500
Airfoil type and Variable Radial Stacking information.
stack_u: % chord stack (0.00 to 100.00).
stack_v: % below or above meanline stack (-100.00 to +100.00).
Use +200 for stacking on airfoil area centroid.
Variable Radial stacking (0=no,1=yes):
0
J type |stk_u |stk_v |umxthk |lethk |tethk |Jcells(Grid:4n+1) |eta_ofst(<=10){%thkc/Jmax} |BGgrid(0=no,1=yes) |
1 sect1 25.00 0.00 0.30 0.02 0.02 33 10 1
2 sect1 25.00 0.00 0.30 0.02 0.02 33 10 1
3 sect1 25.00 0.00 0.30 0.02 0.02 33 10 1
4 sect1 25.00 0.00 0.30 0.02 0.02 33 10 1
5 sect1 25.00 0.00 0.30 0.02 0.02 33 10 1
6 sect1 25.00 0.00 0.30 0.02 0.02 33 10 1
7 sect1 25.00 0.00 0.30 0.02 0.02 33 10 1
8 sect1 25.00 0.00 0.30 0.02 0.02 33 10 1
9 sect1 25.00 0.00 0.30 0.02 0.02 33 10 1
10 sect1 25.00 0.00 0.30 0.02 0.02 33 10 1
11 sect1 25.00 0.00 0.30 0.02 0.02 33 10 1
12 sect1 25.00 0.00 0.30 0.02 0.02 33 10 1
13 sect1 25.00 0.00 0.30 0.02 0.02 33 10 1
14 sect1 25.00 0.00 0.30 0.02 0.02 33 10 1
15 sect1 25.00 0.00 0.30 0.02 0.02 33 10 1
16 sect1 25.00 0.00 0.30 0.02 0.02 33 10 1
17 sect1 25.00 0.00 0.30 0.02 0.02 33 10 1
18 sect1 25.00 0.00 0.30 0.02 0.02 33 10 1
19 sect1 25.00 0.00 0.30 0.02 0.02 33 10 1
20 sect1 25.00 0.00 0.30 0.02 0.02 33 10 1
21 sect1 25.00 0.00 0.30 0.02 0.02 33 10 1
Control table for blending section variable:
5 0 0
span bf1 bf2
0.000000000000000E+000 1 0
0.250000000000000 1 0
0.500000000000000 1 0
0.750000000000000 1 0
1.00000000000000 1 0
Stacking axis location (200=centroid):
25000
Control points for delta_m:

5 0
span delta_m True_sweep
0.000000000000000E+000 0.000000000000000E+000 0.0
0.250000000000000 0.000000000000000E+000 0.0
0.500000000000000 0.000000000000000E+000 0.0
0.750000000000000 0.000000000000000E+000 0.0
1.00000000000000 0.000000000000000E+000 0.0
Control points for delta_theta:
8 1
span delta_theta True_lean
0.000000000000000E+000 0.000000000000000E+000 0.0
0.250000000000000 0.000000000000000E+000 0.0
0.500000000000000 0.000000000000000E+000 0.0
0.750000000000000 0.000000000000000E+000 0.0
0.800000000000000 -0.00000000000000E+000 0.0
0.900000000000000 -0.004000000000000E+000 -0.0016
0.950000000000000 -0.008000000000000E+00 -0.0033
1.00000000000000 -0.012000000000000E+000 -0.0050
Control points for in_beta*:
5
span in_beta*
0.000000000000000E+000 0.000000000000000E+000
0.250000000000000 0.000000000000000E+000
0.500000000000000 0.000000000000000E+000
0.750000000000000 0.000000000000000E+000
1.00000000000000 0.000000000000000E+000
Control points for out_beta*:
5
span out_beta*
0.000000000000000E+000 0.000000000000000E+000
0.250000000000000 0.000000000000000E+000
0.500000000000000 0.000000000000000E+000
0.750000000000000 0.000000000000000E+000
1.00000000000000 0.000000000000000E+000
Control points for chord:
5
span chord
0.000000000000000E+000 0.000000000000000E+000
0.250000000000000 0.000000000000000E+000
0.500000000000000 0.000000000000000E+000
0.750000000000000 0.000000000000000E+000
1.00000000000000 0.000000000000000E+000
Control points for tm/c:
5
span tm/c

0.000000000000000E+000 0.000000000000000E+000
0.250000000000000 0.000000000000000E+000
0.500000000000000 0.000000000000000E+000
0.750000000000000 0.000000000000000E+000
1.00000000000000 0.000000000000000E+000
Hub offset
0.000000000000000E+000
Tip offset
0.000000000000000E+000
Streamline Data
x_s r_s
-0.300000000000000 0.494387000000000
-0.200000000000000 0.494387000000000
-0.186572000000000 0.494387000000000
-7.025421900000001E-002 0.492938365000000
0.000000000000000E+000 0.507423771000000
0.263851669000000 0.580068081000000
0.293891489000000 0.588552850000000
0.398736643000000 0.618549342000000
0.440935757000000 0.630187586000000
0.603606866000000 0.673643804000000
0.636633592000000 0.681538350000000
0.714130514000000 0.699645108000000
0.752227131000000 0.707322373000000
0.866009995000000 0.727239806000000
0.897443326000000 0.732309698000000
0.961034258000000 0.742232201000000
0.995364670000000 0.746288115000000
1.08676758200000 0.754834504000000
1.11573839400000 0.757804012000000
1.17063808200000 0.763453321000000
1.20207141300000 0.765336424000000
1.27906134600000 0.767581661000000
1.30390381700000 0.768595640000000
1.35402332200000 0.770768451000000
1.40711233400000 0.772651554000000
1.46925472600000 0.774027667000000
1.49554573800000 0.775041646000000
1.54363728500000 0.777069602000000
1.57651915700000 0.778083581000000
1.63902368400000 0.779242413000000
1.66574925800000 0.779169986000000
1.71876584300000 0.778952705000000
1.77323097000000 0.779097559000000
1.83138987500000 0.780401246000000

1.85348011900000 0.780328819000000
1.91200115900000 0.779966684000000
1.93785760800000 0.780111538000000
1.99043963200000 0.780618527000000
2.01318171900000 0.780546100000000
2.06569131600000 0.780111538000000
2.09386543100000 0.780183965000000
2.13935000000000 0.780619000000000
2.16810313600000 0.780473673000000
2.23002824700000 0.780039111000000
2.30000000000000 0.780000000000000
2.50000000000000 0.780000000000000
0 0
1.38223421793494 0.776089231747206
1.39302575258406 0.776427586371302
1.40381853447651 0.776743276534340
1.41461277158334 0.777046875718339
1.42540828507959 0.777368510346849
1.43620442198022 0.777720663126003
1.44700036940181 0.778065914779841
1.45779533661827 0.778371782442426
1.46858873318392 0.778642576837112
1.47938043909526 0.778935482437679
1.49017087126078 0.779284425194044
1.50096038090340 0.779693978576179
1.51174933466604 0.780096369593644
0 0
1.38259808552201 0.778988542253906
1.39338412717120 0.779304700598530
1.40417135697879 0.779605999781926
1.41495995186279 0.779903720115986
1.42574978861637 0.780212427149267
1.43654031186873 0.780532052551585
1.44733077858880 0.780832365329987
1.45812045936375 0.781091217773241
1.46890884139311 0.781321079900359
1.47969588331934 0.781582958645588
1.49048191349550 0.781908186194946
1.50126717264268 0.782295732564068
0 0
1.38297757191222 0.782222579140842
1.39375789698175 0.782511501806866
1.40453936320229 0.782794924188213
1.41532213881355 0.783081995351970
1.42610614876825 0.783371894475145

1.43689091657930 0.783651547787885
1.44767576349840 0.783896564679087
1.45846001790102 0.784096392656085
1.46924323121907 0.784275785982663
1.48002541096159 0.784499917542491
1.49080682028723 0.784797514394142
1.50158760800746 0.785151037327541
0 0
1.38337236102054 0.785882593139950
1.39414675045853 0.786136414598445
1.40492225006256 0.786395539603582
1.41569903482055 0.786665359551467
1.42647707270770 0.786932107782087
1.43725595142511 0.787169173057368
1.44803504872670 0.787352305492643
1.45881374397680 0.787481690090725
1.46959163912947 0.787598367868358
1.48036877067611 0.787775037673835
1.49114535192326 0.788036018925842
1.50192145515258 0.788341776971727
0 0
1.38378213611770 0.790034278314023
1.39455037384998 0.790242138870547
1.40531970988447 0.790467519990803
1.41609033705660 0.790711653557802
1.42686226263843 0.790951749841633
1.43763512638945 0.791146871623073
1.44840835311620 0.791264735422922
1.45918136392211 0.791313077647974
1.46995379796541 0.791353264286783
1.48072570699707 0.791470260525465
1.49149726456084 0.791681602644784
1.50226847903846 0.791927371406147
0 0
1.38420658030779 0.794658952614086
1.39496845113791 0.794809662990401
1.40573143042962 0.794991060454284
1.41649573746401 0.795200624840243
1.42726141585940 0.795409404493750
1.43802814668087 0.795562338924797
1.44879539089331 0.795613379982982
1.45956260019355 0.795573831450329
1.47032943815023 0.795528034118880
1.48109596178455 0.795575239316051
1.49186231160481 0.795724908070754

1.50262844254276 0.795904548598084
0 0
1.38464537681069 0.799745986423710
1.39540066373789 0.799828073964710
1.40615709457805 0.799954834028069
1.41691492244482 0.800120664699795
1.42767422465806 0.800292487961999
1.43843471320023 0.800402287177019
1.44919587277336 0.800386760939939
1.45995717285431 0.800257156554010
1.47071828897600 0.800120897731789
1.48147927566392 0.800090789376140
1.49224024507840 0.800169458054000
1.50300110757671 0.800281363035226
0 0
1.38509820902819 0.805275925122756
1.39584668986944 0.805278259111761
1.40659637955152 0.805339686389804
1.41734757215559 0.805453887124527
1.42810037596734 0.805584622235288
1.43885452289978 0.805650613710592
1.44960950703812 0.805569823462384
1.46036480104396 0.805351138182945
1.47112007998201 0.805123739141542
1.48187538947231 0.805011997353904
1.49263081697155 0.805014592234665
1.50338623618377 0.805059675442669
0 0
1.38556476034933 0.811310498729071
1.39630620345408 0.811217961632116
1.40704895551940 0.811199608892407
1.41779335926537 0.811253907962589
1.42853955070024 0.811343945017963
1.43928726901949 0.811371256967522
1.45003600062280 0.811230689546123
1.46078520451200 0.810925341135411
1.47153454245852 0.810605118191389
1.48228404573188 0.810406308890265
1.49303378055673 0.810327502005591
1.50378359159985 0.810304394561034
0 0
1.38604471361956 0.817799405082803
1.39677887234110 0.817597214920221
1.40751448335589 0.817484584789793
1.41825194697827 0.817469936083673

1.42899142265105 0.817517893380006
1.43973264119830 0.817510693030999
1.45047506029145 0.817317792704255
1.46121810532635 0.816933033716758
1.47196141113526 0.816523701944155
1.48270499017557 0.816236935459651
1.49344889166113 0.816073819432336
1.50419293925081 0.815980872378586
0 0
1.38653775016069 0.824548098378526
1.39726435557575 0.824228948740552
1.40799261120816 0.824013497369142
1.41872298603792 0.823920748420195
1.42945565682142 0.823917164467419
1.44019032548320 0.823870197004331
1.45092639404023 0.823628578896585
1.46166322992273 0.823176208082220
1.47240042614886 0.822690498265833
1.48313797335364 0.822323600280947
1.49387590987482 0.822080248824849
1.50461404765349 0.821918442216197
0 0
1.38704354818018 0.831435255893177
1.39776229929742 0.830994845966284
1.40848296936953 0.830669733713802
1.41920611030632 0.830489413624753
1.42993190699032 0.830423150593185
1.44066000430246 0.830328540604447
1.45138971296244 0.830038710899353
1.46212031174746 0.829527975400455
1.47285133542889 0.828977670598488
1.48358275234578 0.828539646420401
1.49431459965115 0.828221860556079
1.50504668916644 0.827993136452114
0 0
1.38756178035165 0.838382920789299
1.39827233066894 0.837817301126575
1.40898516269918 0.837375247789588
1.41970093032407 0.837097902904156
1.43041981229696 0.836959520387255
1.44114135654756 0.836810295983579
1.45186473396269 0.836470963068169
1.46258909488226 0.835906145187126
1.47331389770047 0.835298408893469
1.48403909258478 0.834795872390277

1.49476473120977 0.834407921311991
0 0
1.38809211029000 0.845316077048688
1.39879404896846 0.844622035804091
1.40949875943464 0.844056573304445
1.42020702398067 0.843671167888405
1.43091899254590 0.843448306182239
1.44163405804072 0.843236767988432
1.45235118396225 0.842846722115132
1.46306933925870 0.842235349018514
1.47378788637582 0.841577039120937
1.48450676974733 0.841012404719877
1.49522608106866 0.840556765480498
0 0
1.38863418761403 0.852156809698639
1.39932701259596 0.851333481201449
1.41002327461040 0.850640550906174
1.42072392300657 0.850136818771171
1.43142904187935 0.849817852977865
1.44213778288936 0.849537277886002
1.45284880666556 0.849094999470710
1.46356082842453 0.848441837965721
1.47427309469399 0.847738864063159
1.48498557155307 0.847115138038903
1.49569843188167 0.846591872978577
0 0
1.38918764136981 0.858796242163058
1.39987072024571 0.857849018417485
1.41055814524274 0.857030379207335
1.42125109338241 0.856404697922300
1.43194952042075 0.855980561535508
1.44265220659302 0.855618144176129
1.45335737369391 0.855115760707182
1.46406338141391 0.854424511717812
1.47476934255382 0.853685256490203
1.48547529907169 0.853008170418772
1.49618157099661 0.852417221283021
0 0
1.38975207226618 0.864998613618013
1.40042458420166 0.863947879233482
1.41110269286034 0.863021504817040
1.42178790714596 0.862283747098625
1.43247994380608 0.861747730930789
1.44317701257536 0.861282457021183
1.45387670343119 0.860704721252984

1.46457687151727 0.859977161217469
1.47527648575361 0.859212809742140
1.48597576687347 0.858494501718563
1.49667528691120 0.857842685130099
0 0
1.39032704459096 0.870580608395042
1.40098789259551 0.869455969211075
1.41165606471761 0.868452526071413
1.42233360121319 0.867624425698523
1.43301977013360 0.866977692562137
1.44371190380202 0.866395758281354
1.45440669255569 0.865735196405885
1.46510125580180 0.864976356025847
1.47579442749213 0.864197918506165
1.48648679970650 0.863453097891409
1.49717936134610 0.862753495966943
0 0
1.39091208268636 0.875496218179422
1.40155975925426 0.874325325046831
1.41221713869591 0.873277496714910
1.42288721865183 0.872386599266380
1.43356838578749 0.871628708974815
1.44425662238377 0.870914081047175
1.45494737043240 0.870166289830800
1.46563662313456 0.869383160028643
1.47632313186515 0.868600573706420
1.48700822209582 0.867841327231526
1.49769355381120 0.867111319467799
0 0
-0.300000000000000 1.03251973600000
-0.218367495000000 1.03251973600000
-4.157311500000000E-002 1.01339900100000
5.946259100000000E-002 1.00000000000000
0.196494532000000 0.980299848000000
0.275300507000000 0.972405302000000
0.388642766000000 0.963879683000000
0.468168320000000 0.957775042000000
0.566451800000000 0.950025349000000
0.626566235000000 0.945853553000000
0.713116535000000 0.940175273000000
0.766640110000000 0.936191787000000
0.844861302000000 0.929600927000000
0.890200623000000 0.925762294000000
0.959151155000000 0.920040559000000
1.00593901600000 0.915984645000000

1.06960237600000 0.910552618000000
1.11052364700000 0.907148548000000
1.16911711500000 0.902151083000000
1.21126964600000 0.898602158000000
1.26566234500000 0.893966828000000
1.30158615200000 0.890924893000000
1.35460273800000 0.886506844000000
1.41326863200000 0.879626277000000
1.45998406600000 0.876294633000000
1.49330050000000 0.873904541000000
1.54428912900000 0.870283190000000
1.58253060000000 0.867530963000000
1.62997030500000 0.864126892000000
1.66437314400000 0.861664373000000
1.71811400000000 0.857825741000000
1.77801115400000 0.854204389000000
1.82421959900000 0.852176432000000
1.85333526500000 0.853480119000000
1.91497066700000 0.848192946000000
1.94220323000000 0.846961686000000
1.98377634500000 0.845151010000000
2.01347142800000 0.843847324000000
2.06656044000000 0.841457232000000
2.09726950100000 0.840153545000000
2.13413485900000 0.838487724000000
2.16636488700000 0.837111610000000
2.23002824700000 0.836677048000000
2.30000000000000 0.837000000000000
2.50000000000000 0.837000000000000
0 0
Input parameters (version 1.1)
e3c
Blade row #:
12
Number of blades in this row:
80
Blade Scaling factor (mm):
350.700000000000
Number of streamlines:
21
Angles in the input file (0=Beta_z (default),1=Beta_r):
0
Airfoil camber defined by curvature control (0=no,1=yes):
0
Airfoil Thickness distribution (0=Wennerstrom,1=Spline):

0
Airfoil Thickness multiplier (0=no,1=yes):
0
Airfoil LE defined by spline (0=no,1=yes):
0
Non-dimensional Actual chord (0=no,1=yes,2=spline):
0
Sectionwise properties:
J in_Beta out_Beta mrel_in chord t/c_max Incidence Deviation Sec. Flow Angle
1 -54.47338791 -28.21655510 0.79255895 0.08038719 0.07972391 0.00000000 0.00000000
0.00000000
2 -54.84393396 -29.69306633 0.78856519 0.07908441 0.07827014 0.00000000 0.00000000
0.00000000
3 -55.21867168 -31.05324153 0.77968914 0.07802034 0.07672903 0.00000000 0.00000000
0.00000000
4 -55.59502058 -32.47266350 0.76729720 0.07692415 0.07500573 0.00000000 0.00000000
0.00000000
5 -55.96917514 -33.83941274 0.75323011 0.07578337 0.07318849 0.00000000 0.00000000
0.00000000
6 -56.33643057 -35.14521105 0.74745883 0.07452650 0.07127287 0.00000000 0.00000000
0.00000000
7 -56.69789927 -36.36870637 0.74387642 0.07313288 0.06928824 0.00000000 0.00000000
0.00000000
8 -57.05490052 -37.47717218 0.74192983 0.07163062 0.06727496 0.00000000 0.00000000
0.00000000
9 -57.41209777 -38.46223841 0.73993707 0.07006679 0.06524981 0.00000000 0.00000000
0.00000000
10 -57.76551466 -39.35237929 0.73981042 0.06848035 0.06314126 0.00000000 0.00000000
0.00000000
11 -58.12551670 -40.17993030 0.74352924 0.06690615 0.06092231 0.00000000 0.00000000
0.00000000
12 -58.51153293 -40.91788731 0.75016005 0.06537982 0.05869019 0.00000000 0.00000000
0.00000000
13 -58.93295034 -41.55635444 0.75799364 0.06392014 0.05645899 0.00000000 0.00000000
0.00000000
14 -59.38094646 -42.11300590 0.76666738 0.06248417 0.05405318 0.00000000 0.00000000
0.00000000
15 -59.85630630 -42.51275278 0.77742465 0.06106640 0.05157168 0.00000000 0.00000000
0.00000000
16 -60.36070398 -42.79563292 0.79147211 0.05954710 0.04894448 0.00000000 0.00000000
0.00000000
17 -60.90306993 -42.90001766 0.80670743 0.05804244 0.04629060 0.00000000 0.00000000
0.00000000
18 -61.48271496 -42.73762469 0.83079259 0.05671187 0.04372461 0.00000000 0.00000000
0.00000000

19 -62.07332021 -42.29224217 0.86539487 0.05557593 0.04119909 0.00000000 0.00000000 0.00000000

20 -62.67468021 -41.54918167 0.92876102 0.05455518 0.03863126 0.00000000 0.00000000 0.00000000

21 -63.30208348 -40.60131662 1.01571935 0.05333042 0.03583723 0.00000000 0.00000000 0.00000000

LE / TE curve (x,r) definition :

Number of Curve points :

12

xLE rLE xTE rTE

1.40711200 0.77265200 1.46925500 0.77402800

1.40733000 0.77866300 1.46838600 0.78025600

1.40769200 0.78996200 1.46708200 0.79119300

1.40812600 0.80075300 1.46577800 0.80126000

1.40877800 0.81140000 1.46461900 0.81103800

1.40935800 0.82190200 1.46353300 0.82081600

1.40993700 0.83240400 1.46266400 0.83052100

1.41052200 0.84283300 1.46186700 0.84029800

1.41131300 0.85340800 1.46107000 0.85007600

1.41211000 0.86412700 1.46049100 0.86028800

1.41268900 0.87245600 1.46020100 0.86854500

1.41326900 0.87962600 1.45998400 0.87629500

Airfoil type and Variable Radial Stacking information.

stack_u: % chord stack (0.00 to 100.00).

stack_v: % below or above meanline stack (-100.00 to +100.00).

Use +200 for stacking on airfoil area centroid.

Variable Radial stacking (0=no,1=yes):

0

J type |stk_u |stk_v |umxthk |lethk |tethk |Jcells(Grid:4n+1) |eta_ofst(<=10){%thkc/Jmax} |BGgrid(0=no,1=yes) |

1 sect1 25.00 0.00 0.30 0.02 0.02 33 10 1

2 sect1 25.00 0.00 0.30 0.02 0.02 33 10 1

3 sect1 25.00 0.00 0.30 0.02 0.02 33 10 1

4 sect1 25.00 0.00 0.30 0.02 0.02 33 10 1

5 sect1 25.00 0.00 0.30 0.02 0.02 33 10 1

6 sect1 25.00 0.00 0.30 0.02 0.02 33 10 1

7 sect1 25.00 0.00 0.30 0.02 0.02 33 10 1

8 sect1 25.00 0.00 0.30 0.02 0.02 33 10 1

9 sect1 25.00 0.00 0.30 0.02 0.02 33 10 1

10 sect1 25.00 0.00 0.30 0.02 0.02 33 10 1

11 sect1 25.00 0.00 0.30 0.02 0.02 33 10 1

12 sect1 25.00 0.00 0.30 0.02 0.02 33 10 1

13 sect1 25.00 0.00 0.30 0.02 0.02 33 10 1

14 sect1 25.00 0.00 0.30 0.02 0.02 33 10 1

15 sect1 25.00 0.00 0.30 0.02 0.02 33 10 1

16 sect1 25.00 0.00 0.30 0.02 0.02 33 10 1
17 sect1 25.00 0.00 0.30 0.02 0.02 33 10 1
18 sect1 25.00 0.00 0.30 0.02 0.02 33 10 1
19 sect1 25.00 0.00 0.30 0.02 0.02 33 10 1
20 sect1 25.00 0.00 0.30 0.02 0.02 33 10 1
21 sect1 25.00 0.00 0.30 0.02 0.02 33 10 1
Control table for blending section variable:
5 0 0
span bf1 bf2
0.000000000000000E+000 1 0
0.250000000000000 1 0
0.500000000000000 1 0
0.750000000000000 1 0
1.00000000000000 1 0
Stacking axis location (200=centroid):
25000
Control points for delta_m:
5 0
span delta_m True_sweep
0.000000000000000E+000 0.000000000000000E+000 0.0
0.250000000000000 0.000000000000000E+000 0.0
0.500000000000000 0.000000000000000E+000 0.0
0.750000000000000 0.000000000000000E+000 0.0
1.00000000000000 0.000000000000000E+000 0.0
Control points for delta_theta:
8 1
span delta_theta True_lean
0.000000000000000E+000 0.000000000000000E+000 0.0
0.250000000000000 0.000000000000000E+000 0.0
0.500000000000000 0.000000000000000E+000 0.0
0.750000000000000 0.000000000000000E+000 0.0
0.800000000000000 0.00000000000000E+000 0.0
0.900000000000000 0.004000000000000E+000 0.0016
0.950000000000000 0.008000000000000E+00 0.0033
1.00000000000000 0.012000000000000E+000 0.0050
Control points for in_beta*:
5
span in_beta*
0.000000000000000E+000 0.000000000000000E+000
0.250000000000000 0.000000000000000E+000
0.500000000000000 0.000000000000000E+000
0.750000000000000 0.000000000000000E+000
1.00000000000000 0.000000000000000E+000
Control points for out_beta*:
5

span out_beta*
0.000000000000000E+000 0.000000000000000E+000
0.250000000000000 0.000000000000000E+000
0.500000000000000 0.000000000000000E+000
0.750000000000000 0.000000000000000E+000
1.00000000000000 0.000000000000000E+000
Control points for chord:
5
span chord
0.000000000000000E+000 0.000000000000000E+000
0.250000000000000 0.000000000000000E+000
0.500000000000000 0.000000000000000E+000
0.750000000000000 0.000000000000000E+000
1.00000000000000 0.000000000000000E+000
Control points for tm/c:
5
span tm/c
0.000000000000000E+000 0.000000000000000E+000
0.250000000000000 0.000000000000000E+000
0.500000000000000 0.000000000000000E+000
0.750000000000000 0.000000000000000E+000
1.00000000000000 0.000000000000000E+000
Hub offset
0.005000000000000E+000
Tip offset
0.000000000000000E+000
Streamline Data
x_s r_s
-0.300000000000000 0.494387000000000
-0.200000000000000 0.494387000000000
-0.186572000000000 0.494387000000000
-7.025421900000001E-002 0.492938365000000
0.000000000000000E+000 0.507423771000000
0.263851669000000 0.580068081000000
0.293891489000000 0.588552850000000
0.398736643000000 0.618549342000000
0.440935757000000 0.630187586000000
0.603606866000000 0.673643804000000
0.636633592000000 0.681538350000000
0.714130514000000 0.699645108000000
0.752227131000000 0.707322373000000
0.866009995000000 0.727239806000000
0.897443326000000 0.732309698000000
0.961034258000000 0.742232201000000
0.995364670000000 0.746288115000000

1.08676758200000 0.754834504000000
1.11573839400000 0.757804012000000
1.17063808200000 0.763453321000000
1.20207141300000 0.765336424000000
1.27906134600000 0.767581661000000
1.30390381700000 0.768595640000000
1.35402332200000 0.770768451000000
1.40711233400000 0.772651554000000
1.46925472600000 0.774027667000000
1.49554573800000 0.775041646000000
1.54363728500000 0.777069602000000
1.57651915700000 0.778083581000000
1.63902368400000 0.779242413000000
1.66574925800000 0.779169986000000
1.71876584300000 0.778952705000000
1.77323097000000 0.779097559000000
1.83138987500000 0.780401246000000
1.85348011900000 0.780328819000000
1.91200115900000 0.779966684000000
1.93785760800000 0.780111538000000
1.99043963200000 0.780618527000000
2.01318171900000 0.780546100000000
2.06569131600000 0.780111538000000
2.09386543100000 0.780183965000000
2.13935000000000 0.780619000000000
2.16810313600000 0.780473673000000
2.23002824700000 0.780039111000000
2.30000000000000 0.780000000000000
2.50000000000000 0.780000000000000
0 0
1.38223421793494 0.776089231747206
1.39302575258406 0.776427586371302
1.40381853447651 0.776743276534340
1.41461277158334 0.777046875718339
1.42540828507959 0.777368510346849
1.43620442198022 0.777720663126003
1.44700036940181 0.778065914779841
1.45779533661827 0.778371782442426
1.46858873318392 0.778642576837112
1.47938043909526 0.778935482437679
1.49017087126078 0.779284425194044
1.50096038090340 0.779693978576179
1.51174933466604 0.780096369593644
0 0
1.38259808552201 0.778988542253906

1.39338412717120 0.779304700598530
1.40417135697879 0.779605999781926
1.41495995186279 0.779903720115986
1.42574978861637 0.780212427149267
1.43654031186873 0.780532052551585
1.44733077858880 0.780832365329987
1.45812045936375 0.781091217773241
1.46890884139311 0.781321079900359
1.47969588331934 0.781582958645588
1.49048191349550 0.781908186194946
1.50126717264268 0.782295732564068
0 0
1.38297757191222 0.782222579140842
1.39375789698175 0.782511501806866
1.40453936320229 0.782794924188213
1.41532213881355 0.783081995351970
1.42610614876825 0.783371894475145
1.43689091657930 0.783651547787885
1.44767576349840 0.783896564679087
1.45846001790102 0.784096392656085
1.46924323121907 0.784275785982663
1.48002541096159 0.784499917542491
1.49080682028723 0.784797514394142
1.50158760800746 0.785151037327541
0 0
1.38337236102054 0.785882593139950
1.39414675045853 0.786136414598445
1.40492225006256 0.786395539603582
1.41569903482055 0.786665359551467
1.42647707270770 0.786932107782087
1.43725595142511 0.787169173057368
1.44803504872670 0.787352305492643
1.45881374397680 0.787481690090725
1.46959163912947 0.787598367868358
1.48036877067611 0.787775037673835
1.49114535192326 0.788036018925842
1.50192145515258 0.788341776971727
0 0
1.38378213611770 0.790034278314023
1.39455037384998 0.790242138870547
1.40531970988447 0.790467519990803
1.41609033705660 0.790711653557802
1.42686226263843 0.790951749841633
1.43763512638945 0.791146871623073
1.44840835311620 0.791264735422922

1.45918136392211 0.791313077647974
1.46995379796541 0.791353264286783
1.48072570699707 0.791470260525465
1.49149726456084 0.791681602644784
1.50226847903846 0.791927371406147
0 0
1.38420658030779 0.794658952614086
1.39496845113791 0.794809662990401
1.40573143042962 0.794991060454284
1.41649573746401 0.795200624840243
1.42726141585940 0.795409404493750
1.43802814668087 0.795562338924797
1.44879539089331 0.795613379982982
1.45956260019355 0.795573831450329
1.47032943815023 0.795528034118880
1.48109596178455 0.795575239316051
1.49186231160481 0.795724908070754
1.50262844254276 0.795904548598084
0 0
1.38464537681069 0.799745986423710
1.39540066373789 0.799828073964710
1.40615709457805 0.799954834028069
1.41691492244482 0.800120664699795
1.42767422465806 0.800292487961999
1.43843471320023 0.800402287177019
1.44919587277336 0.800386760939939
1.45995717285431 0.800257156554010
1.47071828897600 0.800120897731789
1.48147927566392 0.800090789376140
1.49224024507840 0.800169458054000
1.50300110757671 0.800281363035226
0 0
1.38509820902819 0.805275925122756
1.39584668986944 0.805278259111761
1.40659637955152 0.805339686389804
1.41734757215559 0.805453887124527
1.42810037596734 0.805584622235288
1.43885452289978 0.805650613710592
1.44960950703812 0.805569823462384
1.46036480104396 0.805351138182945
1.47112007998201 0.805123739141542
1.48187538947231 0.805011997353904
1.49263081697155 0.805014592234665
1.50338623618377 0.805059675442669
0 0

1.38556476034933 0.811310498729071
1.39630620345408 0.811217961632116
1.40704895551940 0.811199608892407
1.41779335926537 0.811253907962589
1.42853955070024 0.811343945017963
1.43928726901949 0.811371256967522
1.45003600062280 0.811230689546123
1.46078520451200 0.810925341135411
1.47153454245852 0.810605118191389
1.48228404573188 0.810406308890265
1.49303378055673 0.810327502005591
1.50378359159985 0.810304394561034
0 0
1.38604471361956 0.817799405082803
1.39677887234110 0.817597214920221
1.40751448335589 0.817484584789793
1.41825194697827 0.817469936083673
1.42899142265105 0.817517893380006
1.43973264119830 0.817510693030999
1.45047506029145 0.817317792704255
1.46121810532635 0.816933033716758
1.47196141113526 0.816523701944155
1.48270499017557 0.816236935459651
1.49344889166113 0.816073819432336
1.50419293925081 0.815980872378586
0 0
1.38653775016069 0.824548098378526
1.39726435557575 0.824228948740552
1.40799261120816 0.824013497369142
1.41872298603792 0.823920748420195
1.42945565682142 0.823917164467419
1.44019032548320 0.823870197004331
1.45092639404023 0.823628578896585
1.46166322992273 0.823176208082220
1.47240042614886 0.822690498265833
1.48313797335364 0.822323600280947
1.49387590987482 0.822080248824849
1.50461404765349 0.821918442216197
0 0
1.38704354818018 0.831435255893177
1.39776229929742 0.830994845966284
1.40848296936953 0.830669733713802
1.41920611030632 0.830489413624753
1.42993190699032 0.830423150593185
1.44066000430246 0.830328540604447

1.45138971296244 0.830038710899353
1.46212031174746 0.829527975400455
1.47285133542889 0.828977670598488
1.48358275234578 0.828539646420401
1.49431459965115 0.828221860556079
1.50504668916644 0.827993136452114
0 0
1.38756178035165 0.838382920789299
1.39827233066894 0.837817301126575
1.40898516269918 0.837375247789588
1.41970093032407 0.837097902904156
1.43041981229696 0.836959520387255
1.44114135654756 0.836810295983579
1.45186473396269 0.836470963068169
1.46258909488226 0.835906145187126
1.47331389770047 0.835298408893469
1.48403909258478 0.834795872390277
1.49476473120977 0.834407921311991
0 0
1.38809211029000 0.845316077048688
1.39879404896846 0.844622035804091
1.40949875943464 0.844056573304445
1.42020702398067 0.843671167888405
1.43091899254590 0.843448306182239
1.44163405804072 0.843236767988432
1.45235118396225 0.842846722115132
1.46306933925870 0.842235349018514
1.47378788637582 0.841577039120937
1.48450676974733 0.841012404719877
1.49522608106866 0.840556765480498
0 0
1.38863418761403 0.852156809698639
1.39932701259596 0.851333481201449
1.41002327461040 0.850640550906174
1.42072392300657 0.850136818771171
1.43142904187935 0.849817852977865
1.44213778288936 0.849537277886002
1.45284880666556 0.849094999470710
1.46356082842453 0.848441837965721
1.47427309469399 0.847738864063159
1.48498557155307 0.847115138038903
1.49569843188167 0.846591872978577
0 0
1.38918764136981 0.858796242163058
1.39987072024571 0.857849018417485

1.41055814524274 0.857030379207335
1.42125109338241 0.856404697922300
1.43194952042075 0.855980561535508
1.44265220659302 0.855618144176129
1.45335737369391 0.855115760707182
1.46406338141391 0.854424511717812
1.47476934255382 0.853685256490203
1.48547529907169 0.853008170418772
1.49618157099661 0.852417221283021
0 0
1.38975207226618 0.864998613618013
1.40042458420166 0.863947879233482
1.41110269286034 0.863021504817040
1.42178790714596 0.862283747098625
1.43247994380608 0.861747730930789
1.44317701257536 0.861282457021183
1.45387670343119 0.860704721252984
1.46457687151727 0.859977161217469
1.47527648575361 0.859212809742140
1.48597576687347 0.858494501718563
1.49667528691120 0.857842685130099
0 0
1.39032704459096 0.870580608395042
1.40098789259551 0.869455969211075
1.41165606471761 0.868452526071413
1.42233360121319 0.867624425698523
1.43301977013360 0.866977692562137
1.44371190380202 0.866395758281354
1.45440669255569 0.865735196405885
1.46510125580180 0.864976356025847
1.47579442749213 0.864197918506165
1.48648679970650 0.863453097891409
1.49717936134610 0.862753495966943
0 0
1.39091208268636 0.875496218179422
1.40155975925426 0.874325325046831
1.41221713869591 0.873277496714910
1.42288721865183 0.872386599266380
1.43356838578749 0.871628708974815
1.44425662238377 0.870914081047175
1.45494737043240 0.870166289830800
1.46563662313456 0.869383160028643
1.47632313186515 0.868600573706420
1.48700822209582 0.867841327231526
1.49769355381120 0.867111319467799

0 0
-0.300000000000000 1.03251973600000
-0.218367495000000 1.03251973600000
-4.157311500000000E-002 1.01339900100000
5.946259100000000E-002 1.00000000000000
0.196494532000000 0.980299848000000
0.275300507000000 0.972405302000000
0.388642766000000 0.963879683000000
0.468168320000000 0.957775042000000
0.566451800000000 0.950025349000000
0.626566235000000 0.945853553000000
0.713116535000000 0.940175273000000
0.766640110000000 0.936191787000000
0.844861302000000 0.929600927000000
0.890200623000000 0.925762294000000
0.959151155000000 0.920040559000000
1.00593901600000 0.915984645000000
1.06960237600000 0.910552618000000
1.11052364700000 0.907148548000000
1.16911711500000 0.902151083000000
1.21126964600000 0.898602158000000
1.26566234500000 0.893966828000000
1.30158615200000 0.890924893000000
1.35460273800000 0.886506844000000
1.41326863200000 0.879626277000000
1.45998406600000 0.876294633000000
1.49330050000000 0.873904541000000
1.54428912900000 0.870283190000000
1.58253060000000 0.867530963000000
1.62997030500000 0.864126892000000
1.66437314400000 0.861664373000000
1.71811400000000 0.857825741000000
1.77801115400000 0.854204389000000
1.82421959900000 0.852176432000000
1.85333526500000 0.853480119000000
1.91497066700000 0.848192946000000
1.94220323000000 0.846961686000000
1.98377634500000 0.845151010000000
2.01347142800000 0.843847324000000
2.06656044000000 0.841457232000000
2.09726950100000 0.840153545000000
2.13413485900000 0.838487724000000
2.16636488700000 0.837111610000000
2.23002824700000 0.836677048000000
2.30000000000000 0.837000000000000

2.500000000000000 0.837000000000000
0 0

Appendix B

Star-CCM+ Macros

Macro to import curves into Star-CCM+

```
// STAR-CCM+ macro: sectionImport.java
    package macro;
    import java.util.*;
    import star.cadmodeler.*;
    import star.common.*;
    import star.base.neo.*;
    public class sectionImport extends StarMacro {
    public void execute() {
    execute0();
    // Units conversion
    }
    private void execute0() {
    Simulation simulation_0 =
    getActiveSimulation();
    CadModel cadModel_0 =
    ((CadModel) simulation_0.get(SolidModelManager.class).getObject("3D-CAD Model
1"));
    LabCoordinateSystem labCoordinateSystem_0 =
    simulation_0.getCoordinateSystemManager().getLabCoordinateSystem();
    // for (int i = 1; i <= 21; i++) {
    // String ii = Integer.toString(i);
    // cadModel_0.getFeatureManager().create3DSketches("C:\\Users\\Acer\\SkyDrive\\eee
blades\\12\\top_periodic.sec" + ii + ".e3c.csv", labCoordinateSystem_0, false, true);
    // }
    // for (int i = 1; i <= 21; i++) {
    // String ii = Integer.toString(i);
    // cadModel_0.getFeatureManager().create3DSketches("C:\\Users\\Acer\\SkyDrive\\eee
blades\\12\\negative lean\\sec" + ii + ".e3c.csv", labCoordinateSystem_0, true, true);
    // }
    for (int i = 1; i <= 21; i++) {
    String ii = Integer.toString(i);
```

```
    cadModel_0.getFeatureManager().create3DSketches("C:\\Users\\Acer\\SkyDrive\\eee
blades\\12\\positive lean\\sec" + ii + ".e3c.csv", labCoordinateSystem_0, true, true);
    }
    // cadModel_0.getFeatureManager().create3DSketches("C:\\Users\\Acer\\Desktop\\fortran
test\\inlet_cas_cic.csv", labCoordinateSystem_0, true, true);
    // cadModel_0.getFeatureManager().create3DSketches("C:\\Users\\Acer\\Desktop\\fortran
test\\outlet_cas_cic.csv", labCoordinateSystem_0, true, true);
    // cadModel_0.getFeatureManager().create3DSketches("C:\\Users\\Acer\\Desktop\\fortran
test\\inlet_hub_cic.csv", labCoordinateSystem_0, true, true);
    // cadModel_0.getFeatureManager().create3DSketches("C:\\Users\\Acer\\Desktop\\fortran
test\\outlet_hub_cic.csv", labCoordinateSystem_0, true, true);
    // cadModel_0.getFeatureManager().create3DSketches("C:\\Users\\Acer\\Desktop\\New
folder\\casing.csv", labCoordinateSystem_0, false, true);
    // cadModel_0.getFeatureManager().create3DSketches("C:\\Users\\Acer\\Desktop\\New
folder\\hub.csv", labCoordinateSystem_0, false, true);
    // for (int i = 1; i <= 21; i++) {
    // String ii = Integer.toString(i);
    // cadModel_0.getFeatureManager().create3DSketches("C:\\Users\\Acer\\SkyDrive\\eee
blades\\12\\bot_periodic.sec" + ii + ".e3c.csv", labCoordinateSystem_0, false, true);
    // }
    }
    }
```

Macro for running a Speedline automatically

```
// STAR-CCM+ macro: automate.java
    import java.util.*;
    import star.common.*;
    import star.base.neo.*;
    import star.flow.*;
    public class automate extends StarMacro {
    public void execute() {
    execute0();
    }
    double[] pb = {7.0,7.25,7.5,7.75,8,8.1,8.213,8.3};
    private void execute0() {
    Simulation simulation_0 = getActiveSimulation();
    Solution solution_0 = simulation_0.getSolution();
    solution_0.clearSolution();
    Region region_0 = simulation_0.getRegionManager().getRegion("Region");
    Boundary boundary_0 = region_0.getBoundaryManager().getBoundary("Body 7.out-
let");
    StaticPressureProfile staticPressureProfile_0 = boundary_0.getValues().get(StaticPressureProfile.cl
    for ( int i = 0; i<8;i++) {
```

```
    staticPressureProfile_0.getMethod(RadialEquilibriumProfile.class).getHubPressure().setValue(pb[i]
    simulation_0.getSimulationIterator().run();
    simulation_0.saveState(resolvePath(".\\rotor6_pb_splittip"+pb[i]+".sim"));
    // Scene scene_0 = simulation_0.getSceneManager().getScene("Scalar Scene 1");
    // scene_0.initializeAndWait();
    // scene_0.open(true);
    // PartDisplayer partDisplayer_0 = ((PartDisplayer) scene_0.getDisplayerManager().getDisplayer("
1"));
    // partDisplayer_0.initialize();
    // ScalarDisplayer scalarDisplayer_0 = ((ScalarDisplayer) scene_0.getDisplayerNabager().getDsipla
1"));
    // scalarDisplayer_0.initialize();
    // PrimitiveFieldDunction primitiveFieldFunction_0 = ((PrimitiveFieldFunction) sim-
ulation_0.getFieldFunction().getFunction("Static Pressure"));
    // scalarDisplayer_0.getScalarDisplayerQuantity().setFieldFunction(primitiveFieldFunction_0);
    // scene_0.printAndWait(resolvePath(".\\rotor6_pb_splittip"+pb[i]+"_ps.png"),1,
1.035, 428);
    // PrimitiveFieldDunction primitiveFieldFunction_1 = ((PrimitiveFieldFunction) sim-
ulation_0.getFieldFunction().getFunction("RelativeMachNumber"));
    // scalarDisplayer_0.getScalarDisplayerQuantity().setFieldFunction(primitiveFieldFunction_1);
    // scene_0.printAndWait(resolvePath(".\\rotor6_pb_splittip"+pb[i]+"_rmach.png"),1,
1.035, 428);
    // new star.common.SimulationSummaryReporter().report(getActiveSimulation(), re-
solvePath(".\\rotor6_pb_splittip"+pb[i]+"_report.html"));
    // p = p + 0.1;
    solution_0.clearSolution();
    }
    }
    }
```

Appendix C

Calculating the Mass Weighted Theta Averaged Values in Star-CCM+

Coordinate system averaging combines the three-dimensional STAR-CCM+ solution results with a typical two-dimensional meridional view. While the meridional view is commonly used in turbomachinery, it can also be applied to certain other applications that involve axisymmetric regions. This technique can provide an average of results in the direction, although you can choose any direction for projecting this average. The calculation is defined as:

$$\bar{\psi} = \frac{\int \psi d\theta}{\int d\theta} \tag{5.1}$$

This definition can be implemented in STAR-CCM+ with a csavg() field function, in a coordinate system and direction that you specify: csavg($Pressure, @CoordinateSystem("Block-Mapped 1"), 2, 0, 20, 20) where, in this example:

- $Pressure is the scalar being defined. (A vector can also be defined in this type of field function.)
- CoordinateSystem("Block-Mapped 1") is the (block-mapped) coordinate system being used for the averaging.
- 2 is the averaging direction.(0-x, 1-y, 2-z)
- 0 is the slice direction.
- 20, 20 are the number of slices and the integrations per slice, respectively.

Using a two-dimensional grid, the approach involves projecting region vertices to the grid and interpolating the average to the vertices.

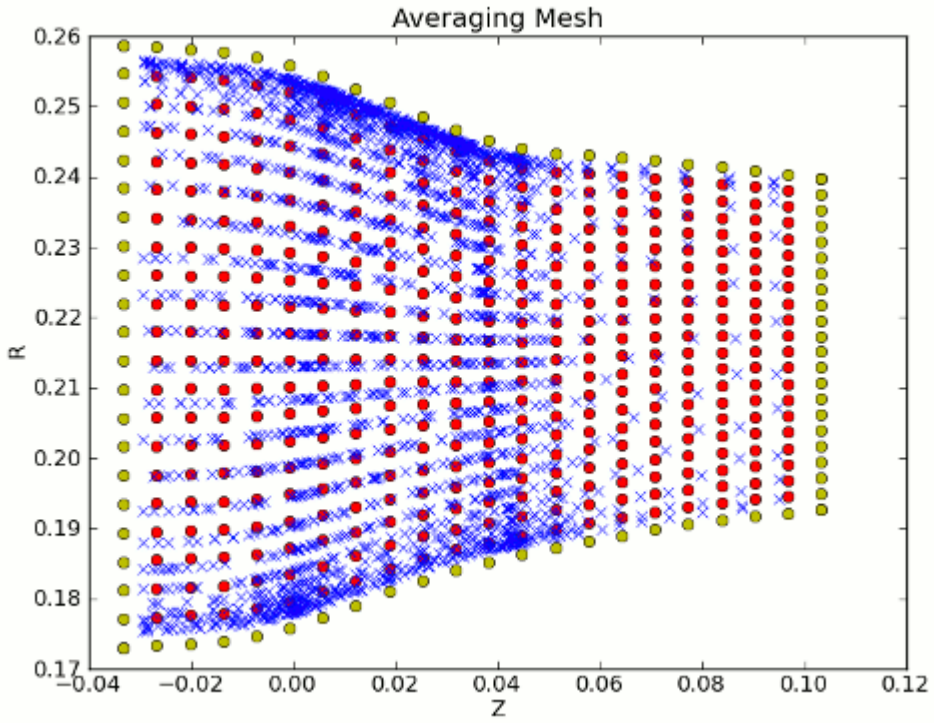

Figure 5.1: CS Averaging Mesh.

- Red dots are the resulting average mesh.
- Blue "x" symbols are the (z, r) vertices from the region projected onto this mesh.
- Green dots are extrapolated (halo) nodes from the average mesh.

Appendix D

Mass Weighted Theta Averaged Plots

The mass weighted Theta averaged plots are shown here for all the clearance cases. They are plotted on the plane downstream of the blade as shown in Figure 4.30. The upstream beta values are plotted at the upstream location shown in Figure 4.30. By comparing these plots it is possible to get an understanding as to how the different flow parameters are changing as with the split tip and baseline blade. Also it is possible to see the effect the spit tip has on the performance of the blade as the clearance is increased compared to the baseline case.

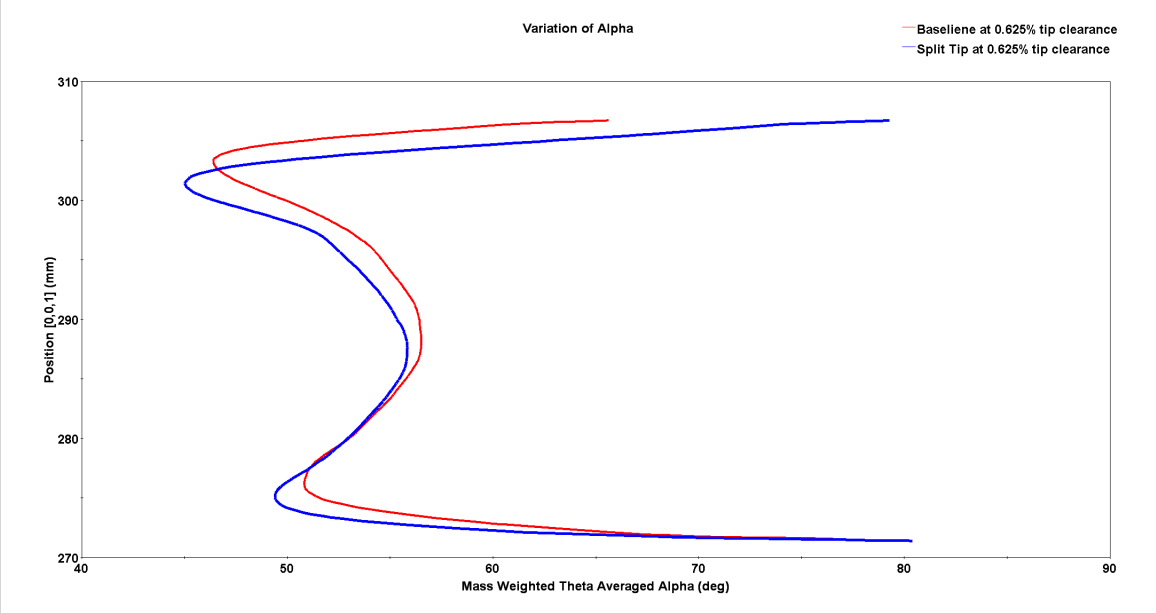

Figure 5.2: Mass Weighted Theta Averaged Alpha at 0.5x clearance for Pb of 8.1 atm

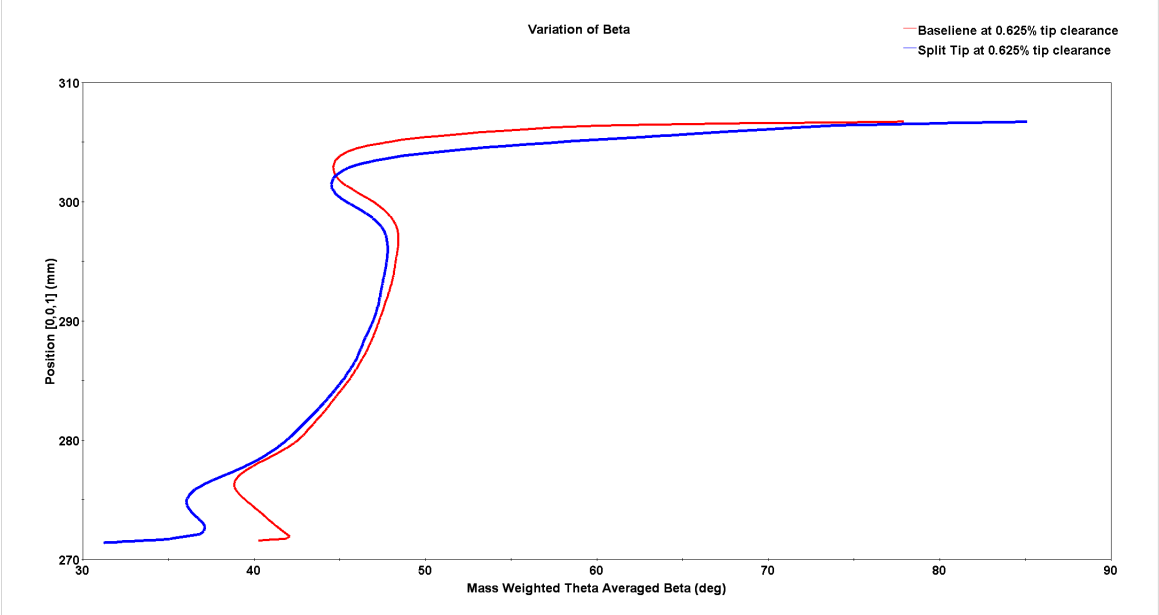

Figure 5.3: Mass Weighted Theta Averaged Beta at 0.5x clearance for Pb of 8.1 atm.

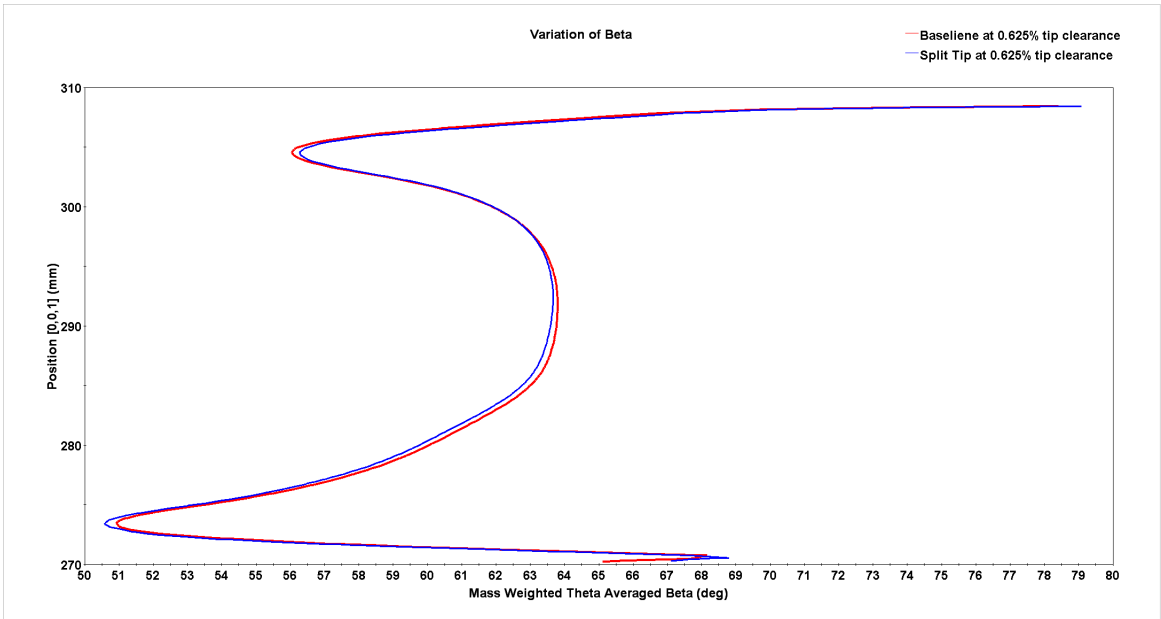

Figure 5.4: Mass Weighted Theta Averaged Beta just upstream of the blade at 0.5x clearance and pb 8.1 atm

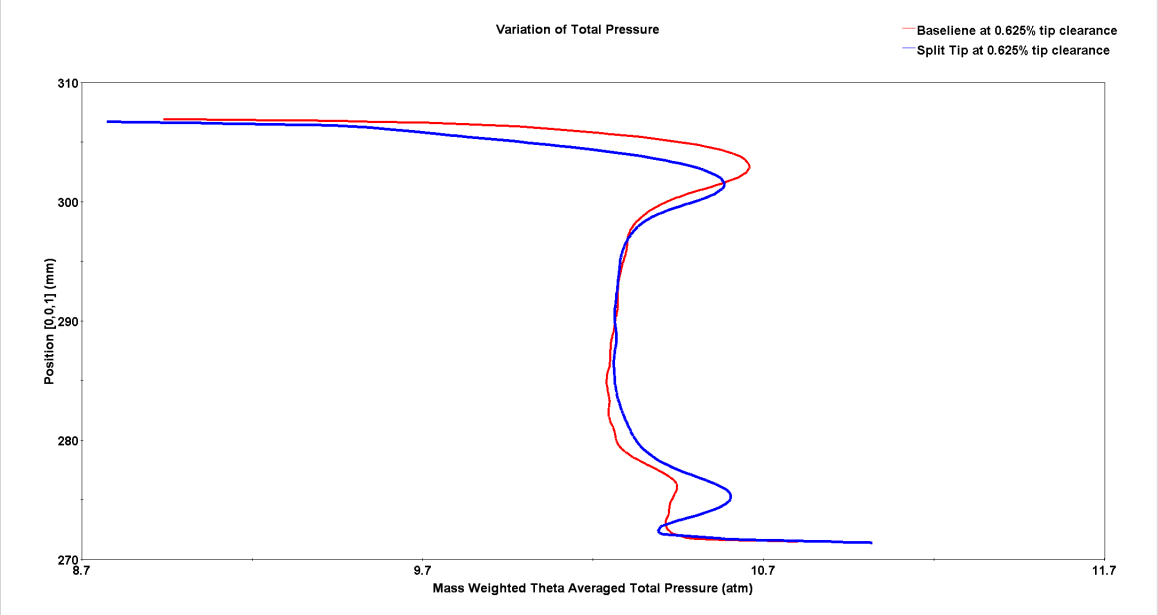

Figure 5.5: Mass Weighted Theta Averaged Total Pressure at 0.5x clearance for pb 8.1 atm

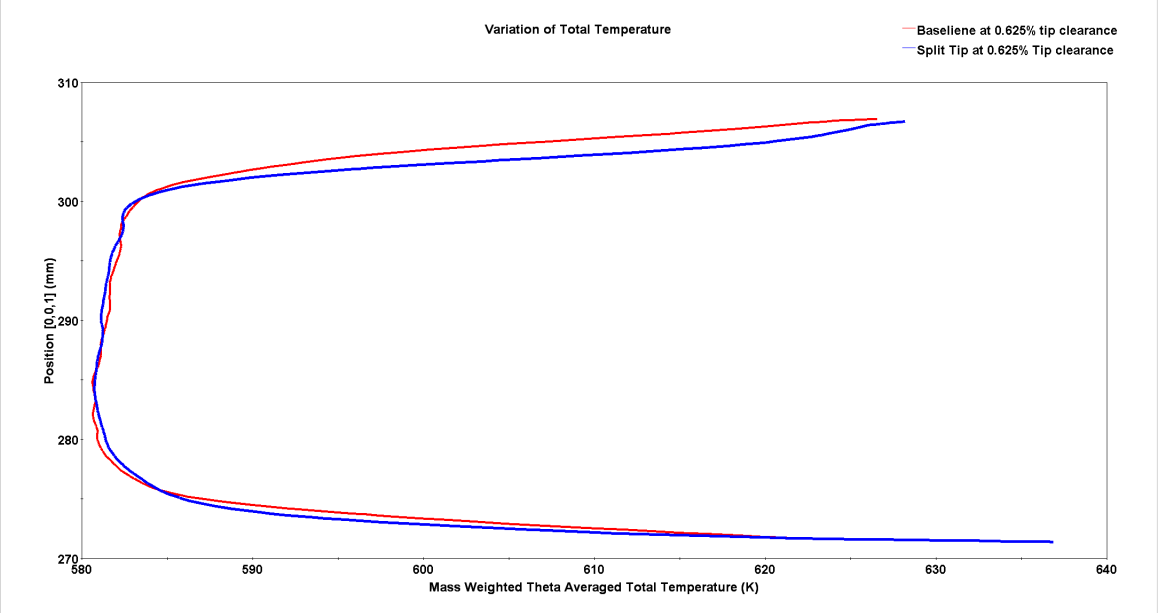

Figure 5.6: Mass Weighted Theta Averaged Total Temperature at 0.5x clearance for pb 8.1 atm.

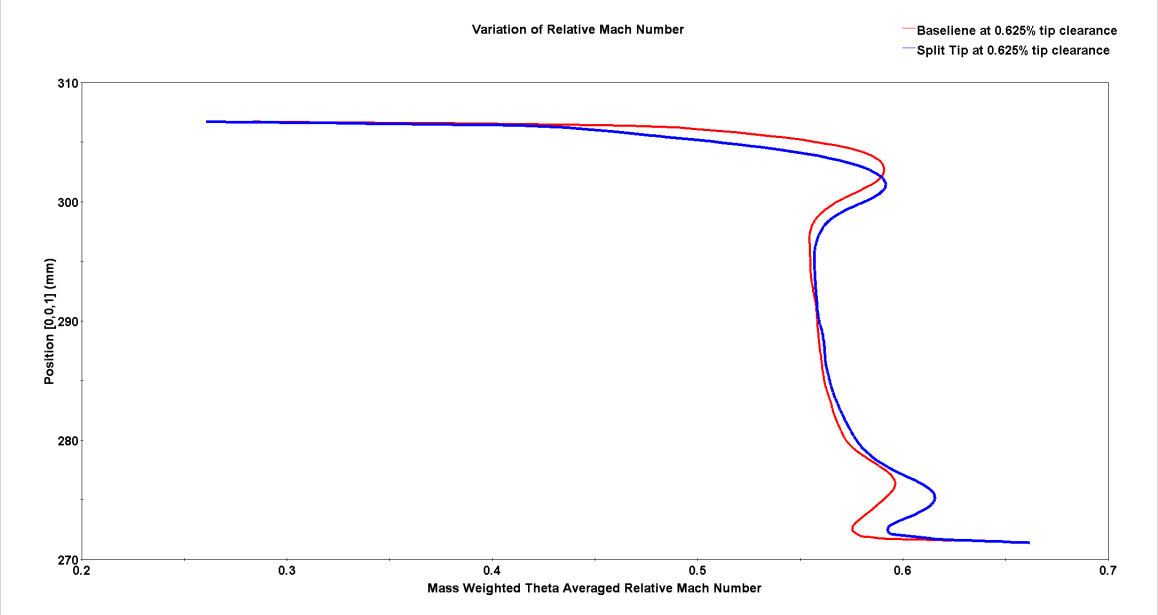

Figure 5.7: Mass Weighted Theta Averaged Relative Mach Number for 0.5x clearance at pb 8.1 atm.

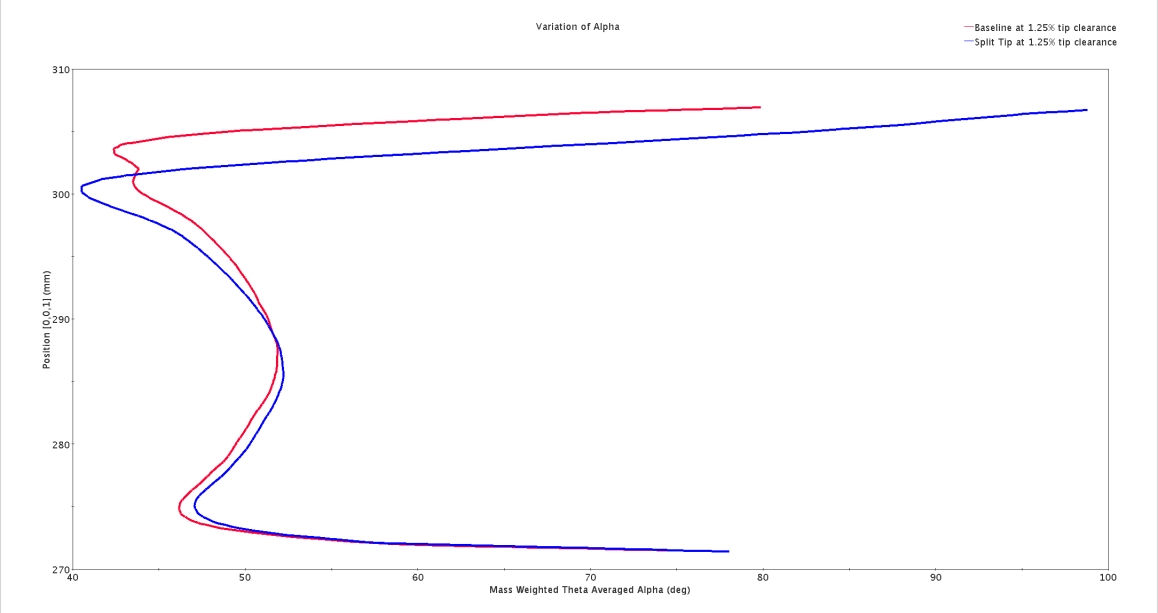

Figure 5.8: Mass Weighted Theta Averaged Alpha at 1x clearance for Pb of 7.95 atm

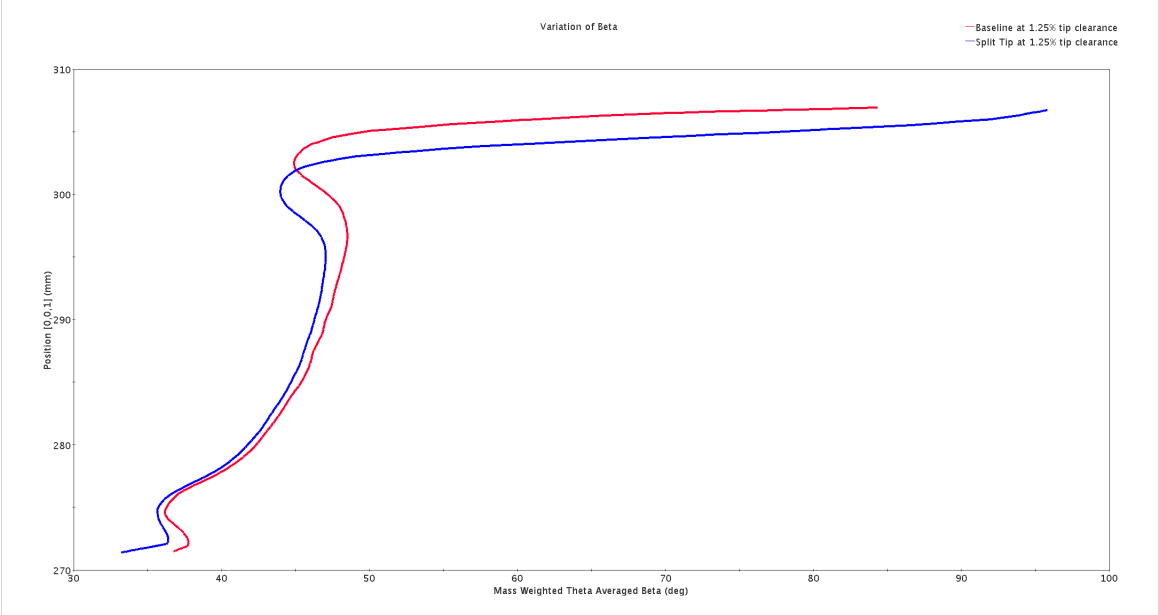

Figure 5.9: Mass Weighted Theta Averaged Beta at 1x clearance for Pb of 7.95 atm.

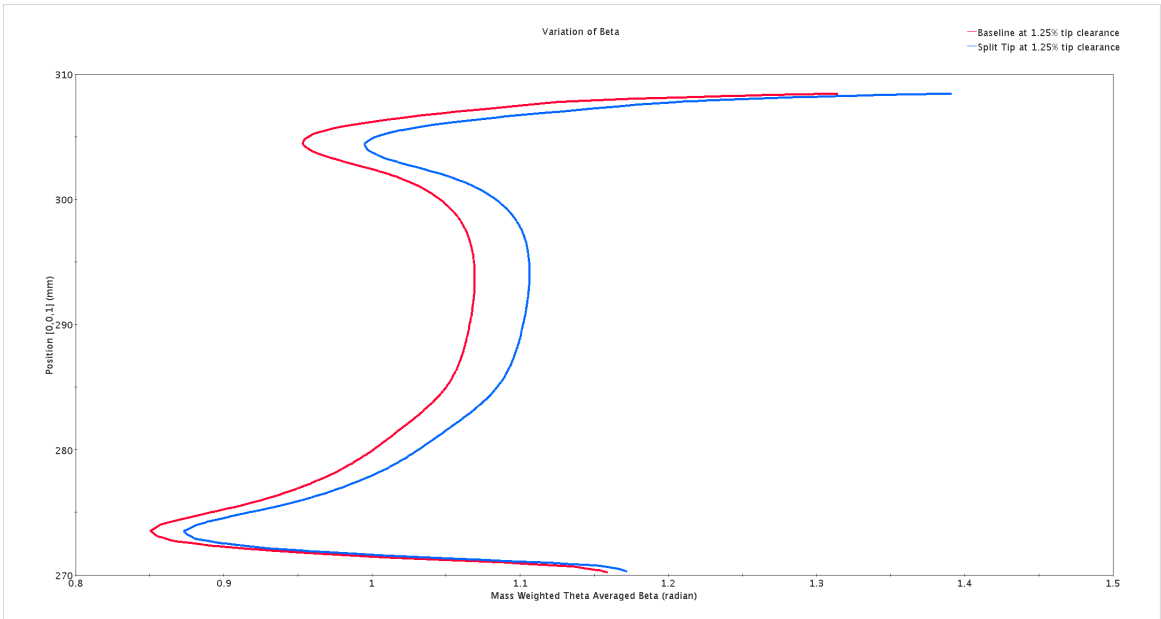

Figure 5.10: Mass Weighted Theta Averaged Beta just upstream of the blade at 1x clearance and pb 7.95 atm

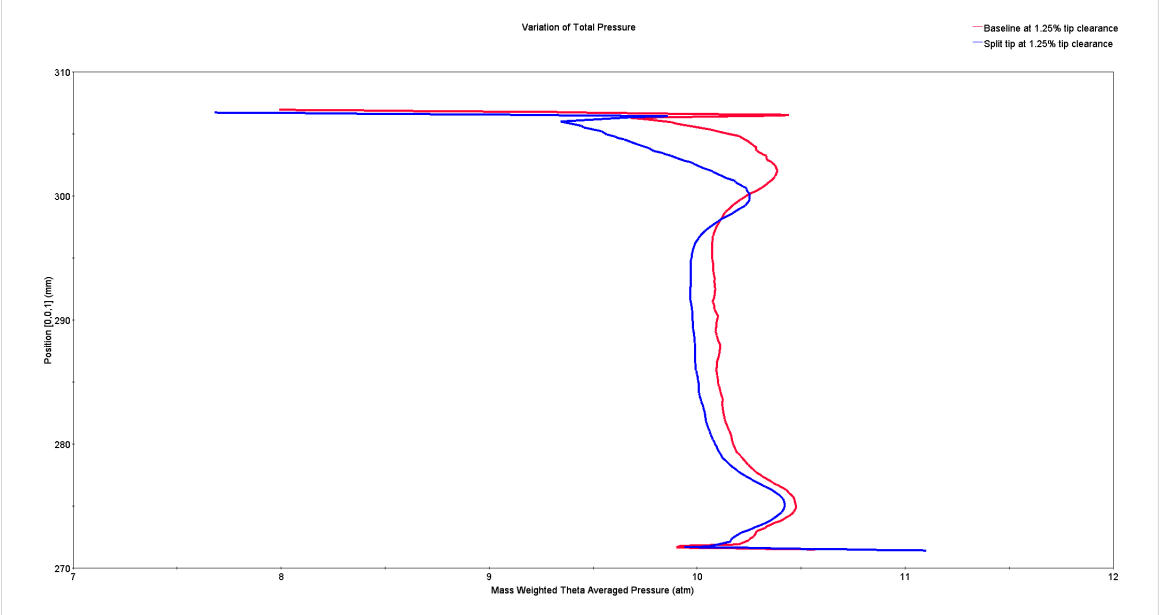

Figure 5.11: Mass Weighted Theta Averaged Total Pressure at 1x clearance for pb 7.95 atm

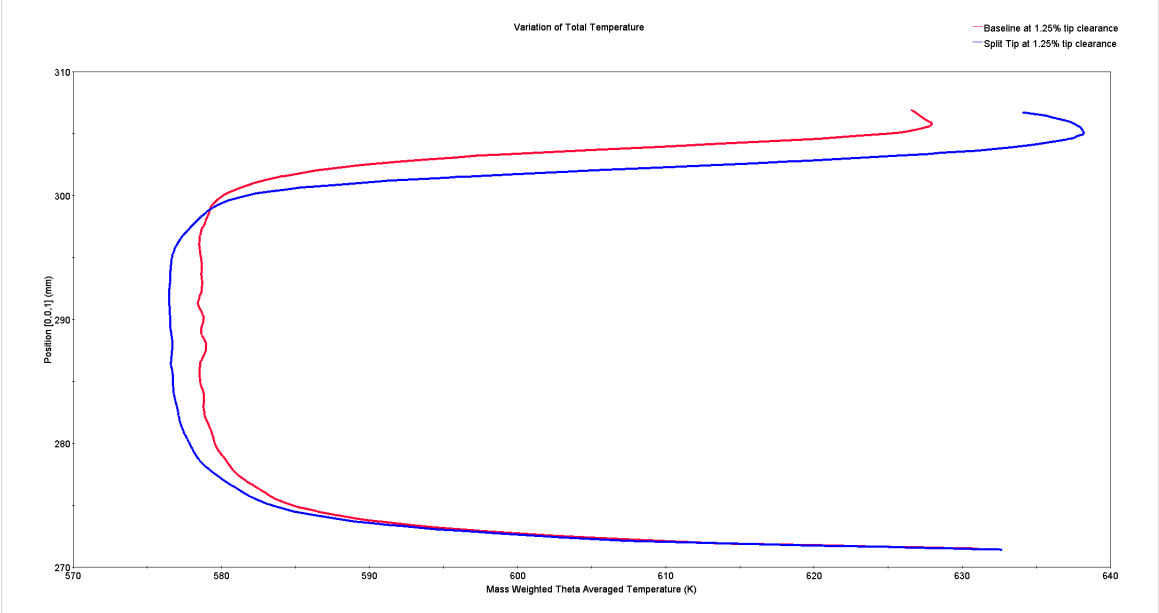

Figure 5.12: Mass Weighted Theta Averaged Total Temperature at 1x clearance for pb 7.95 atm.

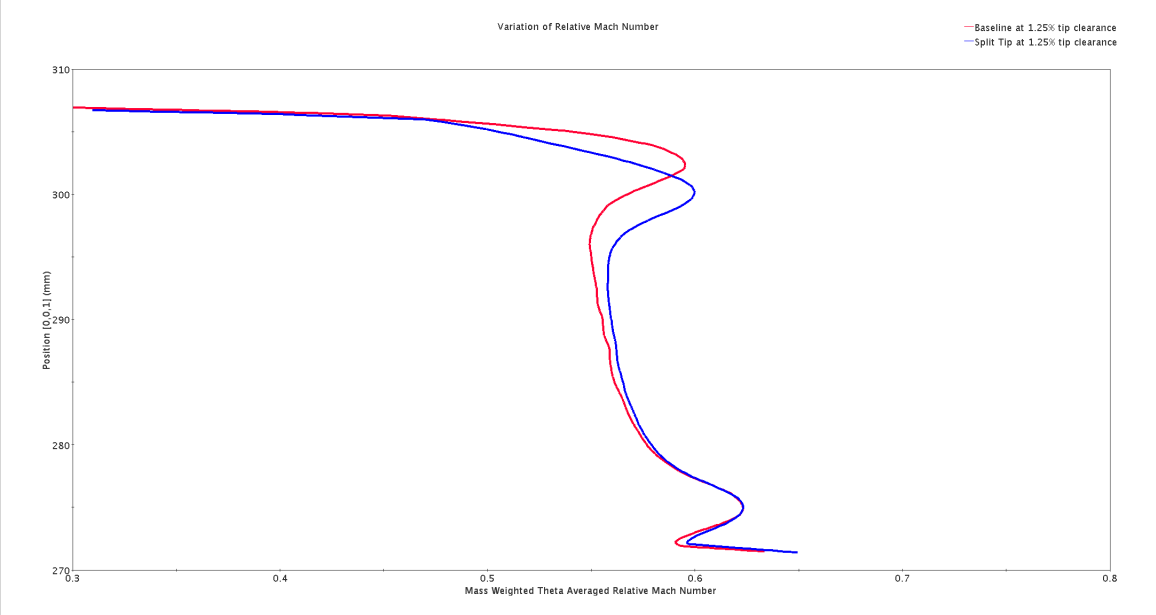

Figure 5.13: Mass Weighted Theta Averaged Relative Mach Number for 1x clearance at pb 7.95 atm.

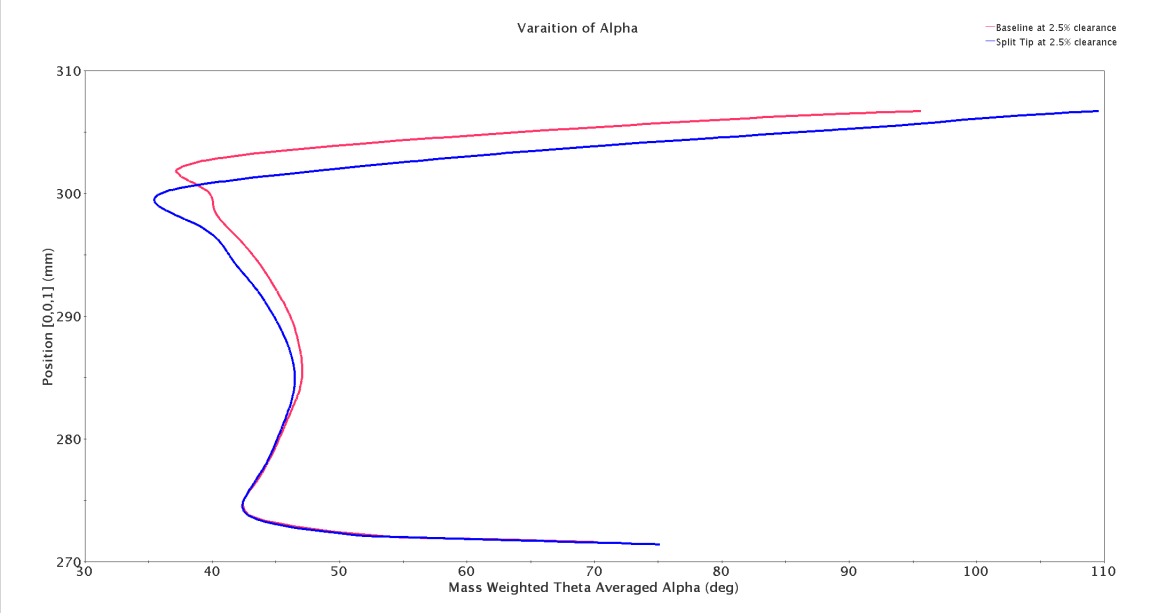

Figure 5.14: Mass Weighted Theta Averaged Alpha at 2x clearance for Pb of 7.5 atm

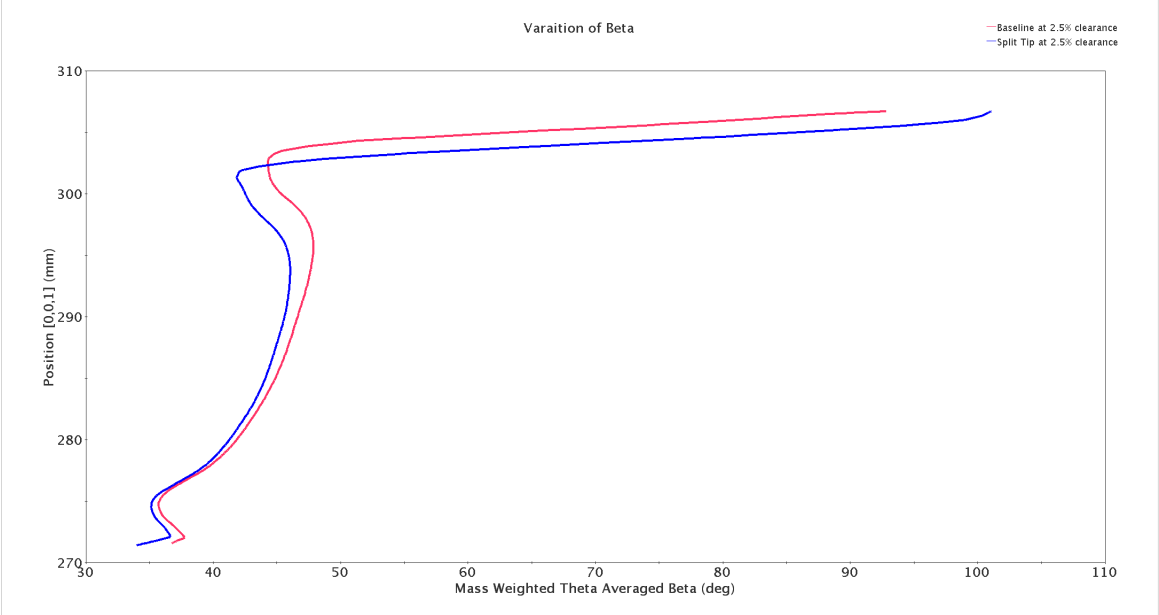

Figure 5.15: Mass Weighted Theta Averaged Beta at 2x clearance for Pb of 7.5 atm.

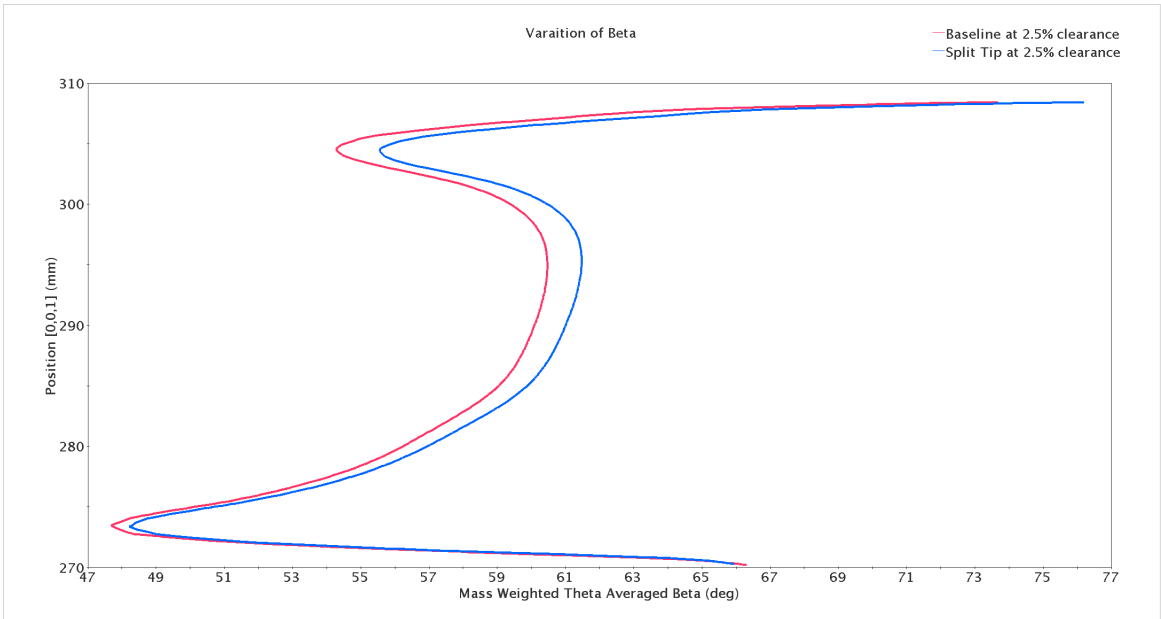

Figure 5.16: Mass Weighted Theta Averaged Beta just upstream of the blade at 2x clearance and pb 7.5 atm

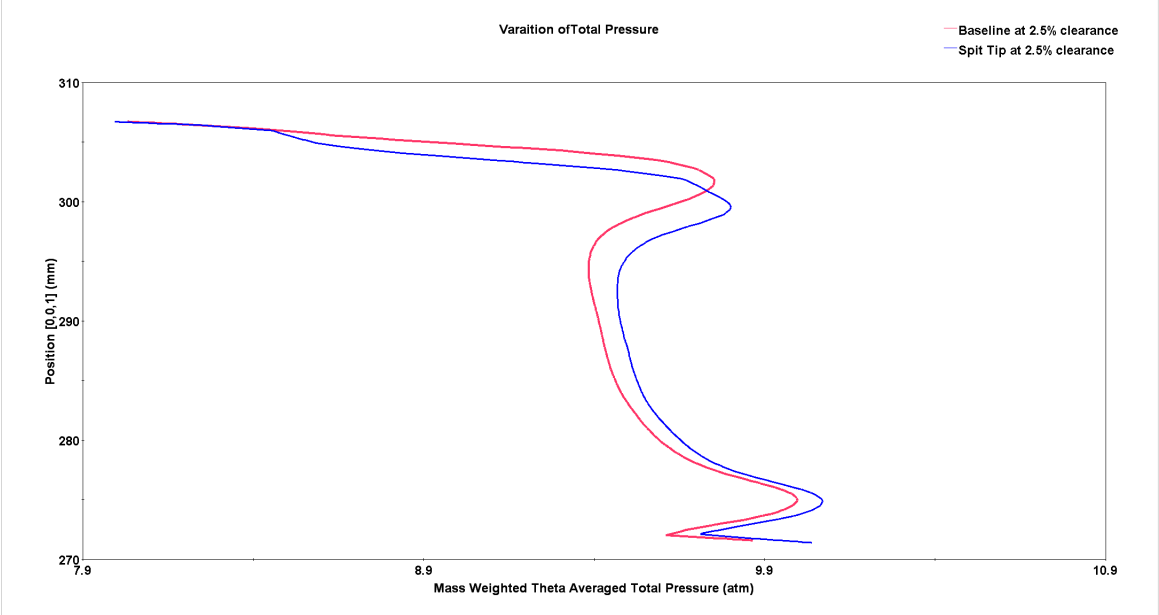

Figure 5.17: Mass Weighted Theta Averaged Total Pressure at 2x clearance for pb 7.5 atm

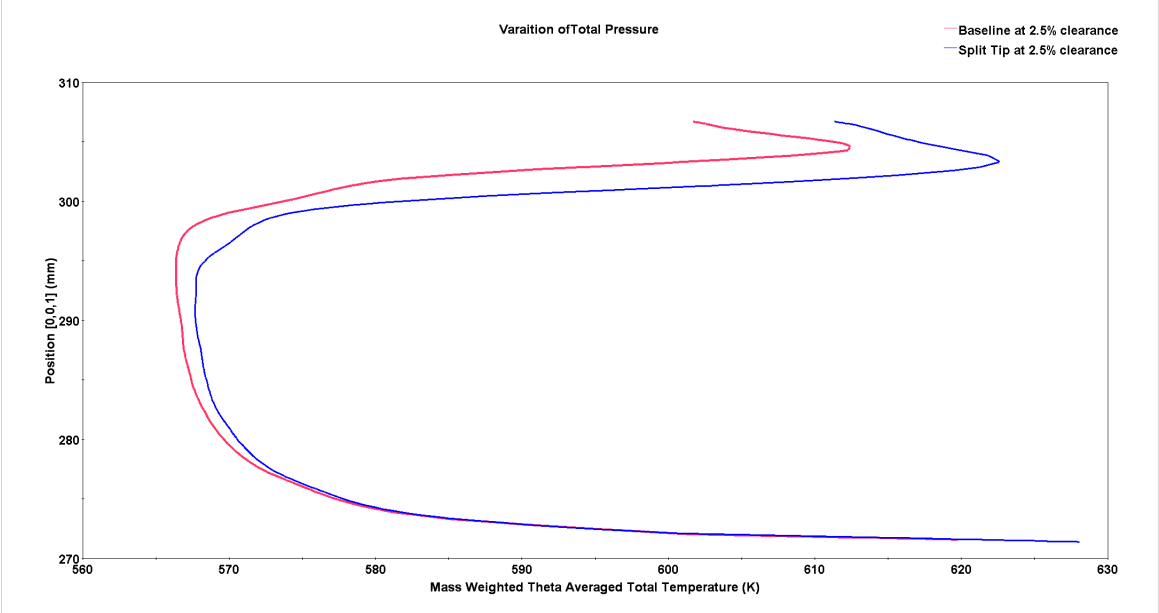

Figure 5.18: Mass Weighted Theta Averaged Total Temperature at 2x clearance for pb 7.5 atm.

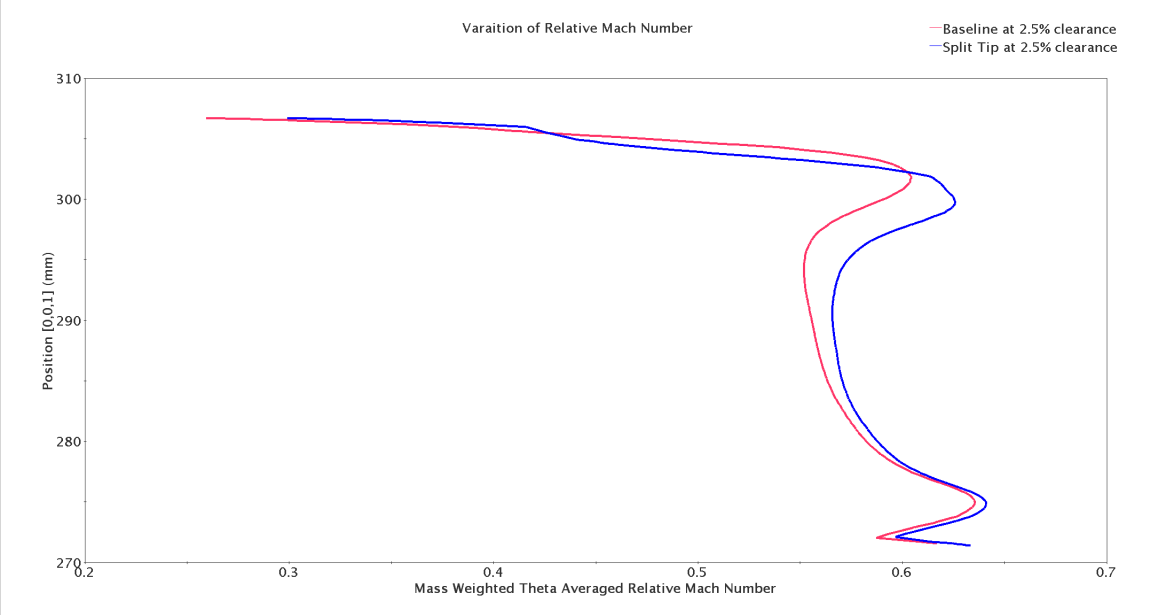

Figure 5.19: Mass Weighted Theta Averaged Relative Mach Number for 2x clearance at pb 7.5 atm.

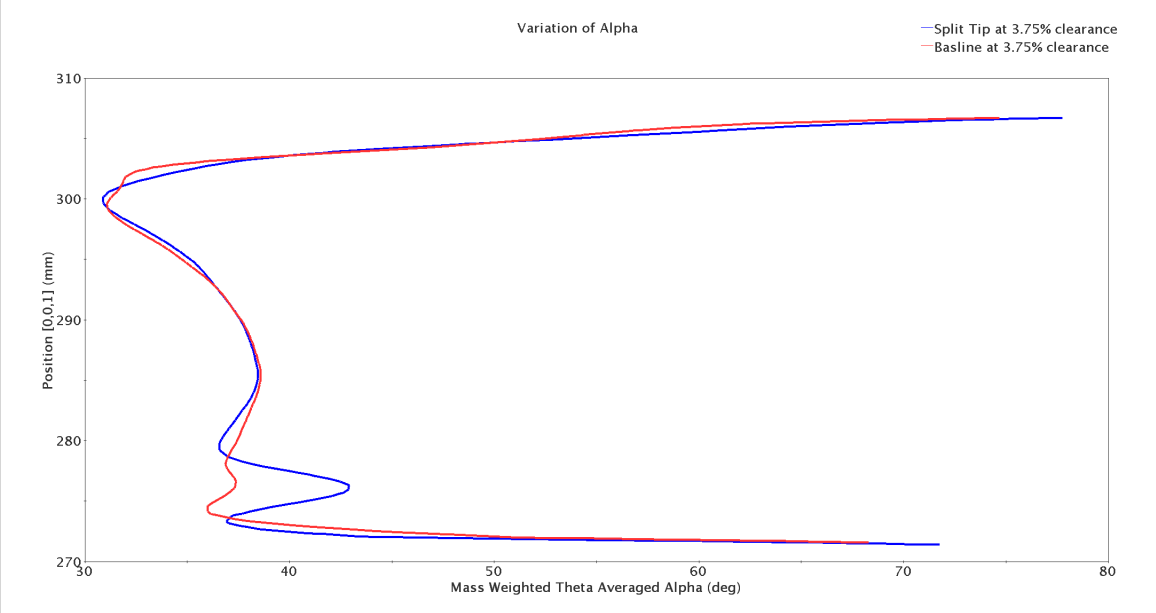

Figure 5.20: Mass Weighted Theta Averaged Alpha at 3x clearance for Pb of 6.75 atm

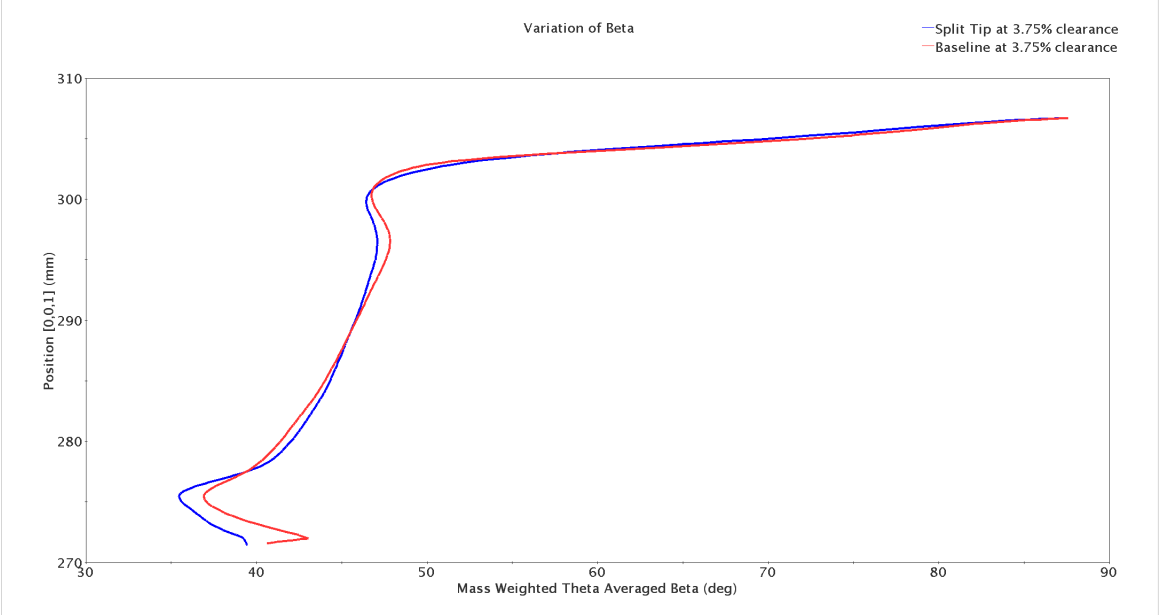

Figure 5.21: Mass Weighted Theta Averaged Beta at 3x clearance for Pb of 6.75 atm.

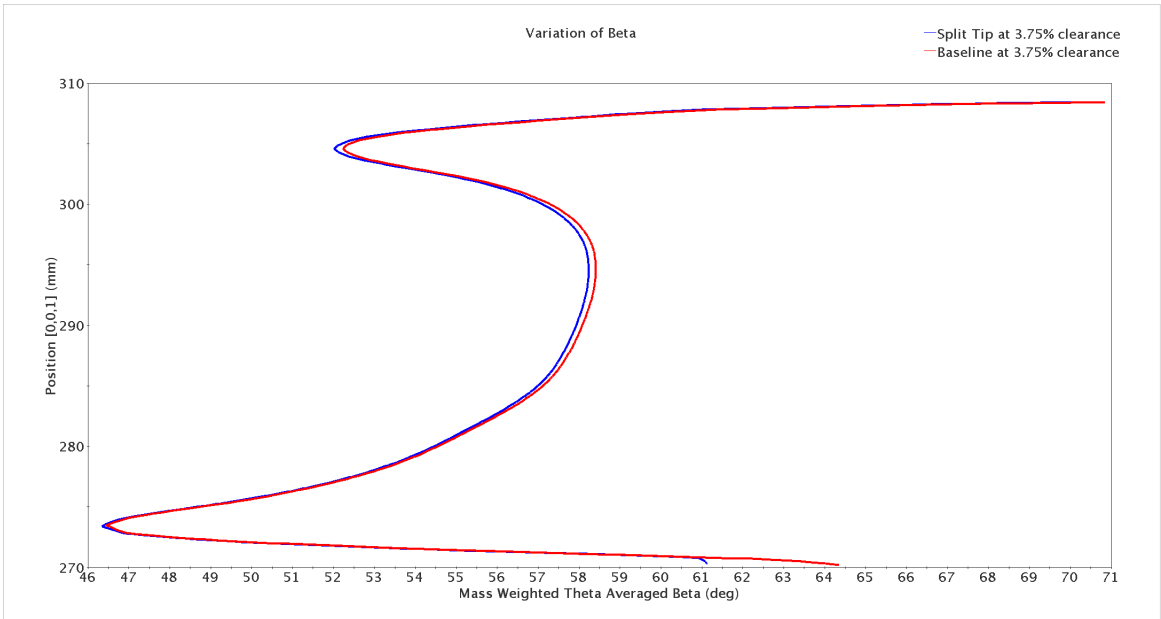

Figure 5.22: Mass Weighted Theta Averaged Beta just upstream of the blade at 3x clearance and pb 6.75 atm

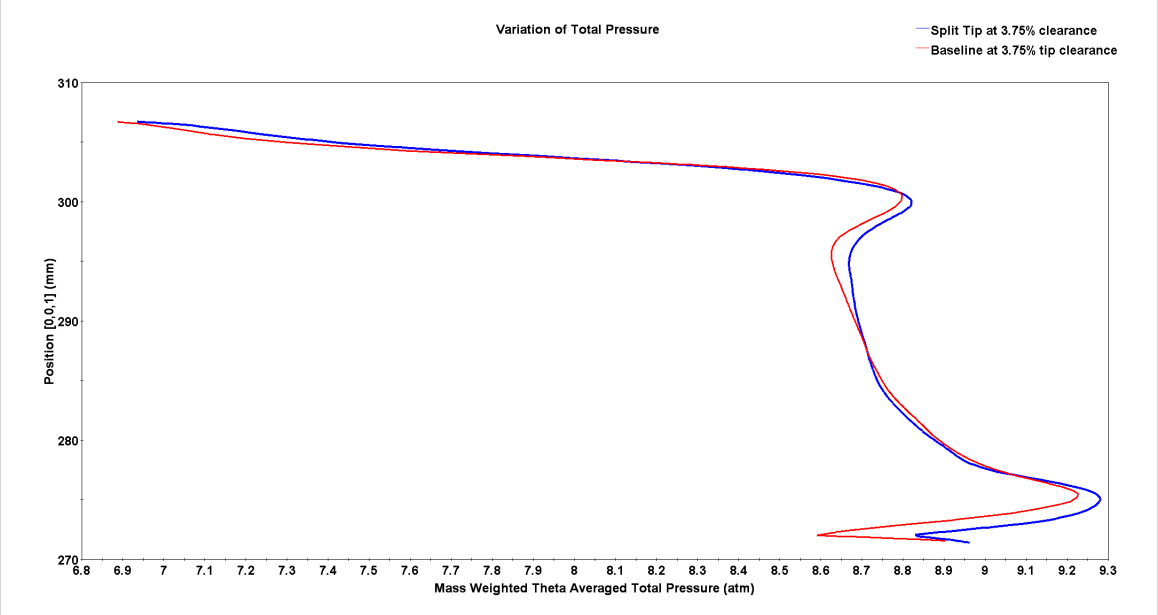

Figure 5.23: Mass Weighted Theta Averaged Total Pressure at 3x clearance for pb 6.75 atm

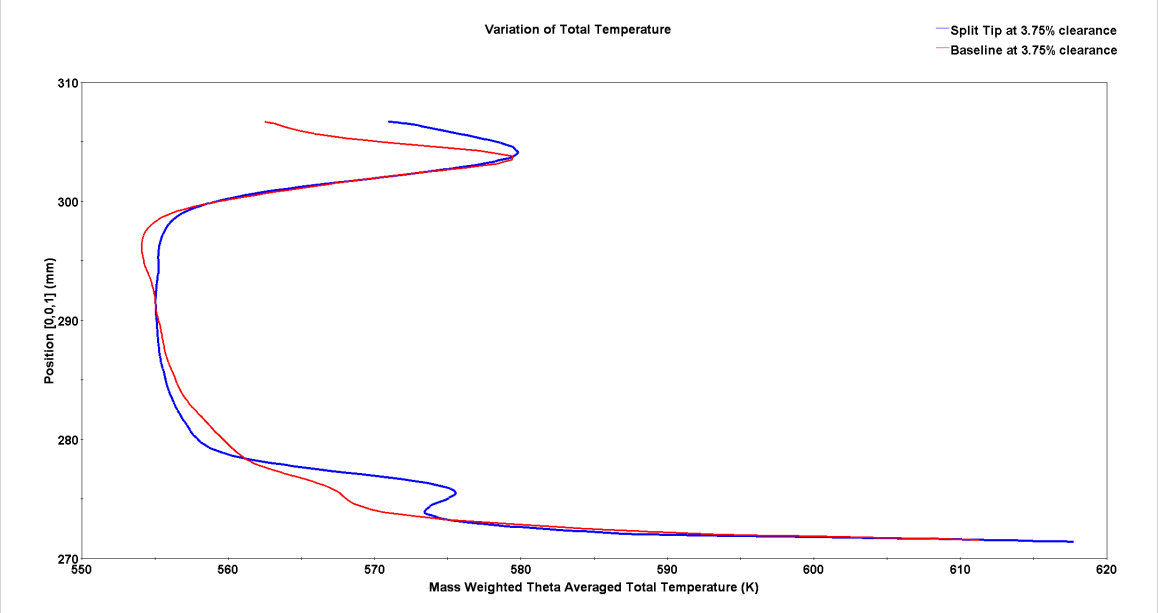

Figure 5.24: Mass Weighted Theta Averaged Total Temperature at 3x clearance for pb 6.75 atm.

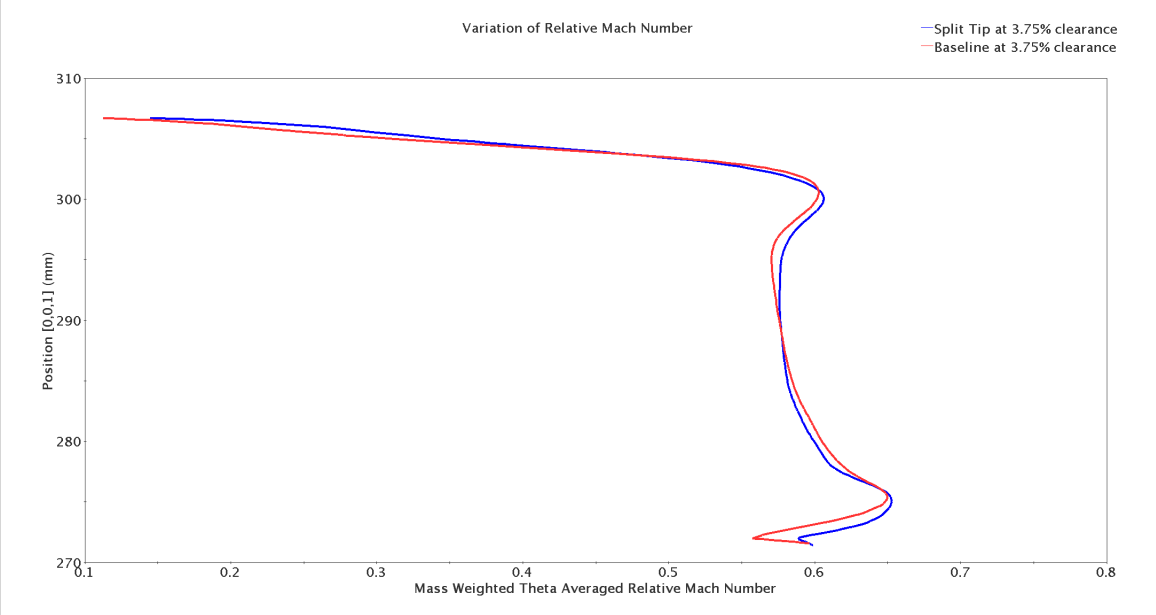

Figure 5.25: Mass Weighted Theta Averaged Relative Mach Number for 3x clearance at pb 6.75 atm.

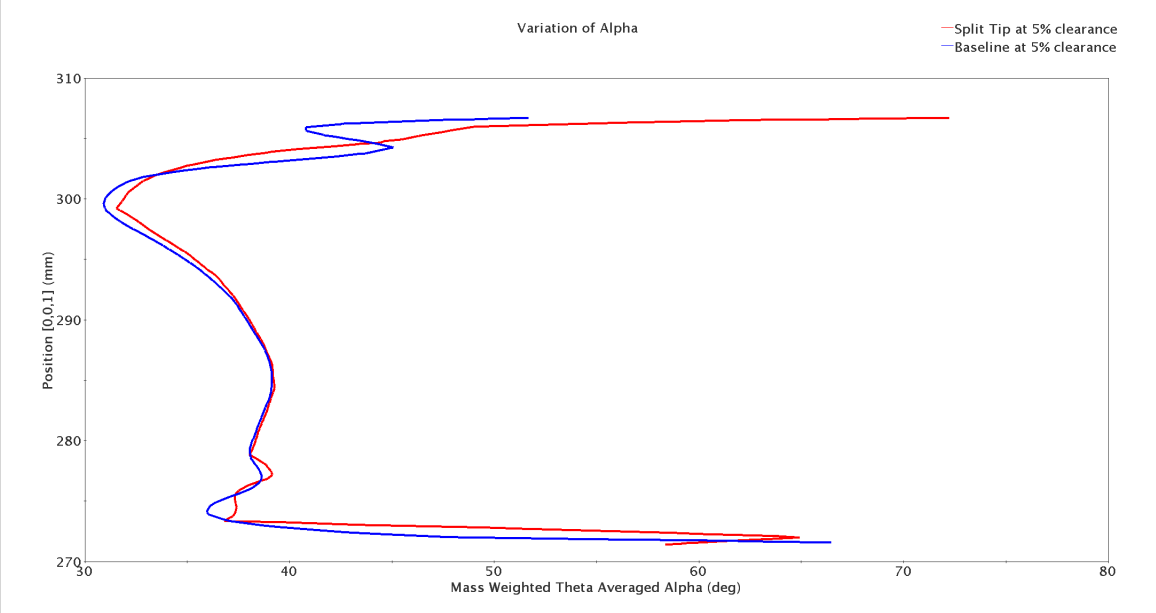

Figure 5.26: Mass Weighted Theta Averaged Alpha at 4x clearance for Pb of 6.5 atm

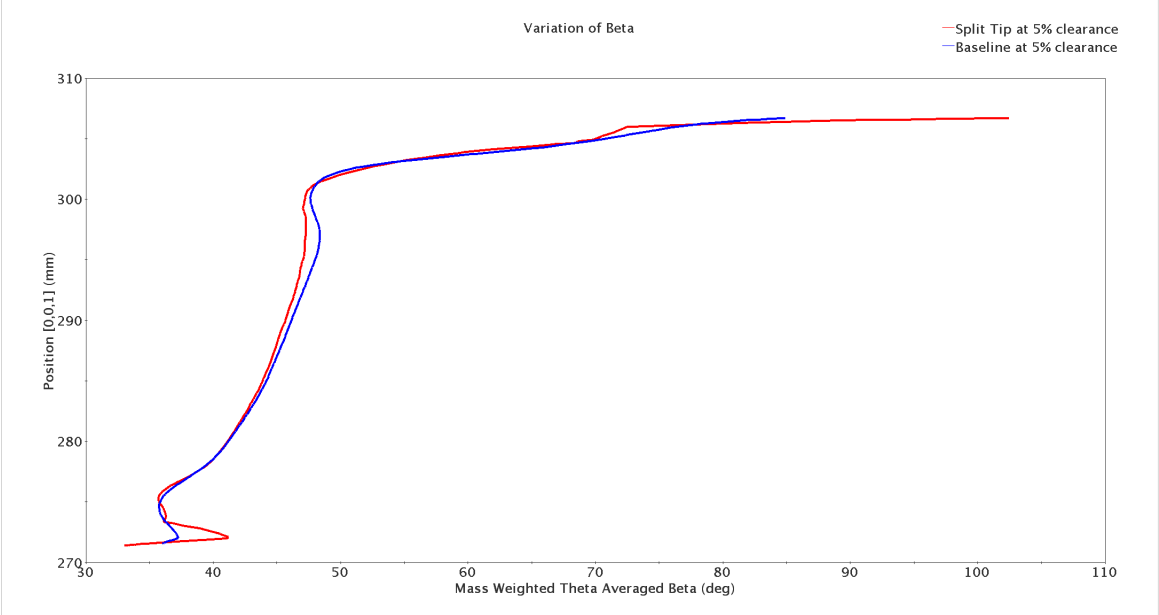

Figure 5.27: Mass Weighted Theta Averaged Beta at 4x clearance for Pb of 6.5 atm.

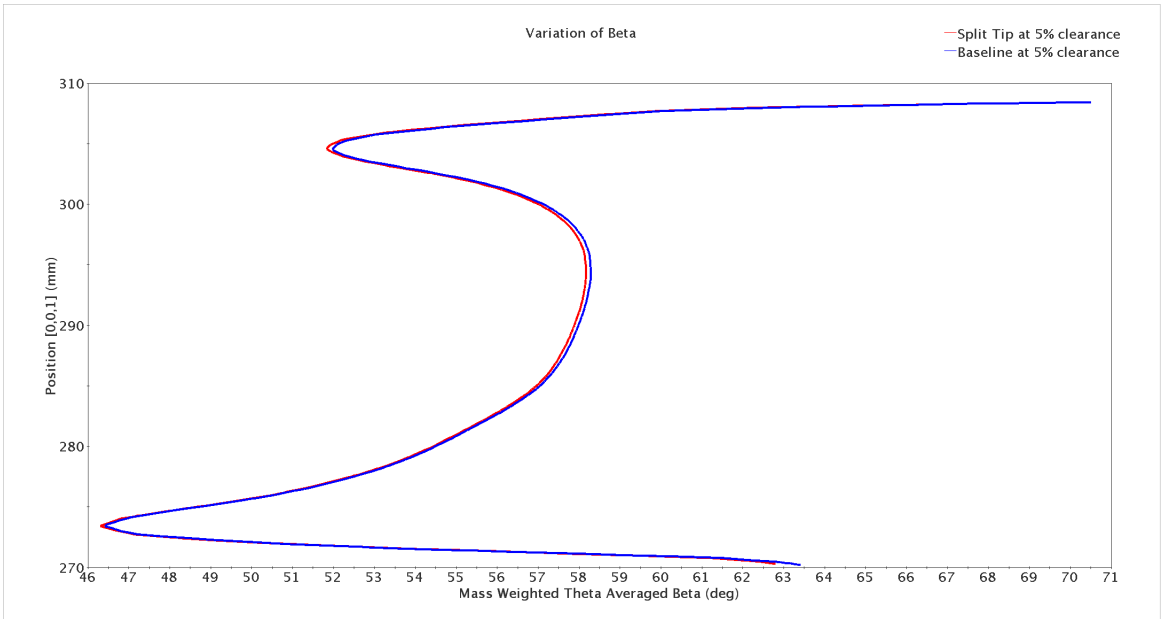

Figure 5.28: Mass Weighted Theta Averaged Beta just upstream of the blade at 4x clearance and pb 6.5 atm

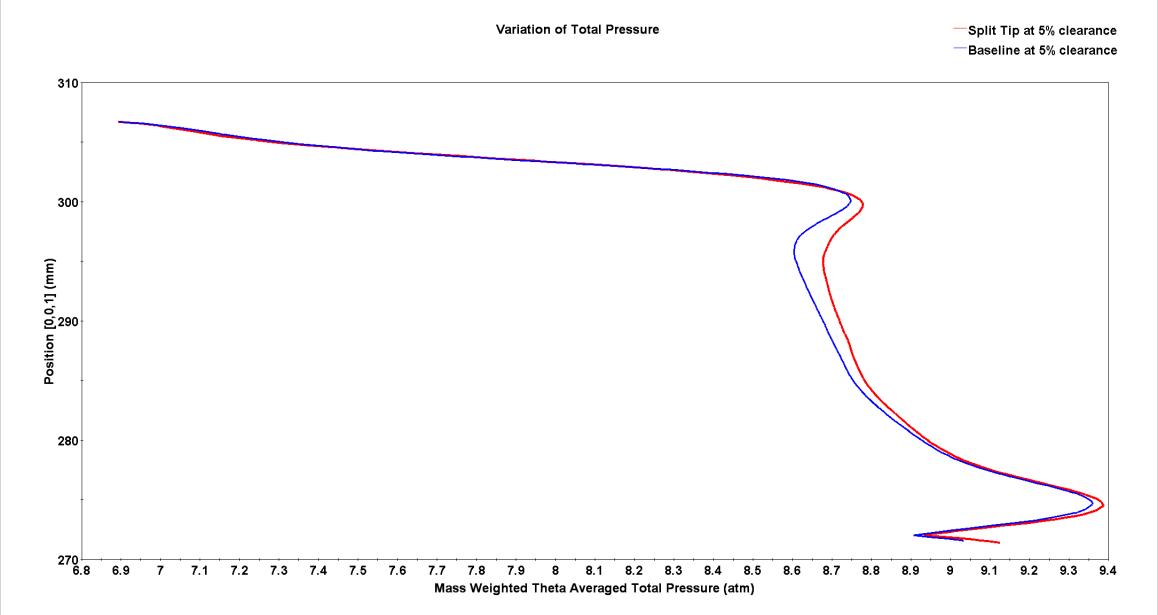

Figure 5.29: Mass Weighted Theta Averaged Total Pressure at 4x clearance for pb 6.5 atm

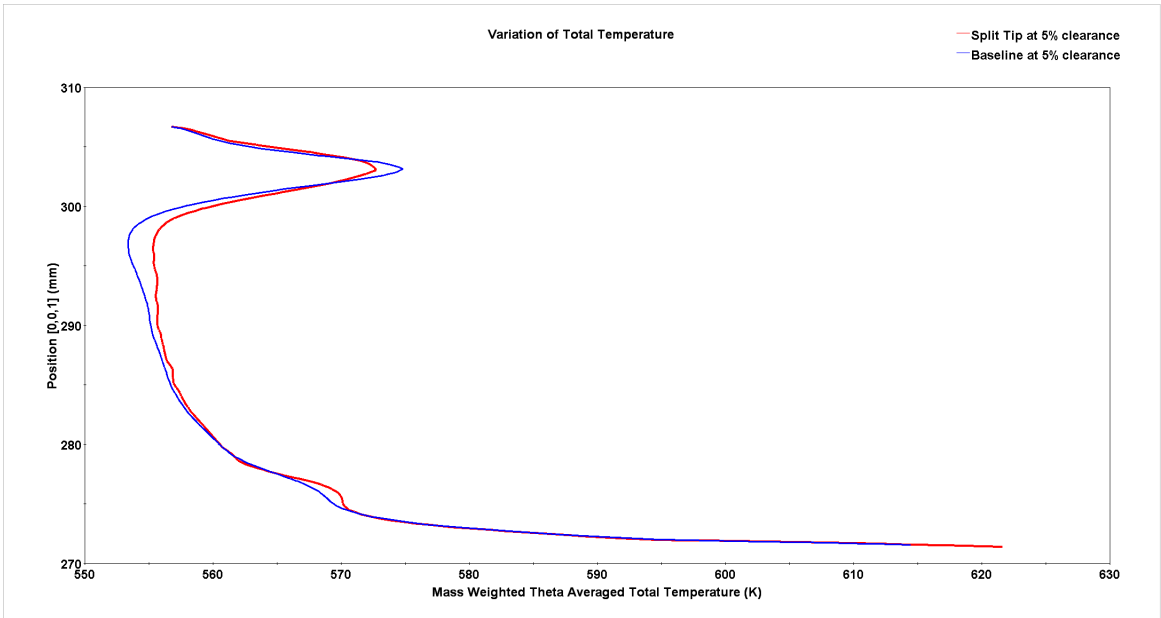

Figure 5.30: Mass Weighted Theta Averaged Total Temperature at 4x clearance for pb 6.5 atm.

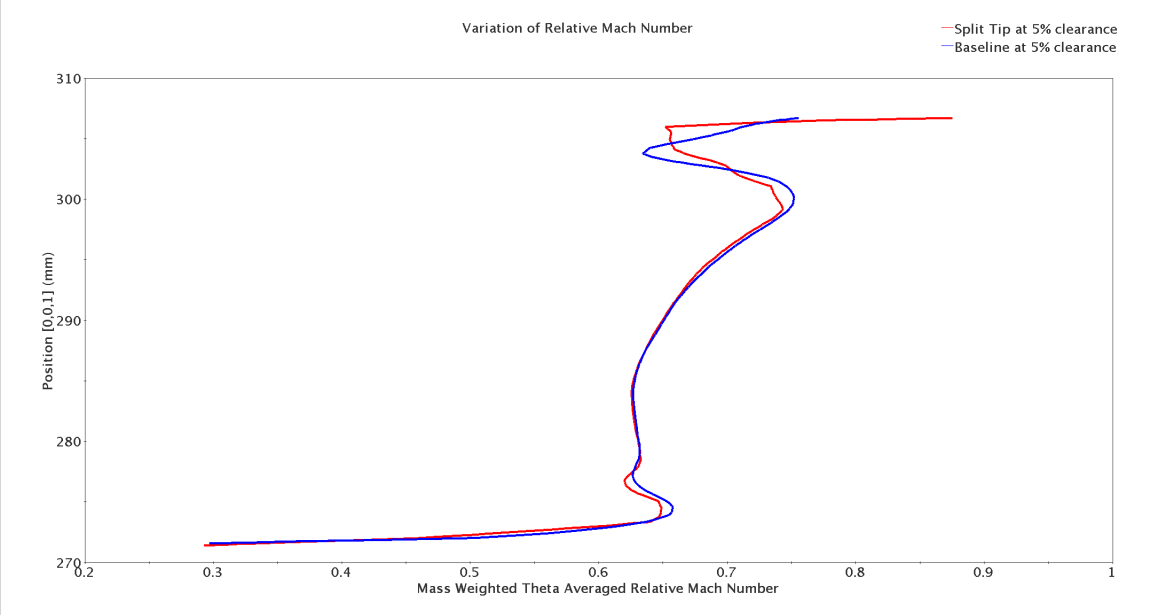

Figure 5.31: Mass Weighted Theta Averaged Relative Mach Number for 4x clearance at pb 6.5 atm.

Figures 5.32 to 5.36 shown the streamwise vorticity contours at the plane downstream of the blade shown in Figure 4.30.

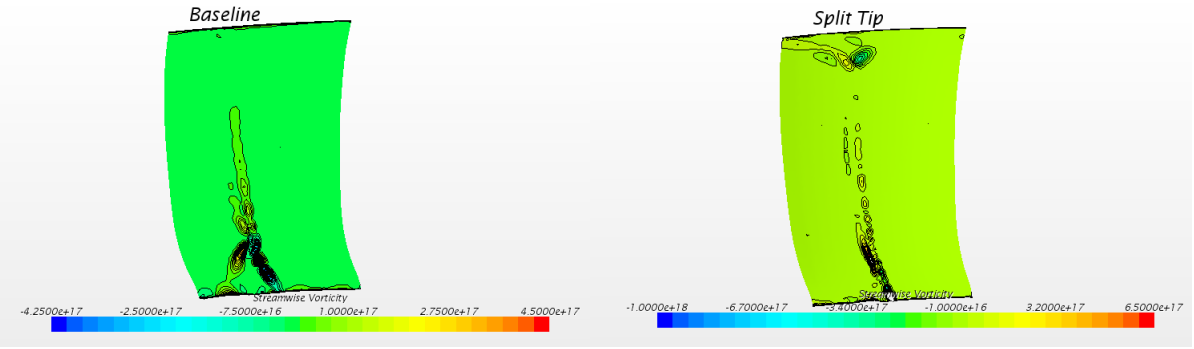

Figure 5.32: Streamwise Vorticity for 1x clearance at pb 7.95atm.

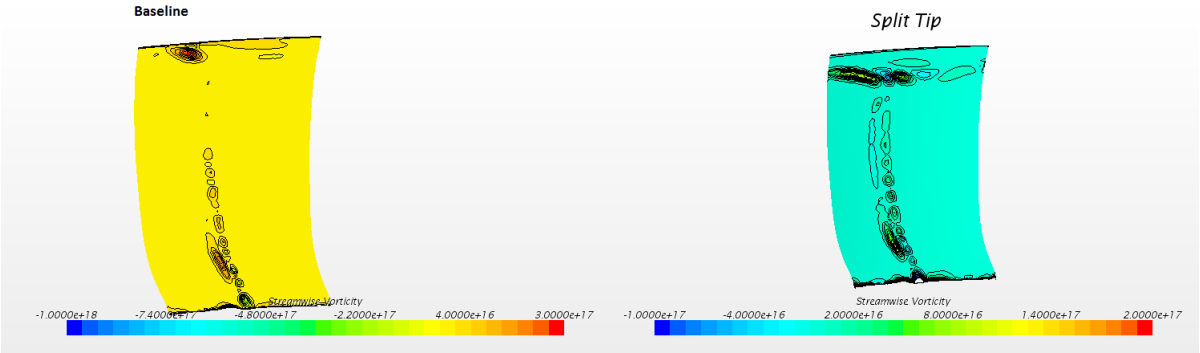

Figure 5.33: Streamwise Vorticity for 0.5x clearance at pb 8.1atm.

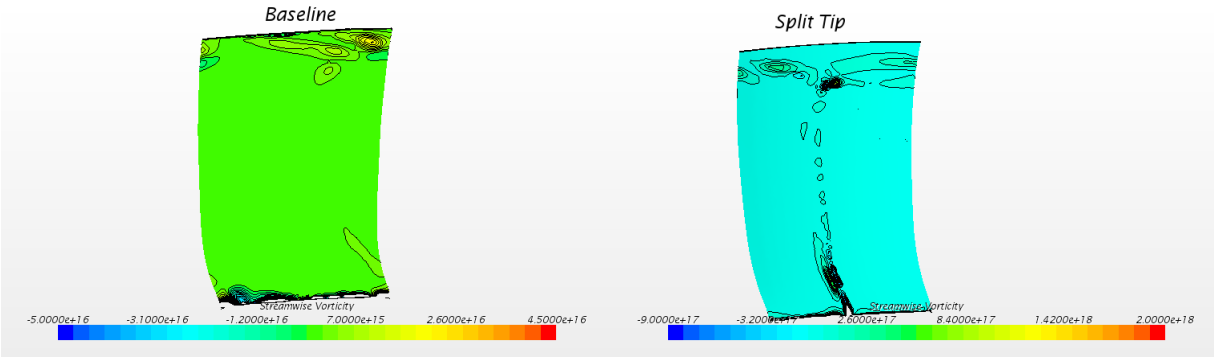

Figure 5.34: Streamwise Vorticity for 2x clearance at pb 7.5atm.

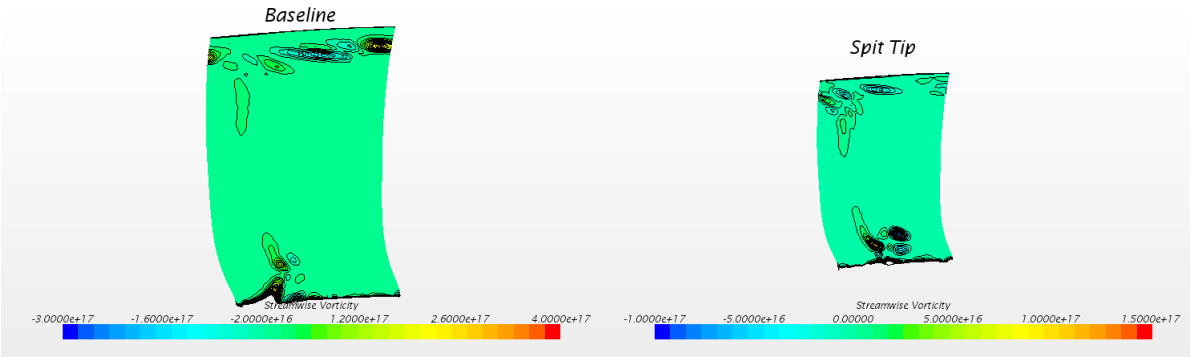

Figure 5.35: Streamwise Vorticity for 3x clearance at pb 6.75atm.

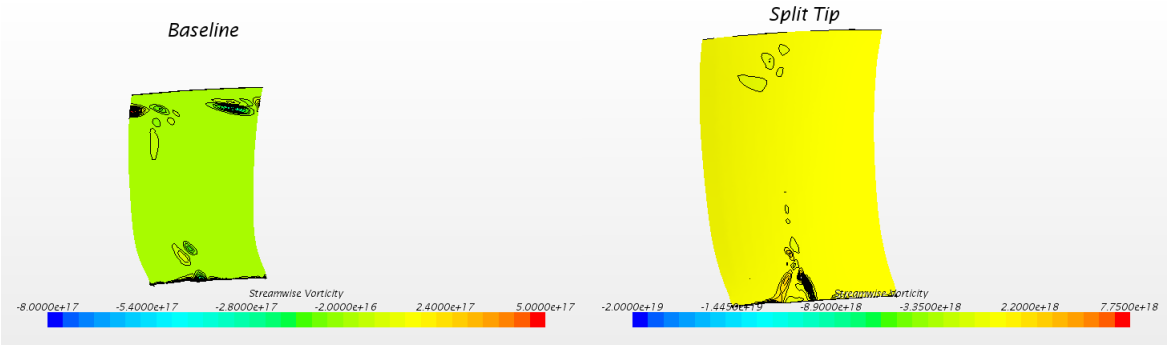

Figure 5.36: Streamwise Vorticity for 4x clearance at pb 6.5atm.